Theoretical and Experimental Investigation of Boundary Layer Ingestion for Aircraft Application

Lv, Lex

DOI
10.4233/uuid:6d8bd168-e057-4ee9-854c-32c84015e4c4

Publication date
2019

Document Version
Final published version

Citation (APA)
Lv, L. (2019). *Theoretical and Experimental Investigation of Boundary Layer Ingestion for Aircraft Application*. [Dissertation (TU Delft), Delft University of Technology]. https://doi.org/10.4233/uuid:6d8bd168-e057-4ee9-854c-32c84015e4c4

Important note
To cite this publication, please use the final published version (if applicable).
Please check the document version above.

Theoretical and Experimental Investigation of Boundary Layer Ingestion for Aircraft Application

Dissertation

for the purpose of obtaining the degree of doctor

at Delft University of Technology

by the authority of the Rector Magnificus Prof.dr.ir. T.H.J.J. van der Hagen,

chair of the Board for Doctorates

to be defended publicly on

Tuesday 23 April 2019 at 12:30 o'clock

by

Peijian LV

Master of Engineering in Flight Vehicle Design, Northwestern Polytechnical University, China

born in Chenzhou, China

This dissertation has been approved by the promotors.

Composition of the doctoral committee:

Rector Magnificus	chairperson
Prof.dr.ir. L.L.M. Veldhuis	Delft University of Technology, promotor
Dr. A. G. Rao	Delft University of Technology, copromotor

Independent members:

Prof. dr. ing. G. Eitelberg	Delft University of Technology
Prof. dr. T. Grönstedt	Chalmers University of Technology, Sweden
Prof. ir. J.J. Hopman	Delft University of Technology
Dr. J. Sabnis	Massachusetts Institute of Technology, USA
Dr. A.T. Isikveren	Safran Tech, France

This work is supported by the Chinese Scholarship Council (CSC), grant number 2011629073.

Printed by Ridderprint

ISBN XXXX

An electric version of this dissertation is available at

http://repository.tudelft.nl/

To my family

Summary

This thesis presents research on Boundary Layer Ingestion (*BLI*). *BLI* is an unconventional aircraft-engine integration technique which aims at integrating the aircraft and the propulsion system such that the overall aircraft fuel consumption can be reduced.

This research begins with a literature survey on propulsion integration. The literature is not only limited to recent work on novel aircraft concepts utilizing *BLI* but also covers the previous studies on ship propellers and pusher propellers used for aircraft. Various studies in the literature show that *BLI* and/or similar configurations can effectively reduce the total power consumption of the propulsion system. However, discrepancies can be identified amongst various research with respect to the improvements that *BLI* could provide in terms of reduction in the power consumption. Different research methods have been used to investigate and study this phenomenon in the literature. In particular, the various research methods give an indication that the physics involved in *BLI* might not be well understood. As a result, the current research aims to enhance the fundamental understanding of *BLI*. The main research questions are identified below:

- What are the mechanisms of *BLI* for the provided benefit?
- How large is the benefit of BLI?

This study addresses the aforementioned questions by following a research line where power conversion is the key to explaining the mechanisms of *BLI*. The current research consists of three main pillars, namely **theoretical analysis, numerical simulation and experimental study**. In the theoretical analysis, the physical model for understanding *BLI* is developed. Numerical simulations and experimental study provide validations to the developed model and assist in understanding the phenomenon involved with BLI.

In the theoretical analysis, effort is made to evaluate the performance of the propulsor and its associated fuselage in two configurations, namely the so-called *BLI* configuration and the Wake Ingestion (*WI*) configuration. A power conversion analysis uses Power Balance Method (*PBM*) introduced by Drela to elaborate the power saving mechanism of *WI*, showing that the Froude's propulsive efficiency as a figure of merit should be separated from the power conversion efficiency in these configurations. The body/propulsor interaction occurring in the *BLI* configuration is qualitatively analyzed to clarify its influence on the performance of the integrated vehicle. The results suggest that the minimization of total power consumption should be used as a design criterion for aircraft utilizing *BLI* rather than focusing on minimization of drag, as is generally done.

The numerical simulations are considered as an extension of the theoretical analysis to support the physical understanding of *BLI* elaborated in the developed theoretical model. This simulation study has two major objectives: establishing the process of typical power conversions and quantifying the influences of *BLI* on the

power conversion of the theoretical model. To achieve these objectives, this study on power conversion processes is rather limited to simple cases, which help to decipher the processes easily and these cases bring out the key elements involved in the power conversion process elegantly. Therefore, the simulation is limited to 2D steady laminar incompressible flows, which excludes complicated flow physics, such as turbulence, compressibility, etc. This simplification allows the analysis to be focused on the mechanisms elaborated in the theoretical analysis. In this simulation study only typical models are used and the simulation results are processed using the *PBM*. The results prove that *BLI* could increase the profile drag of a body but reduce the actual total power consumption.

The experimental study aims to provide evidence to the physical understanding of *BLI* developed during the theoretical analysis. This study focuses on the power conversion processes involved in a propulsor operating in the wake of the body. The experimental setup is specifically designed such that the same propulsor can ingest a body wake or purely work in the free stream. Conventional force balance measurement techniques are used to measure the thrust and power in the experiments. Stereoscopic PIV is employed in order to visualize the flow and understand the physics involved in *BLI* and *WI*. This technique has been used for the first time to visualize the flow in wake ingesting propellers. Furthermore, the *PBM* is used to quantify the power conversion mechanisms using the data obtained from the experiments. The results prove that the dominant mechanism responsible for the efficiency enhancement in this experimental study is due to the utilization of body wake energy by the wake ingesting propeller.

Finally, efforts are made to summarise the main findings of the three pillars. These methods are theoretical analysis, numerical simulation, and experimental study respectively. A key working principle encompassing the entire research is extracted. The conclusion of this research provides answers to the research questions raised in the earlier chapters of this thesis, and recommendations for future research are provided.

Overall, the importance of wake energy flow rate in understanding *BLI* & *WI* phenomenon is highlighted. This understanding is a major milestone in the research into this phenomenon. In terms of the results, this research agrees with several previous investigations which claim that *BLI* could effectively reduce power consumption of the aircraft.

Samenvatting

Dit proefschrift presenteert onderzoek aan Boundary Layer Ingestion (BLI). *BLI* is een vliegtuig-motor integratie techniek die het doel heeft het vliegtuig en het voortstuwingssysteem zodanig te integreren dat het totale brandstofverbruik van het vliegtuig kan worden verminderd.

Dit onderzoek begint met een literatuurstudie over voortstuwingsintegratie. De gepresenteerde literatuur is niet gelimiteerd tot recent gepubliceerd werk over nieuwe vliegtuigconfiguraties die gebruik maken van BLI, maar omvat ook eerdere studies over scheepsschroeven en vliegtuig propellers in duwconfiguratie. Verschillende studies in literatuur laten zien dat BLI en/of vergelijkbare configuraties effectief het totale energieverbruik van het voortstuwingssysteem kan verminderen. Echter, discrepanties kunnen worden vastgesteld tussen verscheidende onderzoeken met betrekking tot de verbetering in het energieverbruik die BLI kan veroorzaken. In literatuur zijn verschillende onderzoeksmethodes gebruikt om dit fenomeen te onderzoeken. Deze methodes wijzen erop dat de fysica achter BLI mogelijk niet goed begrepen wordt. Dit onderzoek heeft tot doel het fundamentele begrip van BLI te verbeteren. De belangrijkste onderzoeksvragen worden geïdentificeerd zoals hieronder:

Wat zijn de fysieke mechanismen die betrokken zijn bij BLI?

Hoe groot is het voordeel van BLI?

Deze studie adresseert de voorgenoemde vragen door een onderzoekslijn te volgen waarbij vermogensconversie wordt gebruikt om de mechanismen van BLI uit te leggen. Dit onderzoek bestaat uit drie hoofdpijlers, namelijk **theoretische analyse**, **numerieke simulatie** en **experimentele studie**. In de theoretische analyse wordt het fysische model om BLI te begrijpen ontwikkelt. De numerieke simulaties en experimentele studie brengen validatie voort voor het ontwikkelde model en helpen tevens in het begrip van de fenomenen die een rol spelen bij BLI.

In de theoretische analyse wordt inspanning gedaan om de prestaties van de het voortstuwingssysteem en de bijbehorende romp in twee configuraties te evalueren, namelijk de zogenaamde BLI-configuratie en de Wake Ingestion (WI) -configuratie. Een analyse van de vermogensconversie die gebruikt van de Power Balance Method (PBM), geïntroduceerd door Drela om het mechanisme van de energiebesparing van WI uit te werken, laat zien dat het Froude's voortstuwingsrendement voor deze configuraties moet worden gescheiden van de vermogensconversie-efficiëntie. De interactie tussen romp en voortstuwingselement die plaatsvindt in de BLI configuratie wordt kwalitatief geanalyseerd om te verduidelijken wat het effect is op de prestaties van het geïntegreerde voertuig. De resultaten suggereren dat de minimalisatie van het totale energieverbruik moet worden gebruikt als ontwerpcriterium voor vliegtuigen die gebruikmaken van BLI, in plaats van zich te concentreren op het minimaliseren van de weerstand, zoals over het algemeen wordt gedaan.

De numerieke simulaties worden beschouwd als een uitbreiding van de theoretische analyse ter ondersteuning van het fysieke begrip van BLI, wat is uitgewerkt in het ontwikkelde theoretische model. Deze numerieke studie heeft twee belangrijke doelen: het vaststellen van het proces van typische vermogensconversies en het kwantificeren van de invloeden van BLI op de vermogensconversie van het theoretische model. Om deze doelstellingen te bereiken, is deze studie beperkt tot eenvoudige gevallen omdat deze het gemakkelijker maken de processen te ontcijferen en de belangrijkste elementen die betrokken zijn bij het vermogensconversie proces op elegante wijze naar voren te brengen. Daarom is de simulatie beperkt tot 2D tijdsonafhankelijke laminaire niet-samendrukbare stromingen, die ingewikkelde stromingsfysica zoals turbulentie en samendrukbaarheid van de stroming uitsluit. Deze vereenvoudiging maakt het mogelijk dat de numerieke analyse wordt gericht op de mechanismen die in de theoretische analyse zijn uitgewerkt. Voor deze simulatiestudie zijn alleen typische modellen gebruikt en de simulatieresultaten worden verwerkt met behulp van de PBM. De resultaten bewijzen dat BLI de profielweerstand van een object kan vergroten, maar het werkelijke totale energieverbruik kan verminderen.

De experimentele studie is bedoeld om bewijs te leveren voor het fysieke begrip van BLI dat is ontwikkeld in de theoretische analyse. Deze studie concentreert zich op de vermogensconversie processen die betrokken zijn bij een voortstuwingselement die in de zog opereert. De experimentele opstelling is specifiek zo ontworpen dat hetzelfde voortstuwingselement zowel in een zog als in de ongestoorde stroming kan werken. Conventionele meettechnieken gebaseerd op balansen worden gebruikt om de stuwkracht en vermogen in de experimenten te meten. Stereoscopisch PIV wordt gebruikt om de stroming te visualiseren en de fysica te begrijpen die betrokken zijn bij BLI en WI. Deze techniek werd voor de eerste keer gebruikt om de stroming rond een propeller die opereert in een zog te visualiseren. Verder wordt de PBM gebruikt om de vermogensconversiemechanismen te kwantificeren met behulp van de gegevens die uit de experimenten zijn verkregen. De resultaten bewijzen dat het dominante mechanisme dat verantwoordelijk is voor de efficiëntieverbetering in dit experimenteel onderzoek te danken is aan het gebruik van het zog-energie door de zog-innemende propeller.

Ten slotte zijn belangrijkste bevindingen samen te vatten van de drie pijlers. Deze methoden zijn respectievelijk theoretische analyse, numerieke simulatie en experimentele studie. Een essentieel werkingsprincipe dat het volledige onderzoek omvat wordt beschreven. De conclusie van dit onderzoek geeft antwoorden op de onderzoeksvragen die in de eerdere hoofdstukken van dit proefschrift aan de orde zijn gesteld en aanbevelingen voor toekomstig onderzoek worden gegeven.

Over het algemeen wordt het belang van de stroomsnelheid van het zog-energie voor het begrijpen van het BLI & WI-fenomeen benadrukt. Dit begrip is een belangrijke mijlpaal in het onderzoek naar dit fenomeen. Wat de resultaten betreft, is dit onderzoek het eens met verschillende eerdere onderzoeken die beweren dat BLI het energieverbruik van het vliegtuig effectief kan verminderen.

Nomenclature

Latin Symbols

A	reference area of the body	[m²]
C_D	$= \frac{D}{q_\infty \cdot A}$, coefficient of body drag	[-]
C_N	$= \frac{N}{q_\infty \cdot A} = C_T - C_D$, coefficient of net force	[-]
C_T	$= \frac{T}{q_\infty \cdot A}$, coefficient of thrust	[-]
C_P	$= \frac{P}{q_\infty}$, (static) pressure coefficient	[-]
C_{Pt}	$= \frac{P_t}{q_\infty}$, coefficient of total pressure	[-]
C_W	$= \frac{P_W}{q_\infty \cdot A \cdot V_\infty}$, coefficient of propeller shaft power	[-]
D	body (airframe) drag	[N]
D_{ram}	ram drag of the turbofan engine	[N]
$\dot{E}_a$	$= \iint_{TP} \rho u \cdot \frac{1}{2}(u - V_\infty)^2 dS$, axial kinetic energy deposition rate	[W]
$\dot{E}_p$	$= \iint_{TP} (p - p_\infty) \cdot (u - V_\infty)\, dS$, pressure-work deposition rate	[W]
$\dot{E}_v$	$= \iint_{TP} \rho u \cdot \frac{1}{2}(v^2 + w^2) dS$, transverse kinetic energy deposition rate	[W]
$\dot{E}_w$	$=\dot{E}_a+\dot{E}_v+\dot{E}_p$, wake energy flow (deposition) rate	[W]
f	focal length of the lens	[mm]
$f_\#$	f number of the lens	[-]
F_x	axial force	[N]
J	$= \frac{V_\infty}{n\pi R}$, advance ratio	[-]

$K\dot{E}_w$	wake kinetic energy flow rate	[W]
$K\dot{E}_p$	kinetic energy production rate	[W]
$K\dot{E}_{loss}$	kinetic energy loss (sink) rate	[W]
k	kinetic energy thickness	[-]
L	length	[m]
N	net force of the vehicle (aircraft)	[N]
n	propeller rotational speed	[rpm]
p	static pressure	[Pascal]
p_t	total pressure	[Pascal]
p_∞	ambient pressure	[Pascal]
P_K	mechanical energy addition rate	[W]
P_W	$= \frac{2\pi n}{60} \cdot Q$, shaft power of the propeller	[W]
Q	propeller reaction torque	[Nm]
q_∞	dynamic pressure of free stream flow	[Pascal]
R	propeller radius	[m]
S	surface area	[m^2]
T	thrust	[N]
T_{gross}	gross thrust of the turbofan engine	[N]
T_{net}	net thrust of the turbofan engine	[N]
TI	$= \frac{\sqrt{\frac{1}{3}\left(u'u' + v'v' + w'w'\right)}}{V_\infty}$, turbulence intensity	[-]
u, v, w	fluid velocity components	[m/s]
V	fluid velocity	[m/s]

V_∞	free stream velocity	[m/s]
w_j	width of jet wake	[m]
X, Y, Z	Cartesian coordinate axes	[-]
x	X coordinate of a flat plate (Blasius model)	[m]

Greek symbols

η_p	$= \frac{T \times V_\infty}{P_w} = \frac{C_T}{C_W}$, Froude (propulsive) power coefficient ("efficiency")	[-]
θ	momentum deficit thickness	[-]
μ	viscosity	[kg/(m s)]
ν	kinematic viscosity	[m2/s]
ρ	fluid density	[kg/m3]
σ	uncertainty	[-]
Φ	viscous dissipation rate	[W]

Subscripts

b	body wake
cruise	cruise
free	free stream actuator disc
in	inflow
install	installed
ideal	ideal wake filling actuator disc
j	jet wake

$_{out}$	outflow
$_{uninstall}$	uninstalled propulsor
$_{WI}$	wake ingestion actuator disc
$_{BL}$	boundary layer
$_{\infty}$	free stream
$_{w}$	wake
$_{TP}$	trefftz plane
$_{SP}$	survey plane

Abbreviations

AEI	Aerodynamic efficiency index
AFC	Active flow control
BLI	Boundary layer ingestion
BPR	Bypass ratio
BWB	Blended wing body
CV	Control volume
CFD	Computer fluid dynamics
DPCP	Circumferential distortion intensity descriptor
FSP	Free stream propulsion
FVM	Finite volume method
KE	Kinetic energy
L/D	Lift to drag ratio

LPT	Low pressure turbine
MTOW	Maximum take-off weight
OPR	Overall pressure ratio
PBM	Power balance method
PFC	Passive flow control
PI	Propulsion integration
PIV	Particle image velocimetry
RPK	Revenue passenger kilometer
SP	Survey plane
TP	Trefftz plane
TPS	Turbine powered simulator
UDF	User defined function
UHBR	Ultra-high bypass ratio
VHBR	Very-high bypass ratio
WI	Wake ingestion

Contents

Chapter 1 Introduction

1.1 Growth in aviation

Right since the inception of the 'jet age', travelling by air has become easier and more affordable. An important driver of this growth has been the improvement in the aircraft fuel efficiency, as the fuel cost can amount to 30% of the total operating cost [1]. New technologies and materials have enabled substantial efficiency improvement in the past decades. The trend can be observed from the historical review of fuel efficiency of passenger aircraft from the 1960s to the beginning of this century. Figure 1-1 shows the consistent reduction of Energy Intensity, which is defined as the energy consumption per Revenue Passenger Kilometer (*RPK*). The figure shows that to deliver an average passenger or equivalent cargo for the same distance, the fuel consumed by the latest Boeing 787 (produced since 2009) passenger aircraft is about 1/3 of the amount needed by the first Boeing 707 aircraft (produced since 1958).

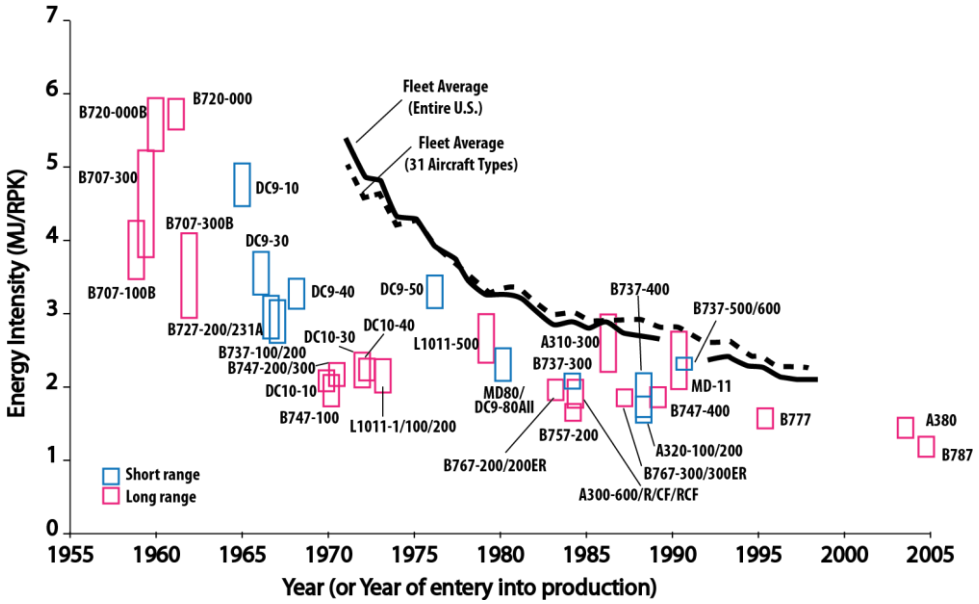

Fig. 1-1. Review of fuel efficiency improvement of passenger aircraft, adapted from reference [2].

Despite this phenomenal improvement in fuel efficiency due to new technologies, the total fuel consumed by the aviation sector has increased significantly due to the continuous growth in air traffic. Even though the growth in air traffic temporarily stagnated due to several incidents in the past, the total *RPK*s has significantly increased over the past decades, as can be seen in Fig. 1-2. As shown by the statistics provided by *ICAO*, the total air traffic in terms of *RPK* has increased from approximately 100 billion in 1960 to 5.4 trillion in 2012, an increase of more than 50

times in 42 years [3]. The air cargo transportation has also experienced a similar expansion [3].

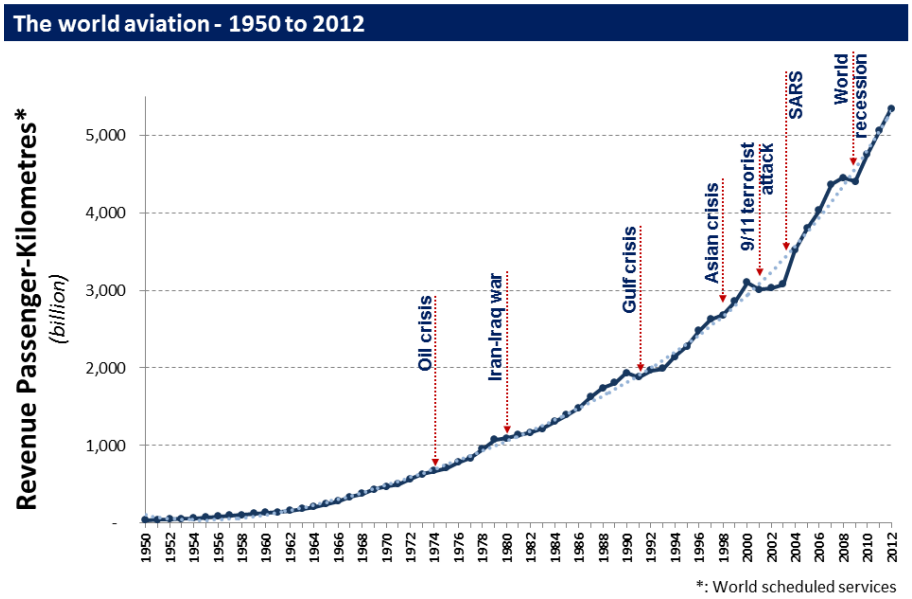

Fig. 1-2. Historical growth of air transport experienced in Revenue Passenger-Kilometers [3].

The *ICAO* forecasts a further growth of total air traffic, which might give rise to energy and environmental issues in the near future [4, 5]. It is essential to meet the demands of air travel in a sustainable way. Therefore, ambitious goals have been set to reduce fuel consumption and emissions for future aircraft. Amongst the most challenging goals, the *NASA* N+3 program aims at 70% fuel burn reduction by the year of 2035 [6], while the *ACARE* Flightpath 2050 targets a reduction of CO_2 emissions of about 75% by 2050 [7]. The target of cutting back in CO_2 emissions requires a reduction in aircraft fuel burn or the replacement of fossil fuels. These challenges encourage investigating alternatives and unconventional technologies, such as novel aircraft configurations [8, 9] and new propulsion technologies [10].

1.2 The main power requirements of aircraft

Before addressing the challenges, it is helpful to present a system overview in which the effect on the fuel efficiency of aircraft is discussed. A Sankey diagram [11] is a method used to visualize the transfer of power in a complex system, allowing the users to identify various paths of energy conversions and thereby identifying the inefficiencies and the potential savings of the system. In this section, the Sankey diagram is employed to illustrate the main power demands of an aircraft in the cruise condition. A typical example for a state-of-the-art transport aircraft is presented in

Fig. 1-3. The main power required for flight excludes auxiliary powers, such as the power needed for control surfaces, air conditioning, communication systems and in-flight entertainment. The power losses discussed in the subsequent paragraphs are based on current technologies [12, 13].

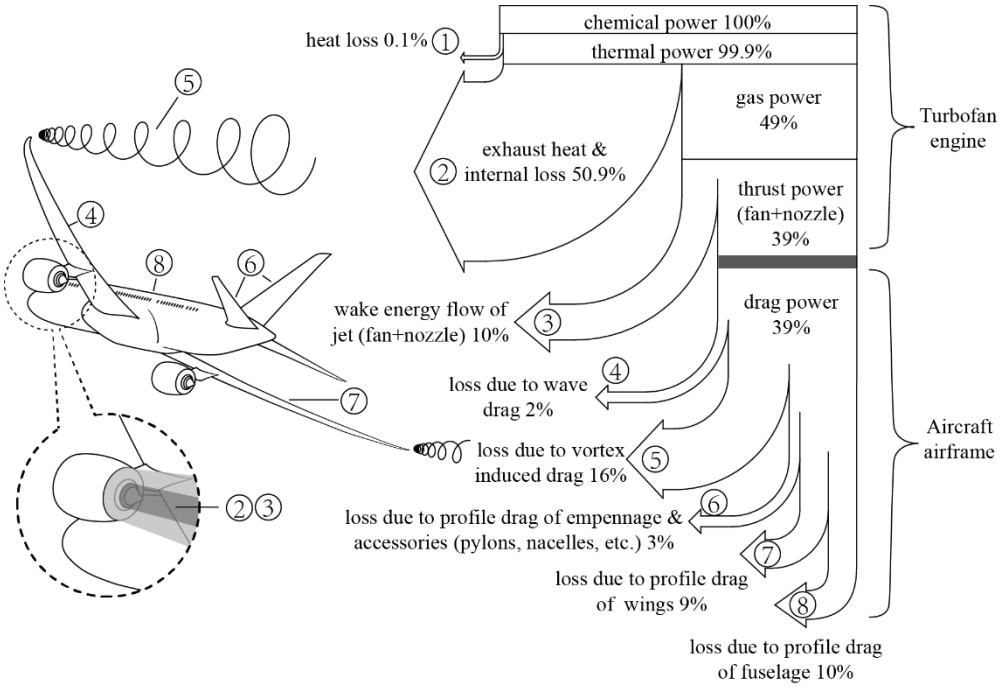

Fig. 1-3. Sankey diagram of an aircraft depicting the power losses at a typical cruise condition (figures adapted from [12, 14, 15]).

For a typical middle range aircraft, the chemical energy of the fuel is the primary energy source. The burning of the fuel takes place in the combustion chamber of the turbofan engine. In this process, the time rate of releasing the chemical energy is the chemical power, 99.9% of which is converted into the thermal power (or heat) of hot gas. The other 0.1% power is lost due to the incomplete combustion and as a heat loss, marked as ① in the Sankey diagram in Fig. 1-3. After that, the thermal power is further converted into a gas power by the gas turbine, which is based on the Brayton cycle [16]. The gas power is a useful power that could be harnessed by the low pressure turbine (*LPT*) and exhaust nozzle of the turbofan engine. For a state-of-the-art turbofan engine, about 49% of the chemical power is converted into the gas power, with rest of the power wasted in the form of exhaust heat and internal mechanical losses, denoted by ② in Fig. 1-3. The thermal performance of the gas turbine is described by a thermal efficiency, which is defined as the ratio between the gas power and the thermal power (Propulsive efficiency will be discussed in the following paragraph). It is worthwhile to mention that the improvement of the thermal efficiency made an important contribution to the increase in fuel efficiency of aircraft. After decades of development, it becomes increasingly difficult to improve the thermal efficiency of the gas turbine further. The Overall Pressure Ratio

(*OPR*) is approaching a limit, above which the increase in *OPR* will not lead to significant improvement in the thermal efficiency [17, 18]. On the other side, the thermal efficiency improvement by increasing turbine inlet temperature is limited by the technologies of material, thermal coating, and cooling of the turbine blades. Furthermore, it is also restrained by the possible future NOx emission regulations [7, 19].

As can be seen from the diagram, the gas power is converted into a thrust power, which is defined as the product of total thrust and the flight speed. The modern turbofan engines have high Bypass Ratio (*BPR*), which is the ratio of the mass flow going through the bypass fan to the gas turbine core. The thrust is generated by the fan bypass duct nozzle and the core exhaust nozzle. The thrust produced by the bypass is a function of the bypass ratio. In modern turbofan engines with high bypass ratio, the bypass duct nozzle produces approximately 75% of the total thrust and the core exhaust nozzle is responsible for the rest. As for the power conversion, the gas power in the engine is partially extracted by the Low Pressure Turbine (*LPT*) and then delivered to the fan (generating the large part of thrust power). The core exhaust nozzle uses the rest of the gas power to accelerate the core flow through the nozzle to produce rest of the thrust. In the Sankey diagram of in Fig. 1-3, around 39% of the chemical power is finally converted into thrust power. Approximately around 10% of the chemical power is lost due to the presence of the jet downstream of the engine (it will be called as a jet wake in Chapter 3 when introducing the wake system). In this research, this power loss is called as wake energy flow rate. The wake energy flow rate of the jet is marked as ③ in the diagram. To obtain a given thrust power, the bypass fan is more efficient than the core nozzle. This can be attributed to the fact that the jet velocity of the bypass fan is much lower than that of the core nozzle. A more detailed explanation is provided in the next chapter related to the characteristic of uninstalled propulsion. Given the fact that the thrust produced by the bypass fan is a more efficient process as compared to the core nozzle, an increase of *BPR* usually leads to a higher portion of the thrust power produced by the bypass, thus improving the aircraft fuel efficiency. This is evidenced by the development of the turbofan engine in the past decades when *BPR* increased substantially [12]. Nevertheless, a higher *BPR* leads to a large fan size, causing increased installation penalties such as engine/airframe interference[20, 21]. For an aircraft using very high *BPR* engines, installation penalties may be large than the benefit brought by the high *BPR*. This is elaborated in the subsequent section.

After the power conversion through the turbofan engine, the thrust power is utilized to propel the aircraft. At cruise condition, the thrust power is equal to a drag power, where the latter is obtained by multiplying the total aircraft drag by the flight speed. The drag power can be broken down into multiple power losses of the aircraft, as shown in Fig. 1-3.

For a modern transonic aircraft, about 2% of the chemical power (or approximately 4% of the total aircraft drag) is used to overcome the power loss pertaining to the shock wave, as denoted by ④ in Fig. 1-3. This power is called as the loss due to the wave drag, which is caused due to the compressibility effects of

airflow. The wing tends to experience an onset of shock wave over its upper surface, where the airflow accelerates to generate lift. The design of supercritical wing can reduce this loss [22, 23]. When the air passes over the wing/nacelle and fuselage/wing junctions of aircraft, the flow accelerates or decelerates due to the aerodynamic interference. The interference can increase the local Mach number and possibly cause a shock wave. The integration of components at the junctions is usually investigated in aircraft design to avoid harmful interference effects, reducing the loss due to the wave drag[23-25].

Along the power stream in the Sankey diagram, an important branch is related to the vortex-[15]induced drag which is a consequence of the wing generating lift force. The power loss due to vortex-induced drag refers to the kinetic energy of the vortex downstream the lifting surface [26]. This power loss is represented by ⑤ in the diagram. In the cruise condition where lift balances the weight of an aircraft, the power loss approximately accounts for 16% of the chemical power (or approximately 40% of the total aircraft drag). Some aircraft implement wingtip devices, aiming to decrease the power loss [27]. It is noted that the reduction in aircraft structural weight can be attributed to the saving of vortex-induced drag, hence the power loss.

The rest of the chemical power is used to overcome the loss caused by the airframe surface immersed in the air stream. This power loss is due to the profile drag and can be broken down in accordance with aircraft components. For aircraft with a typical tube-wing configuration, the power loss pertaining to the empennage and accessories (such us engine pylons, nacelles, etc.) is approximately 3% of the chemical power (or approximately 8% of the total drag). This branch in the diagram is marked as ⑥; the loss attributable to the wing surface is about 9% of the chemical power as denoted by ⑦ (or approximately 23% of the total aircraft drag); the loss for the fuselage is about 10% of the chemical power and shown as ⑧ (or approximately 25% of the total aircraft drag)[15, 28]. The losses due to profile drag depend on the type of the boundary layer formed on the airframe surface. It is preferred to have a laminar boundary layer than the turbulent boundary layer, as the drag produced by the turbulent boundary layer is higher than the laminar boundary layer. A modern passenger aircraft naturally maintains laminar flow over a small portion of the wing [29], and it is difficult to move the transition line further downstream. This has been acknowledged by the researchers working on boundary layer control techniques [30, 31], which aim to delay the boundary layer transition.

Figure 1-3 illustrates the power demands for a state-of-the-art aircraft in the typical cruise condition. The total power demand is the summation of all the listed power losses. These losses represent the inefficiencies of the system and indicate where opportunities lie to reduce the losses. In the past decades, many technologies have reduced power losses, but it becomes increasingly difficult to improve fuel efficiency with conventional technologies. Under this circumstance, it is imperative for us to look into novel technologies that can lead to the reduction of power losses, and thereby increase the overall efficiency.

1.3 Opportunities in propulsion integration

Among the many opportunities to increase fuel efficiency, the one brought by Propulsion Integration (*PI*) is of particular interest. This section looks at an aircraft in the cruise condition where the engine thrust is equal to the aircraft drag, as shown in Fig. 1-4. For aircraft with a conventional configuration where the propulsion system is installed underneath the wings, *PI* could lead to an unfavourable consequence of increasing the fuel consumption due to installation penalties, as compared to the performance of isolated airframe and propulsion system. However, a synergistic situation possibly exists and there might be opportunities brought by the unconventional configuration where the propulsion system is integrated with the aircraft in a favourable manner, such that power losses can be reduced.

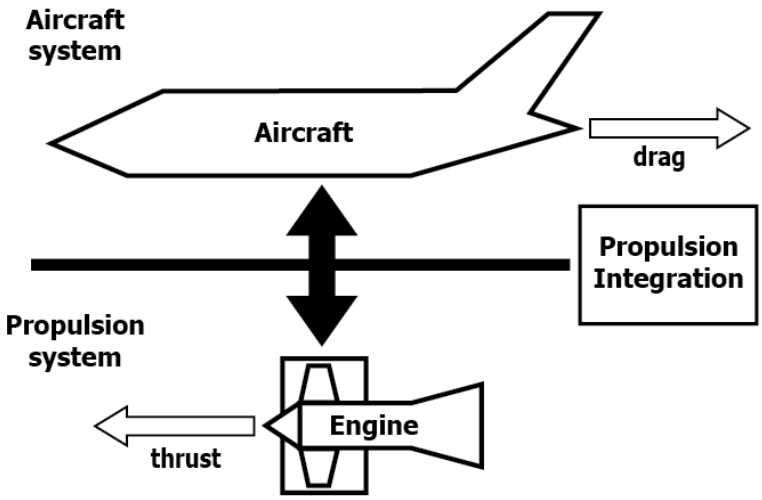

Fig. 1-4. Propulsion integration showing a decoupled airframe and propulsion system, and the main acting forces.

As discussed in the previous section, an important factor substantially improving the fuel efficiency in the past decades is the increase in *BPR* of the turbofan engine. However, increasing *BPR* beyond certain limits can lead to increased installation penalties. The trade-off between the two consequences of increasing *BPR* is illustrated in Fig. 1-5. For an uninstalled engine, the increase of *BPR* corresponds to a monotonic decrease of thrust specific fuel consumption. Therefore, the actual improvement of increasing *BPR* is different for the engine installed on an aircraft. The increase of *BPR* might lead to higher fuel consumption once an optimum value is exceeded. The difference in the improvement of fuel consumption is caused by the installation penalties that are represented by an installation drag in Fig. 1-5. It should be noted that this installation drag corresponds to multiple sources, such as the wave drag, profile drag, increase of engine weight, etc. The details of installation penalties are discussed in Chapter 2.

For a turbofan engine installed on an aircraft in a conventional configuration, the increase of *BPR* can reduce wake energy flow rate of (fan and core) jet to a certain extent but cannot eliminate this power loss completely. This is due to the principle of propulsion which states that the thrust produced by the engine is equal to a change in the rate of the momentum of air flowing through the engine. As a result, the jet wake has a higher velocity than the cruise velocity, thereby maintaining a finite value of the wake energy flow rate in the jet.

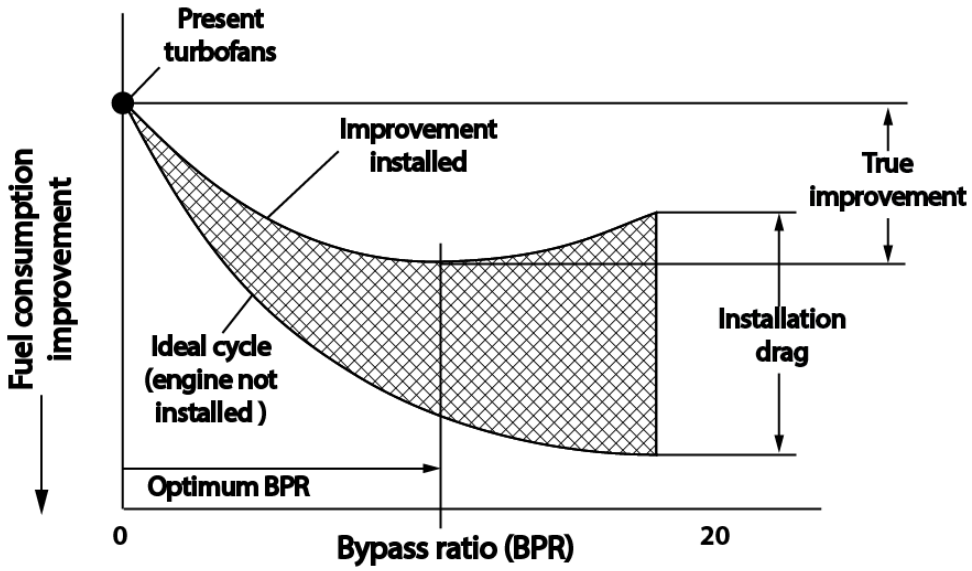

Fig. 1-5. The true improvement of increasing bypass ratio (adapted from reference [32]).

Besides increasing *BPR*, there are other means of reducing wake energy flow rate of the jet wake. Unconventional aircraft configurations utilizing favourable *PI* might offer an opportunity for reducing wake energy flow rate. Boundary Layer Ingestion (*BLI*) and Wake Ingestion (*WI*) are such possible configurations, as illustrated in Fig. 1-6. An aircraft utilizing *BLI* or *WI* is based on a special arrangement: The propulsion system is placed behind the aircraft to ingest the boundary layer or wake of the aircraft, rather than ingesting the free stream airflow as in the case of conventional configuration. The *BLI* denotes that propulsor ingests the boundary layer flow of the body (top in Fig. 1-6), while *WI* represents that the propulsor ingest the wake downstream of the body (bottom in Fig. 1-6). The main difference between *BLI* and *WI* is the distance between the propulsor and the body (There are slight distinctions in the theoretical and experimental analysis, these will be elaborated in Chapter 3 and Chapter 5). With this arrangement, the *PI* due to *BLI* or *WI* might possibly reduce the two power losses:

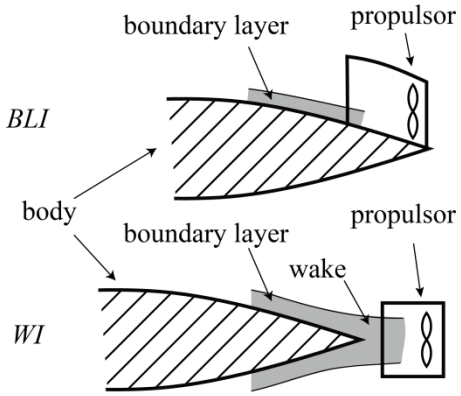

Fig. 1-6. Concepts of boundary layer ingestion and wake ingestion.

- The first power loss is the wake energy losses of the jet wake, marked as ③ in the Sankey diagram;
- The second power loss is the wake energy losses due to the presence of airframe wake, which is the wake downstream of the aircraft. This loss can be considered as a part of the loss due to the profile drag, as denoted by ⑧ in the Sankey diagram.

The two power losses pertain to the jet wake and the airframe wake respectively. For clarity, the jet wake is defined as the flow with a negative fluid velocity u w.r.t. the ambient air (u is negative when it is in the opposite direction of aircraft flying velocity). The airframe wake denotes the flow with a positive fluid velocity u w.r.t. the ambient air. Both types of wake can be found in the downstream region of aircraft. The photograph in Fig. 1-7 illustrates the contrails of a passenger aircraft. This aircraft contrail is a visible phenomenon that is closely related to the wake behind the engine and the airframe. The mathematical expressions and the physical interpretations of the power losses of wake are given in Chapter 3. These power losses are called as wake energy flow rates of the jet and airframe wake, and they are convected into the downstream wake and then dissipated in the atmosphere. A previous study [33] shows that *BLI* and *WI* can reduce wake energy flow rate of both the jet wake and the airframe wake. It is possible to reduce these two power losses to a minimum in an idealistic situation where the engine refills the airframe wake completely (the wake of a fuselage/body) into the free stream condition [34].

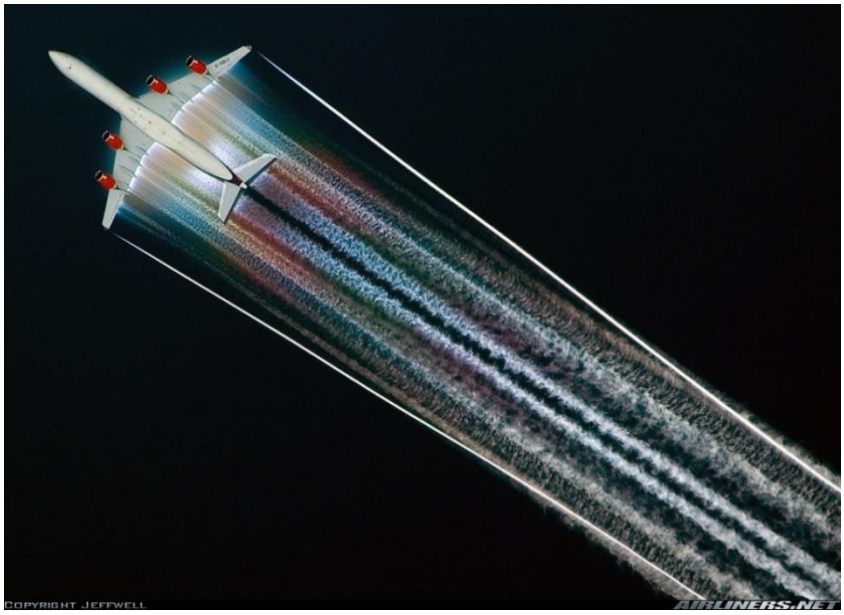

Fig. 1-7. Contrails depict the jet wake and airframe wake downstream of an aircraft (Airbus A340-642, photograph is taken during the flight at 9000m, courtesy of Jeffwell).

Besides the reduction of the two power losses, there are other possible consequences caused by *BLI* and *WI*, for instance, the reduction in weight due to the integration of engine and airframe structure, the occurrence of flow distortion, etc. These issues might also change the aircraft fuel efficiency and they are briefly discussed in Chapter 2. In this research, the main interests are limited to understanding the underlying physics of the *BLI* (and *WI*) configuration such that the two power losses are influenced by the configuration.

1.4 Research objective

In recent research programs on novel aircraft concepts, such as the *NASA* N+3 program, some of the aircraft concepts utilize the *BLI* configuration. Investigations show that *BLI* can improve the fuel efficiency. For example, the Boeing Blended Wing Body aircraft whose fuselage is merged with the wing uses *BLI*, as shown in Fig. 1-8 (a). The research on this aircraft indicates that *BLI* could lead to a 10% reduction in fuel burn [35]. The *BLI* was also chosen for the "Silent Aircraft" concept which aims to reduce noise emission, as illustrated in Fig. 1-8 (b). The study of this aircraft shows that the fuel consumption can be reduced by 3~4% due to *BLI* [34]. The *BLI* is also used in the *NASA* Hybrid Wing Body N3-X aircraft, as shown in Fig. 1-8 (c). The research carried on the aircraft configuration estimated that *BLI* could bring in a 7% reduction in required power [36]. The D8 aircraft, whose fuselage is characterized by a double bubble cross section also uses *BLI* to increase the total efficiency. This aircraft is presented in Fig. 1-8 (d). Numerical and experimental assessments claim that *BLI* could lead to a 6~9% reduction in power consumption [37, 38].

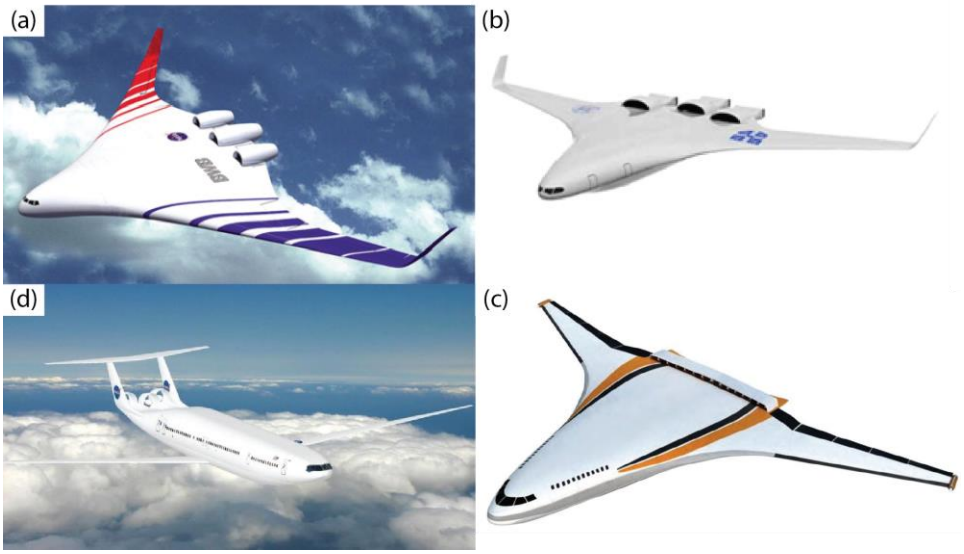

Fig. 1-8. Aircraft concepts utilizing *BLI*, clockwise from top-left picture: a) NASA/Boeing BWB 450 concept [35]; b) Silent aircraft [34]; c) NASA N3-X concept [36]; d) MIT D8 aircraft [40](courtesy of NASA).

Results of these research programs show that *BLI* might be a promising technology for reducing fuel consumption. Moreover, evidence could also be found in the field of marine propulsion. As early as the 19th century, W. Froude [39] studied a configuration in which a propeller was placed behind a ship hull. He acknowledged that such a configuration could bring in a positive effect of reducing shaft power as compared to the required power of the propeller in an isolated condition. Nowadays naval architects commonly use a term called as "wake fraction" to address this effect [40]. A modern ship is usually designed in such a way that the propeller is installed at the stern of the ship, as demonstrated in Fig. 1-9.

The above discussions indicate that open issues related to *BLI* still exist even if the results from the majority of studies suggest that *BLI* might be beneficial, these results are not coherent. To look into this discrepancy, it might be helpful to shift our focus from the results to the analysis methods that are used to quantify the benefit of *BLI*.

Including the work accomplished by naval architects, there have been abundant studies on *BLI*. Different methods have been used in these studies and can be broadly classified into three methods: The first method considers *BLI* as a propeller placed in a uniform stream with a lower velocity than the free stream velocity [40, 41]. This method is widely used in the study of ship propellers; it has also been utilized for an aircraft propeller located behind the fuselage [42] and for stern-mounted propellers in airships [43, 44]. The second method utilizes a thrust/drag bookkeeping system. In this methodology, the *BLI* is seen as a means of reducing the ram drag, the momentum flow measured at the engine inlet. This method has been used while analyzing some of the unconventional aircraft configurations such

as the Boeing *BWB* aircraft and the N3-X aircraft [36, 45]. The third method is based on power balance [33, 46, 47]. It has been used to investigate the *BLI* and *WI* as a means of reducing the power losses due to the wake behind the aircraft [33, 48]. This method has been used in the research of D8 aircraft [38]. In a recent study of *BLI*, an exergy based method is developed from the method based on power balance [47, 48], as a variant of the third method. These three methods are elaborated in the next chapter.

Fig. 1-9. A typical modern ship with its propeller placed behind its hull (courtesy of TOTE, Inc.).

In the previous studies on *BLI*, the various methods denote different interpretations of the physics involved in *BLI*. The difference in interpretation indicates that either the physics is not completely clear, or some aspects might be misunderstood. Particularly, there are some concerns in the aircraft design community that *BLI* might not be beneficial in increasing fuel efficiency [49, 50]. We can learn that there are some open issues regarding the understanding of *BLI*. These issues might be important to explain why *BLI* is not widely used for aircraft application. This research tries to make a contribution towards dealing with the open issues and to provide further insight into *BLI*. As a result, the objective of this research is **to enhance the understanding of *BLI*. Furthermore, the understanding shall be supported by comprehensive analyses with evidence from the numerical simulation and wind tunnel experiments**. For clarity, the following research questions are identified for the current research:

- **What are the mechanisms of *BLI* for the provided benefit?**
- **How large is the benefit of *BLI*?**

1.5 Thesis overview

A mind map is provided as assistance in dealing with the research questions, as shown in Fig. 1-10. The answers to the questions can be found progressively when the information in the branches is established. In accordance with the organization of this mind map, the thesis is structured as follows.

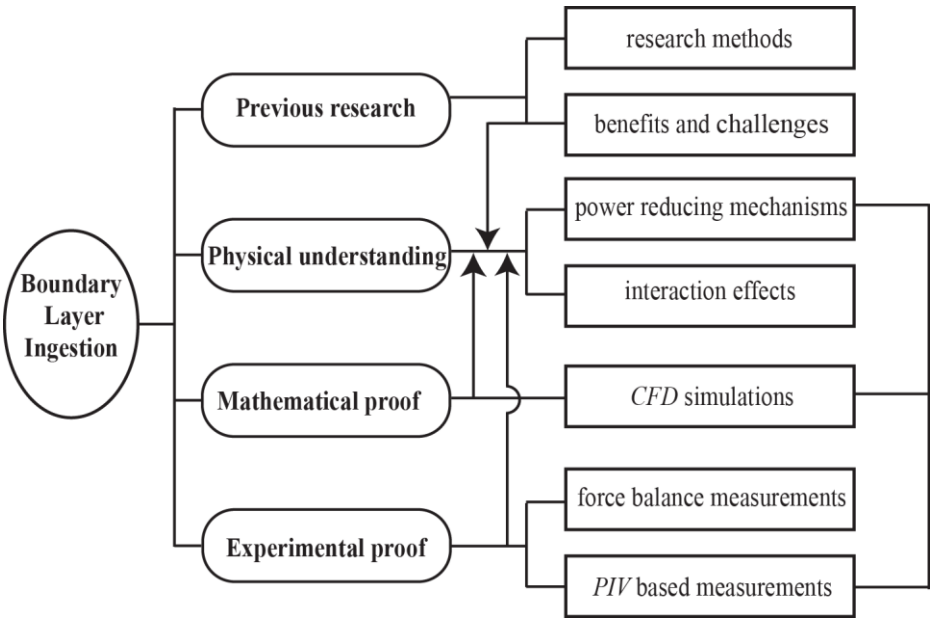

Fig. 1-10. Mind map of this research thesis on Boundary Layer Ingestion.

In this chapter, the motivation for reducing the aircraft fuel consumption is presented. The fuel efficiency for a state-of-the-art passenger aircraft is analysed by means of a Sankey diagram. Finally, the scope and objectives of this research are described and a thesis outline is provided.

The background of *BLI* is introduced in Chapter 2. It presents the issues of propulsion integration found in previous research. First, the propulsion integration for the conventional aircraft is discussed, together with a thrust/drag bookkeeping system. Then it gives a historical review of the research on propellers ingesting wake, with the research approach highlighted. After that, the possible benefits and challenges of *BLI* applied to the aircraft are presented.

Chapter 3 pertains to the physical understanding wherein the mechanisms of *BLI* are analysed. The method based on "power balance" is introduced, followed by a study on the vital "wake flows". The power conversion processes associated with *WI* is analysed, and the issues with respect to the highly integrated case of *BLI* are discussed. At the end of this chapter, the main findings from the theoretical study are provided.

In Chapter 4, the possible benefits of *BLI* are quantified through numerical simulations. A post-processing approach capable of calculating and analysing power conversions in *CFD* simulations is described. This approach is examined in the simulations of wake flows and then applied to the simple case of an isolated actuator disc and an isolated flat plate. Eventually, a numerical simulation is carried out for the *BLI* case that combines the actuator disc and the plate.

Chapter 5 deals with the experimental investigation carried out to illustrate the flow mechanisms involved in *BLI & WI*. A dedicated wind tunnel experiment conducted in a TU Delft wind tunnel is elaborated. The performance data is directly measured through the force balance measurement system, consistent with the approach used by other researchers. To enhance the understanding further, the experiments employed stereoscopic PIV to support the theoretical analysis.

Chapter 6 presents a synthesis of knowledge learned from the theoretical study, numerical simulations and experiments. Finally, the main conclusions of the research and recommendations for future research in this area are presented in Chapter 7.

Chapter 2 Propulsion integration

This chapter aims to present background knowledge of *BLI* for aircraft applications. Literature is reviewed for previous research related to relevant issues in Propulsion Integration (*PI*). The structure of this chapter is organised as follows: The first part briefly describes the typical performance of uninstalled propulsion. The second part introduces the issues of *PI* for the state-of-the-art conventional aircraft with engines installed under the wing. The third part discusses propellers ingesting the body wake, including ship propellers and pusher propellers applied for aircraft. Lastly, the possible benefits and challenges due to *BLI* are discussed.

2.1 Characteristics of uninstalled propulsion

This section aims to establish the fundamentals about *PI* for later discussions, by demonstrating the typical performance of uninstalled propulsion systems. Propulsion systems of aircraft refer to aero engines and their accessories, such as engine inlets, nacelles, etc. Within a propulsion system, propulsors (such as propellers and fans) are mainly responsible for generating the thrust force. The thrust occurs due to the pressure difference between the two sides of the propulsor.

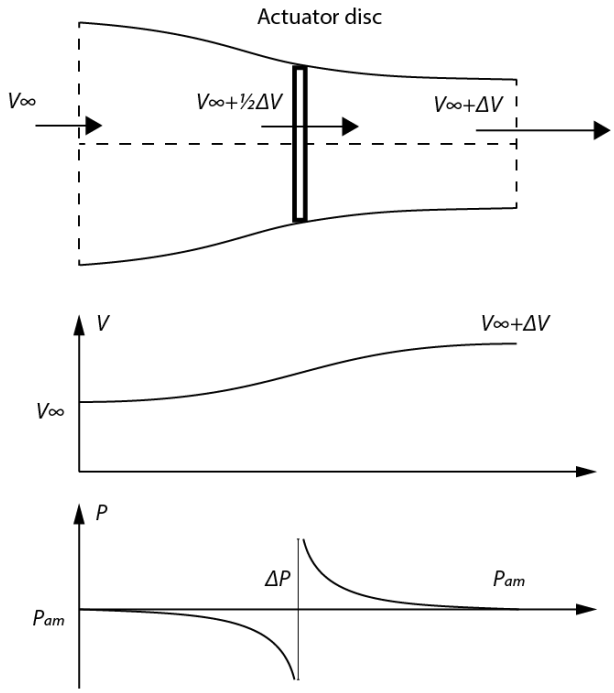

Fig. 2-1. Actuator disc model showing the static pressure along the axial (streamwise direction) coordinate and the change in flow velocity.

The typical performance of an uninstalled propulsor can be demonstrated by applying the momentum theory to an actuator disc model. The actuator disc model is introduced by R.E. Froude to analyse propellers [51], as shown in Fig. 2-1. When compared to an actual propeller, the classical actuator disc model has a few simplifications:

- The flow is considered to be uniform and in the axial direction.
- Pressure is uniform within the cross section of the stream tube.
- Viscous effects are neglected.

A commonly used propulsive efficiency is given by Froude, defined as the ratio of a thrust power TV_∞ over the mechanical power addition P_K. The simplifications made for the actuator disc model enable the thrust T being expressed as Eqn. (2.0). In this expression, $\dot{m}$ is the mass flow rate through the actuator disc model and ΔV is the velocity addition as shown in Fig. 2-1. P_K is given by Eqn. (2.1). As a result, the Froude's propulsive efficiency for this uninstalled actuator disc model can be reduced to an expression containing only the forward velocity (or the free stream velocity) V_∞ and the velocity addition ΔV, as given in Eqn. (2.2). This expression shows that the propulsive efficiency is less than unity when positive thrust is produced (the ΔV is positive and finite). Furthermore, this expression indicates that a small value of ΔV is preferred to maintain high efficiency.

$$T = \dot{m}\Delta V \tag{2.0}$$

$$P_K = \dot{m}\frac{1}{2}((V_\infty + \Delta V)^2 - V_\infty^2) \tag{2.1}$$

$$\eta_{uninstall} = \frac{TV_\infty}{P_K} = \frac{\dot{m}\Delta V V_\infty}{\dot{m}\frac{1}{2}((V_\infty+\Delta V)^2 - V_\infty^2)} = \frac{1}{1+\frac{\Delta V}{2V_\infty}} \tag{2.2}$$

Even though the actual physics of aero engines is more complicated than an actuator disc model, the simplified expression of Eqn. (2.2) can be used to demonstrate the Froude propulsive effciency of engines in the uninstalled condition. The typical three types of engines, namely turbojet, turbofan, and turboprop engines can then be differentiated by the extent of velocity addition ΔV. Figure 2-2 illustrates the propulsive efficiency curves for these engines.

- The turbojet engine maintains low propulsive efficiency within the subsonic regime. This can be attributed to the very high value of ΔV (the relative velocity between the high-speed jet and the free stream air).
- The turbofan engine is characterized by a moderate velocity addition due to lower ΔV, because of the lower velocity of the bypass air. As a result, the propulsive efficiency of the turbofan engine is better than a pure turbojet engine at the subsonic speed.
- The turboprop engine maintains the highest propulsive efficiency at the low airspeed due to the smallest value of velocity increase across the propulsor.

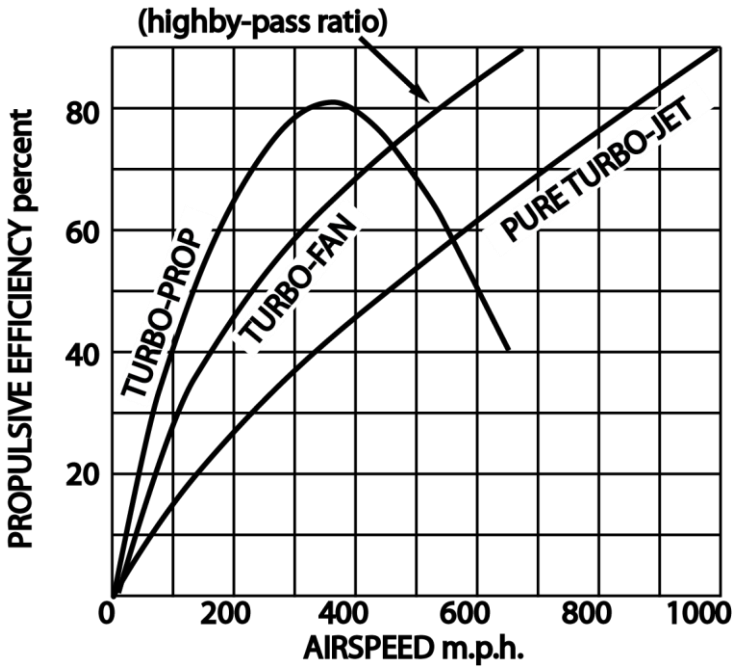

Fig. 2-2. Propulsive efficiencies for various aero engines, courtesy of Rolls Royce [52].

The subsonic transport aircraft no longer use turbojet engines due to their low propulsive efficiency. The Turbofan and Turboprop engines are widely installed in transport aircraft. In summary, the propulsive efficiency of uninstalled propulsors mainly depends on their velocity addition and the speed regime where they operate.

2.2 Introduction to propulsion integration

In the aircraft industry, engines and aircraft are designed and developed separately. This separation allows engineers to address a huge amount of technical issues through the corresponding disciplines. On the other hand, airline companies welcome the separation because this allows the interchangeability of aircraft and engines. Nevertheless, the separation is not always beneficial. Modern subsonic aircraft widely apply similar configurations in which turbofan or the turboprop engines are installed on the wing, as can be seen from Fig. 2-3. In these aircraft configurations, the integration of propulsion and airframe possibly changes the characteristic of the propulsion system and aircraft. This issue is known as *PI*, and typical consequences are:

- Engine thrust is changed (usually reduced) from that of the uninstalled condition;
- Aircraft drag is different (usually increased) from that of a clean airframe without engines.

Fig. 2-3. Modern turbofan (top) and turboprop (bottom) engine aircraft commonly place the propulsion system underneath the wing (Courtesy: Boeing and Airbus).

The aforementioned consequences might not be considered significant in the past because of the week interference between the flowfield around the wing and the flow due to the propulsion system. Nevertheless, this is not the case for modern turbofan engine aircraft. Section 1.3 introduced an impact of *PI* for aircraft with turbofan engines, that the increase of *BPR* of turbofan engines causes the higher installation drag. This installation penalty might outweigh the improvement of engine efficiency. The listed example shows the impact of *PI* on aircraft fuel consumption. It is in our interest to investigate the issues of *PI* with more details.

2.2.1 Thrust/drag bookkeeping

It is important to measure the thrust and drag accurately before we quantitively discuss the influence of *PI*. It seems straightforward to use sensors to measure these forces directly, for instance, measuring the apparent force acting on the trunnion of the connections of the engine. This direct measurement is indeed used in the ground test of aircraft engines, as shown in Fig. 2-4. However, this approach is seldom used in an in-flight test, because the complex structural supports and connections are unacceptable for a flying aircraft. The in-flight test usually employs an indirect measuring technique.

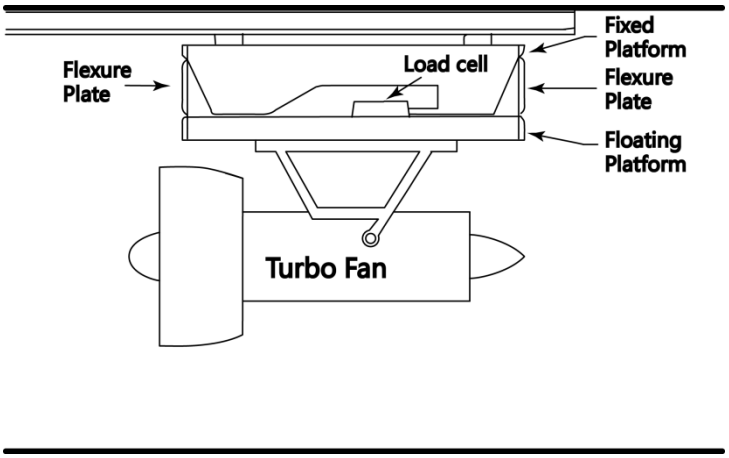

Fig. 2-4. The scheme of a test cell for a turbofan engine (adapted from [53]).

An indirect measurement can quantify the thrust force of an uninstalled engine by analysing the flow through the engine. However, it is difficult to separate the thrust from drag for an aircraft with the engine installed. Because a substantial portion of the thrust can be distributed over the airframe surfaces external to the engine [21, 54]. Under this circumstance, a so-called thrust/drag bookkeeping system is introduced to measure the thrust and drag in an indirect manner.

A thrust/drag bookkeeping system is demonstrated for a simplified aircraft model whose schematic is shown in Fig. 2-5. Two cross sections are specified in this schematic, namely an engine inlet and an engine exit. In the bookkeeping system, the thrust denotes a net thrust T_{net}. As given in Eqn. (2.3), T_{net} is the difference between a gross thrust T_{gross} and a ram drag D_{ram}, that are measured as the momentum flow rate at the two cross sections. D_{ram} corresponds to the engine inlet, and T_{gross} refers to the engine exit. For turbofan engines, the gross thrust can be further divided into the contributions of the fan (bypass) and the gas turbine (core). On the other side, the difference between T_{net} and D (aircraft drag in this case) denotes the net force N imposing on the entire aircraft, as shown in Eqn. (2.4). It is noted that the value of N corresponds to the flight status of the aircraft. A positive value stands for the state of accelerating and a negative N is for decelerating. In the condition of cruise, N shall be zero.

$$T_{net} = T_{gross} - D_{ram} = (\dot{m}V_{out} + P_{out}A_{out}) - (\dot{m}V_{in} - P_{in}A_{in}) \tag{2.3}$$

$$N = T_{net} - D \tag{2.4}$$

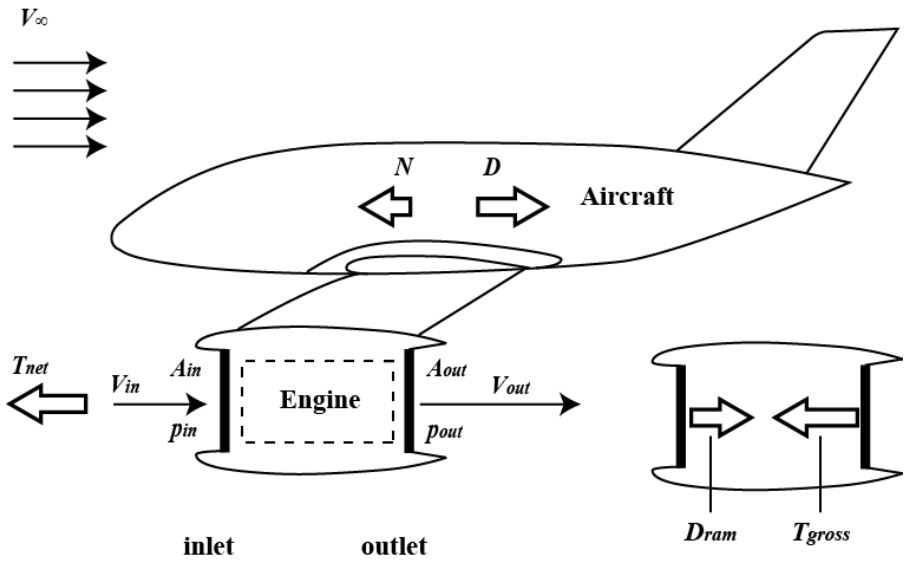

Fig. 2-5. Schematic of a simplified aircraft model with an engine installed.

A bookkeeping system shall maintain equilibrium among the net force, the net thrust, and the aircraft drag. The bookkeeping system is not only used for the actual in-flight test but also adopted in *CFD* simulations and wind tunnel tests [32, 55-57]. The bookkeeping systems used in the industry might be slightly different from each other [54].

An example is given to demonstrate how to apply a thrust/drag bookkeeping system. In wind tunnel tests, it is possible to evaluate the impact of *PI* for an actual passenger aircraft. This is enabled by engine simulators which are installed in a subscale aircraft model. In order to provide thrust to the aircraft model, engineers usually employ one type of engine simulators called the Turbine Powered Simulator (*TPS*). It can be seen as a miniature turbofan engine, except that the simulator is powered by compressed air rather than burning fuel. The *TPS* has a similar architecture as turbofan engine, shown in Fig. 2-6. The airflow through the *TPS* also consists of core flow and bypass flow. The core flow corresponds to the compressed air which drives the turbine, and the turbine exit vents the core flow to the air stream of the wind tunnel. The bypass flow through the fan is responsible for the major part of thrust.

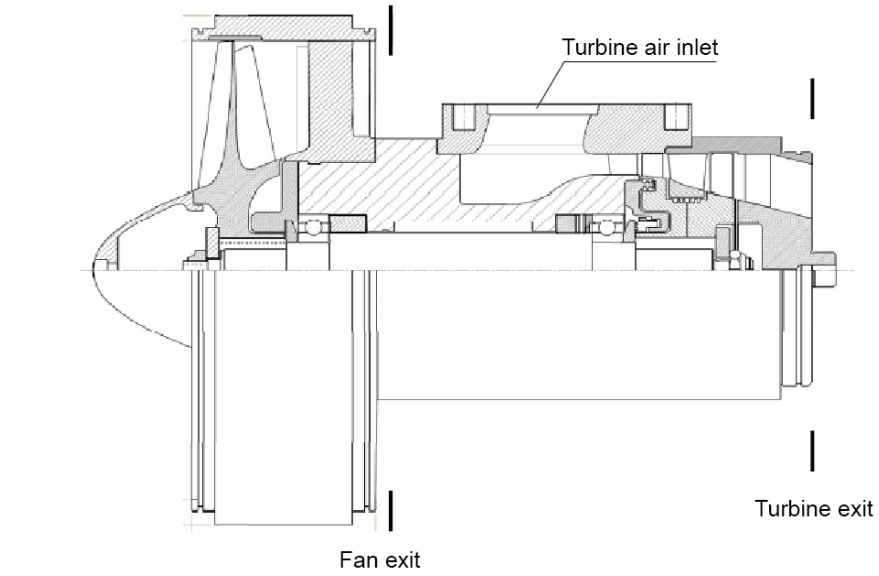

Fig. 2-6. Cross-sectional drawing of a Turbine Powered Simulator (*TPS*) [32].

To mimic an actual aircraft, engine simulators are installed under the wing of the aircraft model, as shown in Fig. 2-7. During the test, compressed air is supplied to the *TPS*. The air feed tube is placed inside the aircraft model to avoid aerodynamics interference, and the other side of air feed tube is linked to the pressure tank external to the wind tunnel. The entire aircraft model is supported by a strut and connected to a balance such that the aerodynamic force (net force) and moment imposed on the model can be measured. Total pressure rakes (or probes) are placed at the fan exit and the core exit of the *TPS*, in order to measure the gross thrust of these engine simulators.

Fig. 2-7. An aircraft model with *TPS* tested in a wind tunnel [32].

The thrust/drag bookkeeping applied to an aircraft model is presented in Fig. 2-8. Balance load is measured through the internal balance which supports the entire aircraft model (corresponding to the net force of aircraft, it shall be close to zero in the simulated cruise condition); Airline residual load is caused by the high-pressure air supply which imposes a significant change of momentum. This load shall be measured as the momentum change and included in this bookkeeping system; Core and fan gross thrusts are obtained as the momentum flow at two sections of the *TPS*, namely the core exit and fan exit; Ram drag is measured at the fan inlet of *TPS*; Drag corresponds to the drag force acting on the airframe of the aircraft model. Because these forces can be measured through instruments, (airframe) drag can be indirectly obtained as a force to maintain equilibrium among the aforementioned forces. By using this thrust/drag bookkeeping system, thrust and drag can be determined.

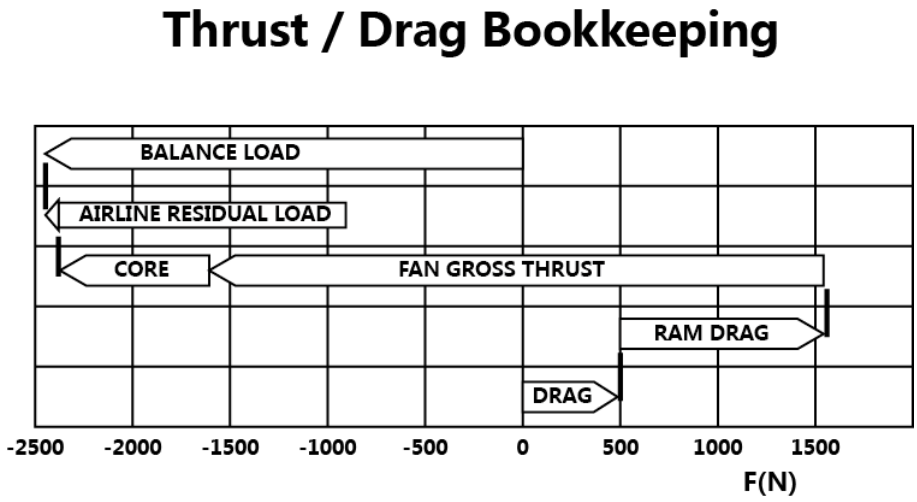

Fig. 2-8. An example of thrust/drag bookkeeping, adapted from [32].

Once a bookkeeping system measures the thrust and drag, engineers follow a test program to evaluate different impacts of *PI*. The type of impacts depends on the specific condition of the test programme. In the example of wind tunnel test, typical effects of *PI* are listed below [32, 57]:

- Installation effect: This effect can be quantified by comparing the forces acting on two model configurations, namely the powered model with engine simulators and the clean model without engine simulators. The expression of installation effect is given in Eqn. (2.5).

$$F_{install} = F_{powered\ model} - F_{clean\ model} \tag{2.5}$$

- Power effect: The power settings of *TPS* is changed for the powered model, with respect to the idle power setting. This effect is evaluated at zero speed of wind. The forces acting on the model are measured with different power

settings of *TPS* such that the influence due to power changing can be evaluated.

- Jet interference: Jet interference is assessed at a finite wind speed, corresponding to a simulated flight condition. The wind speed differentiates this effect from the aforementioned power effect. The power setting of *TPS* is varied for the powered model and the forces acting on the model are measured accordingly. As a result, the impact of jet interference can be determined.

As discussed, the effects of *PI* can be quantified through a test program. In practice, engineers usually combine a thrust/drag bookkeeping with a drag breakdown system to investigate more detailed effects of *PI* [20]. The issues of *PI* can be complicated and diverse for the aircraft with different propulsion systems. The following sections briefly discuss the aerodynamic aspects of *PI* for current transport aircraft using turbofan and turboprop engines.

2.2.2 Propulsion integration for aircraft with turbofan engines

Aircraft using turbofan engine are usually designed to fly at a high subsonic Mach number (above 0.7), where turbofan engines maintain high propulsive efficiencies. For such an aircraft, the pylons physically connect the engines to the wing. Engines are surrounded by an aerodynamic shroud, known as a nacelle, as depicted in Fig. 2-9. For a turbofan engine, the fan is its main propulsor generating thrust. The *BPR* is the ratio of airflow through the fan to the airflow through the core. Higher *BPR* indicates more thrust is produced by the fan, this generally leads to lower jet velocity and higher propulsive efficiency [16]. Over the past decades, *BPR* of turbofan engines has been increased significantly [12]. As introduced in Chapter 1, an installation drag should be accounted for when evaluating the real improvement of increasing *BPR*, particularly in the cases where ultra-high (12~15) *BPR* is considered [28, 58].

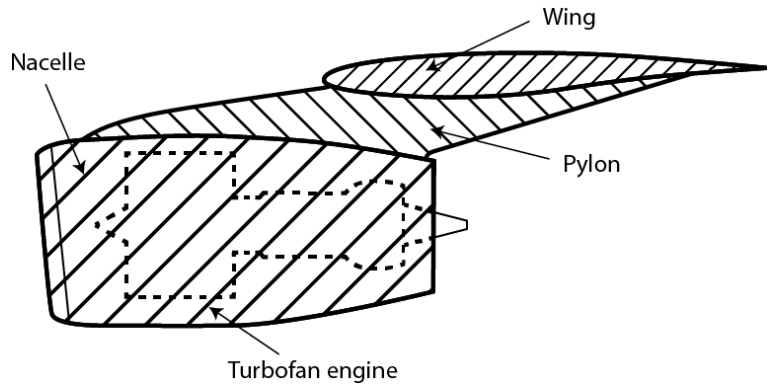

Fig. 2-9. A turbofan engine installed under the wing.

For current aircraft, the installation drag typically makes about 6~8% of the total aircraft drag [20, 55, 56, 59] in the cruise condition. The installation drag consists of

the following contributions: namely the clean drag of pylons and nacelles, and an interference drag [54-56, 59]. The clean drag is the drag of the pylon and nacelle measured at their isolated condition and is associated with their respective wetted area. While the interference drag is due to the aerodynamic interference between the wing, the engine, the pylon, and the nacelle.

The interference drag is related to *PI*. The drag is caused by the forced mixing of air flows between the involved components. Aerodynamic interference is of particular interest when designing an aircraft flying at a high subsonic Mach number. The wing of the aircraft generates lift by accelerating the surrounding airflow whose velocity might exceed the sonic speed at the wing's upper surface, causing a shock wave. The aerodynamic interference further strengthens the shock wave, when the airflow is accelerated due to the presence of the engine. For example, in *CFD* simulations of a two-engine aircraft with a low wing configuration (*ALVAST* model), the results show that the engine installation increases the coefficient of wave drag by 25% for the entire wing [20]. This is evidenced by the slightly larger supersonic region over the wing, as shown in Fig. 2-10.

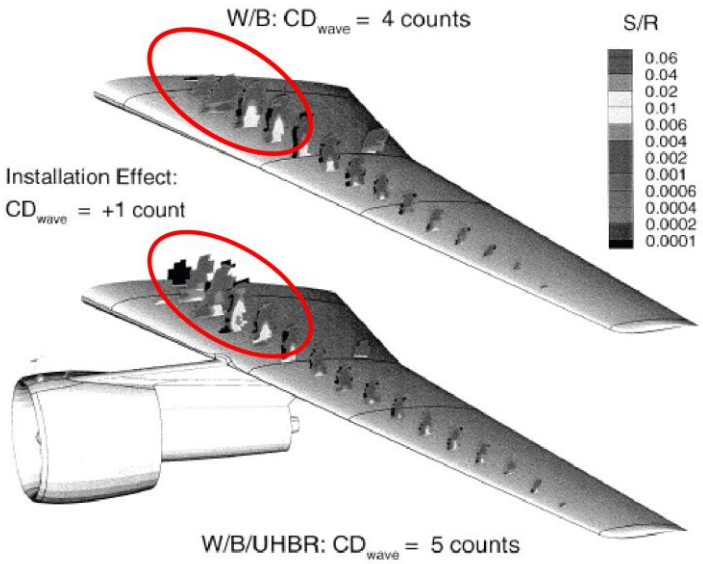

Fig. 2-10. The effect of ultra-high *BPR* engine installation on wave drag (a CFD simulation at Mach =0.75, CL=0.50 FPR=1.72, Re=4.3 million, the contours denotes entropy production in the supersonic region, figure from [20].

The interference drag depends on the engine position and engine type. It is preferred to place the engine in a forward position relative to the wing, as shown in the studies of a transport aircraft using two VHBR turbofan engines (*DLR-F6* aircraft model) [58, 60]. The engine nacelle changes the airflow over the upper surface of the wing. The jet of the engine mainly influences the airflow over the lower surface of the wing. In the research on a transport aircraft using UHBR turbofan engines, results have shown that the longitudinal position of the engines

can influence the mission fuel burn by 6.4%~3.7% [55]. The significant large sonic region appears when the engine is placed too close to the wing. For a transport aircraft using a high wing configuration, wind tunnel experiments showed that it might be beneficial to place engines in the most forward and lowest vertical position to the wing [25].

Besides the interference drag, *PI* causes alternative aerodynamic interference effects. For example, the lift distribution of the wing can be changed by the presence of the nacelle. In return, the pressure distribution over the nacelle surface is also altered by wing [55, 56]. Studies [20, 28] have shown that these effects have a relatively small impact on fuel consumptions, thus they are not discussed further in this thesis.

The nacelle plays an important role in generating the installation drag. Thus, engineers consider abandoning the aerodynamic shroud over the fan when further increasing *BPR*. Such consideration leads to the propfan and the open-rotor designs for novel aero engines [61, 62]. These engines share many similarities with the turboprop engines.

2.2.3 Propulsion integration for aircraft with turboprop engines

Turboprop engines are usually installed on transport aircraft flying at the low Mach number (below 0.7), as discussed in Section 2.1. Propulsion integration for these aircraft refers to the aerodynamic interference between the propeller and the wing [63] as many of these aircraft apply the same configuration that the tractor propellers are placed ahead of the wing. The propeller-wing interference can be grouped into two: The effect of propeller slipstream on the aerodynamic characteristics of the wing, and the impact induced by the wing on propeller performances.

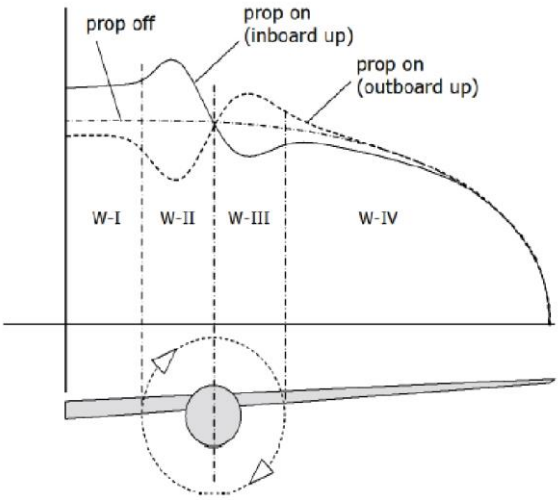

Fig. 2-11. Lift distributions of the wing affected by propeller slipstream [63].

Turboprop engines generate propeller slipstream impinging on the wing. A notable effect is the change of the lift distribution of the wing. The velocity of slipstream can be decomposed into axial and swirl velocities. For the wing section immersed in the slipstream, the axial velocity leads to an increase of the local lift coefficient. The swirl velocity alters the distribution of lift coefficient in a rotationally symmetric pattern. The combined effect is shown in Fig. 2-11. The lift distribution can be different due to the propeller rotation direction. Studies have shown that the inboard up rotation (clockwise rotation for the propellers installed on the right wing observed from the back view) of propellers can increase the lift-to-drag ratio of aircraft [63-65].

Propeller-wing interference not only changes the aerodynamic characteristics of the wing but also influences the propeller performance, altering the thrust and torque imposed on the propeller. When the wing generates lift, bounded vortex induces an upwash velocity in front of the wing, where the propeller is installed. The induced velocity increases its angle of attack of the propeller, causing a non-uniform loading of the disc swept by propeller blades [63]. This upwash due to interference is similar with that of changing the propeller's incident angle, and both effects can lead to a decrease in propeller efficiency, as shown by the plot in Fig. 2-12 [58]. Additionally, Propeller-wing interference causes another effect that the wing can straighten the swirling flow of the slipstream. Studies show that swirl recovery vanes installed after the propeller can improve the propeller efficiency by a few percent [66, 67]..

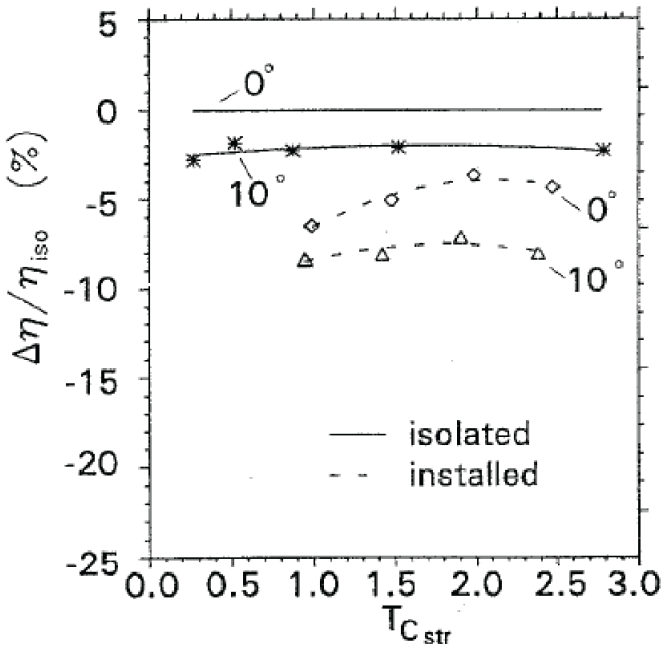

Fig. 2-12. Propeller efficiency in the installed and isolated conditions (results are presented by the change of efficiency $\Delta\eta/\eta_{iso}$ versus thrust coefficient T_{Cstr} at two angles of attack (0 °and 10 °), source: [58]).

2.3 Historical survey of propellers in the wake

As discussed, *PI* leads to performance degradation for aircraft with engines installed on the wing. However, it does not mean that *PI* is necessarily harmful to all aircraft configurations. With different engine arrangement, it is possible to obtain favourable *PI*, thereby improving fuel efficiency [68]. An example of such a favourable *PI* is a configuration in which the propellers are placed in the airframe wake. A favourable effect obtained from this configuration has been acknowledged by naval architects and early aerodynamicists [69]. This section briefly discusses the effect of ship propellers and pusher propellers installed on aircraft.

2.3.1 Ship propellers

For ships, the propellers are generally located behind the hull. In the field of marine propulsion, it is well known that the interaction between propeller and hull wake might lead to a performance improvement [40, 49]. This effect had been realized and studied by the pioneers of naval architecture, W. Froude [39]. As early as 1865, he made a remark:

…I think it is clear, then, that if we could place the propeller in a current moving in the direction of the ship, quite irrespective of any other operation on the ship, that propeller would gain an advantage by working in such a current; whatever the forward velocity of the current, it would be so much saved to the power of the engine…

Froude had demonstrated the significant impact of the propeller-hull interaction through towing tank experiment [70, 71]. He first tested a propeller without hull model and adjusted the propeller rotational speed to produce zero thrust. Then the hull model was placed in front of the propeller with equal rotational speed. The entire combination was towed in the tank at the same forward speed. In the combined configuration, the propeller produced more thrust of about 20% of the hull resistance force. Depending on the hull shape, the other effect found in his experiment was the increase in hull resistance due to the propeller operation.

He broke down the complicated problem into solvable parts, first the propeller in isolation and then behind the hull. His son, R.E. Froude, further advanced this method [70]. In this method, the efficiency of the forward moving propeller in still water is obtained as $\eta_{uninstall}$. Then, a wake factor was introduced as $\frac{V_\infty}{V_b}$. In this wake factor, V_∞ is the model speed and V_b is the speed of the hull wake. The wake factor aims to address the effect when the propeller is placed in the wake, allowing to obtain a new efficiency $\eta_{installed}$, as shown in Eqn. (2.6). This method assumes that $\eta_{uninstall}$ remains the same in a hypothetical uniform wake flow. The wake brings gain in the overall efficiency: $\eta_{installed}$ is greater than $\eta_{uninstalled}$ since V_∞ is greater than V_b. The wake speed V_b is specified by a "wake fraction" with expressions given by R.E. Froude and D.W. Taylor [49, 71]. In the terminology of modern naval architecture, Relative Rotative Efficiency is used to correct difference in the efficiencies of the propeller operating in open water and the propeller operating behind the ship hull. This efficiency corrected the trust, revolutions, and the actual torque delivered to the

propeller, to address the flow variation at each radii of the propeller in the mixed wake and open water flows. Assumed to be scale independent, this efficiency is obtained from small-scale model test, and then used for full size ship propellers.[41, 72].

$$\eta_{install} = \eta_{uninstall} \frac{V_\infty}{V_b} \tag{2.6}$$

Apart from the gain due to wake, another effect due to propeller-hull interaction is the increase in hull drag due to the action of the propeller. Froude described it as "augment of resistance", and then replaced it by "Thrust deduction" in modern naval architecture. This "augmentation" and "wake" together constitute the "hull efficiency" which remains in use today [40, 41, 72]. The hull efficiency of modern ships is usually a little greater than unity, meaning that the gain due to wake is more dominant. Because of this overall benefit, nowadays naval architects universally place ship propellers behind the ship hull.

2.3.2 Pusher propellers for aircraft

Similar to a ship propeller, a propeller installed in an aircraft is called pusher propeller when it is placed behind a body (fuselage). When studying pusher propellers, aerodynamicists acknowledged the work done by naval architects and appreciated the favourable propeller-hull interaction obtained by ship propellers. For example, Durand [42] acknowledged a beneficial interference between a pusher propeller and the body. He introduced an approach to deal with the interference by considering the pusher propeller operating in a region of reduced velocity, as can be seen from Fig. 2-13. Betz [73] studied a pusher propeller which refilled the wake of a body. Furthermore, he explained that the gain in efficiency comes from the reduction of kinetic energy in the wake.

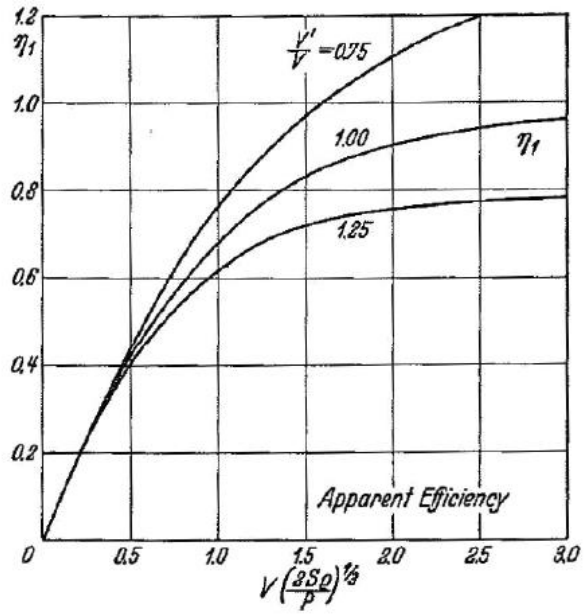

Fig. 2-13. Durand's method obtains (apparent) efficiency increases by assuming a reduced velocity *V* ´(reduce from the freestream velocity *V*) [42].

Even if aerodynamicists acknowledge the favourable interaction for pusher propellers, they are concerned that pusher propellers are too different from ship propellers and the actual benefit for pusher propeller aircraft might be insignificant. For example, Durand pointed that the diameter of aircraft propeller is much greater than the fuselage diameter, and the drag of the fuselage is only a fraction of aircraft's total drag that should be overcome by the thrust of the propeller [42]. Betz was concerned that the gain from the propeller resulting from reduced velocity is exactly cancelled out by an increase in the drag of the body [73]. Duncan [49] commented that the gain obtained by pusher propellers might be small due to the small averaged wake velocity. His alternative concerns about pusher propellers were less ground clearance and the vibration problems suffered by propellers operating in the wake.

Throughout the history of propeller-driven aircraft, pusher propellers have always been compared with the propellers placed forward (tractor propellers). As a result, there have been abundant studies on this topic. Miley and Lavante [74] reviewed 121 references about investigations on *PI* for propeller-driven aircraft. These investigations were carried out in the period from 1936 to 1980 and most of them were experimental tests. A large number of studies showed that most of the pusher propellers have a few percent higher efficiencies than tractor propellers [75].

Fig. 2-14 XB-42 in 1944 showing the integration of fuselage and counter-rotating pusher propellers [76].

These previous studies show that pusher propellers might have small or marginal benefit in performance. These studies might partially explain why most of the propeller-driven aircraft usually use tractor propellers. The actual reasons why pusher propellers are seldom in use are due to other associated penalties, such as ground clearance, vibration, engine cooling, etc. Nevertheless, there are exceptions to these concerns. For instance, the XB-42 aircraft is such a special aircraft. This aircraft was an experimental aircraft driven by two contra-rotating pusher propellers installed aft of its fuselage [76], as depicted in Fig. 2-14.

XB-42 had an exceptional aerodynamic performance when compared to other aircraft in its class. The performance can be evaluated by Aerodynamic Efficiency Index (*AEI*), defined as Maximum Take-Off Weight (*MTOW*) multiplied with the cruise speed and divided by the total shaft power of engines P_W, as shown in Eqn. (2.7). The *AEI* is in proportion to the aircraft lift-to-drag ratio and propulsive efficiency in the cruise condition, therefore, includes the performances of the aircraft airframe and propeller. The XB-42 is compared with several aircraft having an identical tube-wing configuration, with two tractor propellers mounted on the wing, as shown in Table 2-1. The listed aircraft are in the same class of *MTOW* (10~25 tons), but have different missions, ranges, and engine types. For the 1940's aircraft using piston engines, B-25 and Mosquito have similar *AEIs* of around 1.7. For the modern regional passenger aircraft and cargo planes using turboprop engines, their *AEIs* are within the range of 1.8 to 2.3. The XB-42 has an *AEI* of 3.0, which is about 30% - 45% more than that of other aircraft.

$$AEI = \frac{MTOW \times V_{cruise}}{P_w} \propto {}^{L}/_{D} \times \eta_p \tag{2.7}$$

Table 2-1. *AEI* comparison among propeller-driven aircraft

Aircraft	MTOW (*ton*)	P_W (shaft Power (*hp*)	Cruise Speed(*km/h*)	AEI
XB-42	16.1	2650	502	3.0
B-25J	15.9	3400	370	1.7
Mosquito B Mk XVI	11.4	3420	500	1.7
SAAB 340 B	13.2	3500	467	1.8
ATR 42-500	18.6	5032	554	2.0
C-295M	23.2	5290	480	2.1
Fokker 50	20.8	5000	530	2.2
SAAB 2000	22.8	8304	665	1.8
ATR 72-600	22.8	4950	509	2.3

Smith [69] studied the benefits obtained by propulsors (propellers and fan) due to Wake Ingestion (*WI*) for aircraft application. He showed that power consumption might be reduced up to 20% when a propulsor ingests the wake. The pusher propellers of XB-42 may gain from the wake of the aircraft fuselage, and the high *AEI* of this aircraft might be partly attributed to the benefit of wake ingestion. This aircraft is an extraordinary example against the concerns about pusher propellers might not be beneficial.

As discussed in Chapter 1, favourable *PI* is key to improving the fuel efficiency of state-of-the-art aircraft. *BLI* (or *WI*) as a means of bringing favourable *PI* was introduced to some novel aircraft in recent research programs [10]. These novel aircraft have different configurations and their missions vary slightly. Numerous studies have investigated the impacts of *BLI*. Some of the results are summarized in the following two sections about the possible benefits and challenges when *BLI* is applied to future aircraft.

2.4 Possible benefits of boundary layer ingestion

Comprehensive studies have quantified the impact on the power consumption caused by *BLI*. The so-called power saving coefficient, defined by Smith [69], is usually used as a metric to evaluate the influence. This parameter is defined as the ratio between the power reduction and the reference power consumption. Power saving (coefficient) due to *BLI* was found to be positive for many aircraft concepts, such as the *BWB* aircraft [35], Silent aircraft [34], D8 aircraft [37, 38], etc. As compared to the baseline condition (propulsors in the isolated condition), power saving (or fuel saving) due to *BLI* were found to be in a range from 3% to 10% for

the whole aircraft, as discussed in Chapter 1. Besides the studies on novel aircraft concepts using *BLI*, some dedicated experimental studies investigate the impact of *BLI* on the power, by placing a propulsor and a body in *BLI* and non-*BLI* configurations. For example, a wind tunnel test in *ONERA* placed a ducted fan and a body of revolution in various configurations, showing the power saving of about 20% in the *BLI* configuration [77]. In another wind tunnel test, the body of revolution is tripped with a turbulent boundary layer, and maximum power saving due to *BLI* was found 25% [78].

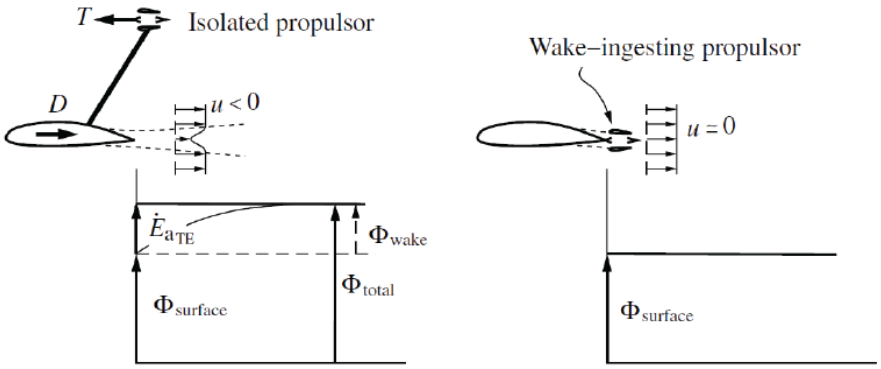

Fig. 2-15. Comparison between isolated propulsor and wake ingesting propulsor by using power balance method [33] (*Φ* is the viscous dissipation to be elaborated in Chapter 3).

These studies show that *BLI* might be a promising concept for future aircraft. More importantly, the studies indicate a progressively enhanced understanding of the physics of *BLI*. In early research related to the method introduced by naval architects, the gain due to wake ingestion depends on the reduction of the inflow velocity to the propellers. In the later studies employing a thrust/drag bookkeeping system, the benefit due to *BLI* was attributed to the reduction of ram drag (momentum inflow of propulsors). In recent studies utilizing the method based on power, the benefit of *BLI* is considered as the reduction of the power pertaining to wake.

The method based on power was introduced by Drela [33], his power balance analysis focuses on mechanical power. Arntz, et al. [47] advanced this method by including thermal power. According to Drela, the power saving in *BLI* is due to the reduction in the viscous dissipation Φ of the jet wake and body wake, as demonstrated in Fig. 2-15. This method is relatively new and introduced with more details in Chapter 3.

2.5 The challenges of boundary layer ingestion

2.5.1 Inlet distortion

In the research on novel aircraft configuration utilizing *BLI*, several technical challenges have been identified. One of the critical issues raised for all aircraft is the

total pressure distortion caused by the non-uniform inflow containing the near wall low-velocity stream and the high-velocity free stream. Once the compressor of aero engines ingests the highly distorted flow, the stall margin is reduced substantially and therefore rotational stall, surge or severe engine failure might occur.

The total pressure distortion is evaluated at engine face by employing a rake which consists of a circumferentially and radially distributed total pressure Pitot array. There are various methods to describe the distortion level. Circumferential Distortion Intensity Descriptor (*DPCP*) [79] is generally used as the industry standard and Distortion Coefficients method is also widely accepted [80]. In general, inlet distortion can be classified into circumferential and radial distortion. The former is quite hazardous for the engine because the circumferential variation leads to the change in the blade loading for each revolution. The latter is less harmful to the rotating blade of the engine. In the *BWB* aircraft research program, efforts were made to develop an inlet for *BLI* to manipulate the inlet flow such that the distortion is redistributed from circumferential to radial variation. These studies show that it is possible to reduce the circumferential distortion to an acceptable level for the engine operation. The *BLI* inlet usually adopts Passive Flow Control (*PFC*), Active Flow Control (*AFC*) or Hybrid Flow Control systems to manipulate the incoming air stream.

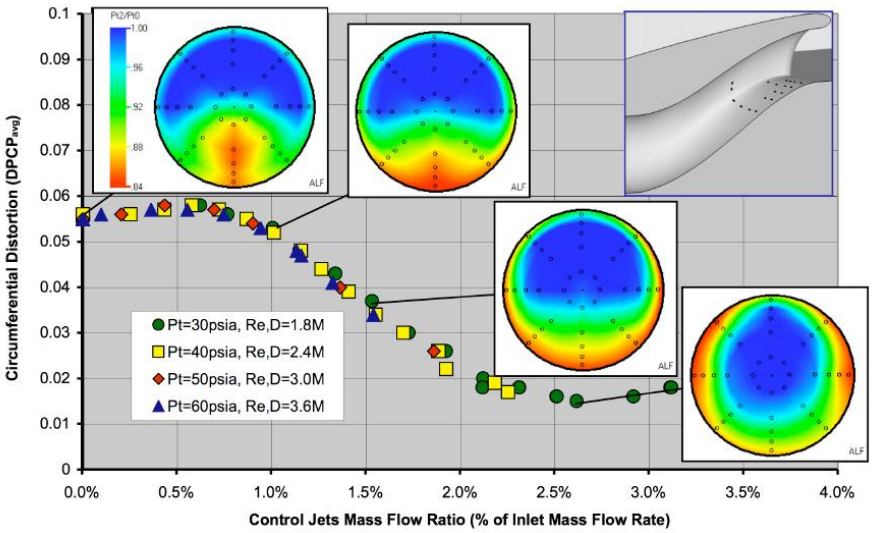

Fig. 2-16. Circumferential distortion ($DPCP_{avg}$) vs the control jet mass flow ratio for the *BLI* inlet utilizing *AFC* [81].

The *PFC* mostly employs vortex generators at the throat of an inlet duct. The wind tunnel test illustrated that the total pressure contour could be reshaped, obtaining around 3% distortion at the fan face [82]. Further research showed that the *PFC* could reduce the *DPCP* to a value low enough for the engine operation to take place at its design point [83]. On the other hand, the research on *AFC* also demonstrated the effectiveness, by impulsively ejecting a small amount of bleeding air at the inlet [84], as shown in Fig. 2-16. It is noted that the flow manipulation of

PFC depends on the incoming flow velocity. The *PFC* only functions well at its design point, while the *AFC* can operate at any work condition at the cost of extra energy-consuming. Therefore the Hybrid Flow Control is considered, which tends to be effective in restraining the inlet distortion at various flight conditions [81]. Similarly, research showed that *BLI* inlet which combines the fence typed *PFC* and *AFC* is capable of limiting the circumferential distortion at the desired Mach number [85].

2.5.2 Noise emission issues

For aircraft using *BLI*, the *BLI* might positively or negatively affect aircraft noise emission, depending on the problem of noise sources and noise propagation [86]. Engines are the major source of noise emission. In the programs of *BWB* aircraft and Silent aircraft, engines were mounted on the top aft part of the center body. The noise propagation from the engine can be effectively shielded by the body, reducing the noise footprint over the ground. On the other side, their embedded *BLI* propulsion system offered an opportunity to deploy acoustic liners. In the design of Silent aircraft, extensive acoustic liners placed inside nacelles and over its internal structure, absorbing broadband turbomachinery noise that accounts for a large portion of total noise emission. The design of Silent aircraft could meet the target of 62 dB in overall noise level during take-off [86].

Besides the noise from engines, another noise source is related to distortion issues. The interaction between the propulsor and the distorted inflow generates low-frequency noise whose frequency is related to the rotational speed of engines [87, 88]. This noise is usually difficult to dissipate. Similar problems can be found in many aircraft using pusher propellers. Pusher propellers normally cause higher noise level over tractor propellers, due to their non-uniform inflow. Such additional noise level is around 15dB [89]. For Silent aircraft, its *BLI* inlets were designed to reduce circumferential total pressure distortion. Further research identified that the *BLI* inlets still generated co-swirl and counter-swirl stream, and this pair of swirl interacting with fans would lead to an increase of 38dB in noise [87].

2.5.3 Losses in the inlet

The *BLI* and *WI* tend to reduce the power consumption of the aircraft using propulsors (propeller or fan), as discussed in section 2.3.2 and section 2.4.1. However, BLI and WI might not be beneficial to the gas turbine (or a pure jet engine). In the preliminary analysis of N3X *HWB* aircraft [90], the benefit for the electric fan was shown to increase as more boundary layer flow was ingested. In contrast, the net benefit for a turbojet engine is neutral or negative, depending on the total temperature ratio of the engine, as shown in Fig. 2-17. The analysis showed that the benefit of *BLI* becomes negative when the total temperature ratio exceeds 2.

In the gas turbine community, it is widely known that the loss at the inlet duct will reduce the level of total pressure hence decreasing the fuel efficiency of the gas turbine [16]. *BLI* and *WI* play similar roles as the inlet duct to reduce the total pressure level at the inlet of the gas turbine. The boundary layer flow (or wake flow)

has a lower level of total pressure than the freestream flow. As a result, *BLI* and *WI* lead to a decrease in the total pressure recovery of an engine. For the engines using the Brayton cycle, such as the gas generator or the turbojet, the total pressure recovery at inlet can significantly change the engine performance: a small reduction in total pressure at inlet normally determines a notable degradation in thermal efficiency.

Due to this negative impact, the jet engine and the gas generator should avoid using *BLI*. In the N3X aircraft concept, a hybrid propulsion system is introduced. Electric fans as the main propulsors are placed at the aft body to utilize *BLI*, but turboshaft engines which generate electric power are installed at the wing tip to ingest the free stream airflow [36].

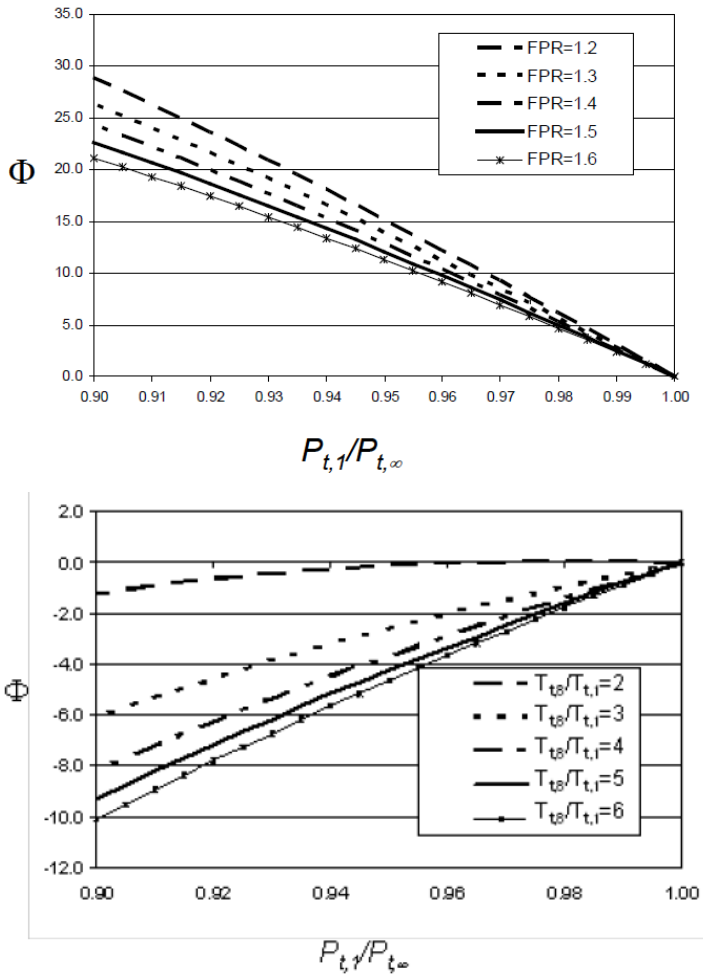

Fig. 2-17. Amount of *BLI* ($P_{t,1}/P_{t,\infty}$) vs the non-dimensional thrust benefit in percentage Φ for the fan (top) and the turbojet engine (bottom), showing that *BLI* is beneficial to the fan, but harmful to the turbojet engine [90].

2.5.4 Other installation issues

Ground clearance is a typical installation issue for an aircraft driven by pusher propellers. The same problem might occur to an aircraft using *BLI*. This aircraft requires its aft-mounted propulsor to be kept away from the ground. Fins, stabilizers or engine nacelles are usually employed for physical protection and the ground clearance issue becomes critical. This issue of aft-mounted propulsor tends to limit the angle of attack during takeoff and landing.

Accessibility to engines is another issue associated with *BLI*. In a conventional aircraft configuration, the engines are mounted on the wing, enabling easy access for maintenance. This is an important feature for airlines. In contrast, a rear-mounted engine installation might cause difficulties, especially for the design with engines embedded inside the aircraft.

Chapter 3 A theoretical analysis of boundary layer ingestion and wake ingestion

This Chapter presents conceptual studies to evaluate the performance of the propulsor and its associated vehicle in the configurations of Wake Ingestion (*WI*) and Boundary Layer Ingestion (*BLI*). A power conversion analysis uses the so-called Power Balance Method (*PBM*) to elaborate the power saving mechanism of *WI*, showing that the Froude's propulsive efficiency as a figure of merit should be separated from the power conversion efficiency in these configurations. The body/propulsor interaction occurring in the *BLI* configuration is qualitatively analyzed to clarify its influence on the performance of the integrated vehicle. The results suggest that the minimization of power consumption should be used as a design criterion for aircraft utilizing *BLI.* This is different from the usual way of aircraft design which mainly focuses on minimizing the airframe drag.

3.1 Introduction

As introduced in Chapter 1, ambitious goals such as *NASA* N+3 and *ACARE* Flightpath 2050 targets were set in terms of reduction of fuel consumption and emissions for future aircraft. To meet these objectives, alternative aircraft configurations have been investigated, some of which aim to integrate the airframe with the propulsive system in a closely coupled manner in which the propulsion system partly ingests the airframe boundary layer. Preliminary studies concerning these new approaches show that this unique integration methodology might result in increased fuel efficiency [68]. This is radically different from many propulsion integration effects which lead to the performance degradation for the conventional tube-wing aircraft configuration [91].

The main promising characteristic of the integration possibilities is that the ingestion of the incoming wake or airframe boundary-layer flow might lead to a reduction in power consumption of about 20% [69]. In the "Silent Aircraft Initiative", *BLI* was introduced as a means to save fuel consumption of about 3~4% with respect to conventional engine configurations [34]. In the research on the Boeing Blended Wing Body (*BWB*) aircraft, a potential fuel reduction of 5.5~10% was predicted with *BLI* [35, 45]. A system study showed that the 3~5% fuel burn benefit due to *BLI* could be achieved for the *NASA* N+2 aircraft using the ultrahigh-bypass-ratio turbofan engine [92]. More favourable values were expected in the D8 aircraft concept employing *BLI* [93], with the experimental and numerical assessments, respectively, showing 6% and 9% power-saving benefit in the *BLI* configuration [37, 38]. In the more dedicated experiments where the propulsor was placed behind the body of revolution, higher values of around 25%~ 30% were identified in terms of power saving [77, 78]. Besides the power-reducing benefit, another phenomenon found in the *BLI* configuration was the change in the drag of the frontal body. In the research on an airship with *BLI*, it was reported that the pressure distribution over the airship hull had been altered by the presence of the

propeller. The drag of the airship hull could increase by 13~40% [43, 44]. In marine propulsion, this effect is known as "thrust deduction". The increase in drag due to interaction was considered counterproductive and was subtracted in the corrected "hull efficiency" [49, 69].

In the present study, two configurations are investigated in which the integration effects are supposed to lead to an increase in performance of the overall system: Wake Ingestion (*WI*) and Boundary Layer Ingestion (*BLI*), as schematically shown in Fig. 3-1. In both configurations, the propulsor is placed behind the body (fuselage). The main difference between the two systems is that the separation distance between the propulsor and the body is determined by the recovery of the freestream static pressure. For an isolated propulsor ingesting wake (top left) or for the *WI* integrated vehicle (top right), it is assumed that the static pressure of the incoming stream has recovered to the atmospheric value p_∞. For an integrated vehicle employing *BLI* (bottom), the pressure of the incoming flow for the propulsor is different from p_∞ due to the presence of the upstream body. The assumption made for *WI* requires the propulsor to be placed far away from the body. Although the assumption is not practical for an actual application, this assumption and the two configurations will help us to analyze different effects in this theoretical study.

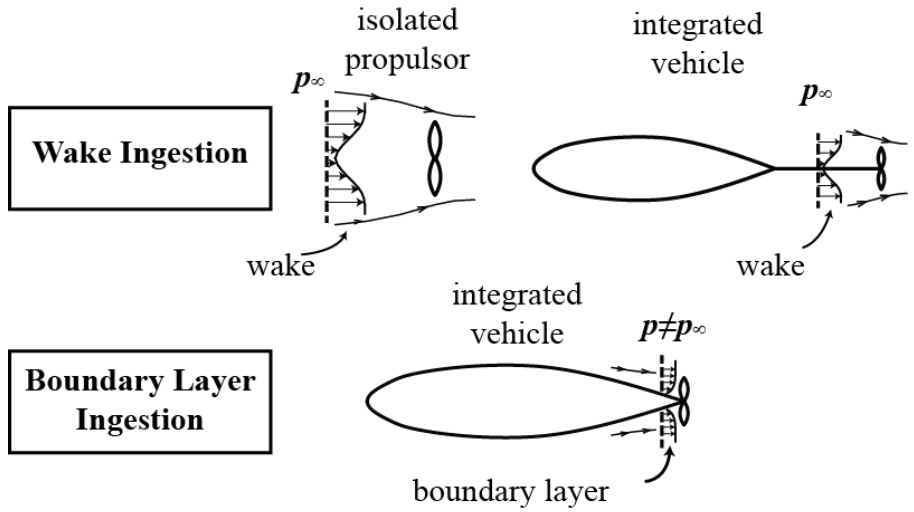

Fig. 3-1. Schematic view of the *WI* and *BLI* configurations for aircraft design.

Despite the abundance of previous studies on *BLI*, there are aspects remained controversial in the aircraft design community, especially concerning the definition of the propulsive efficiency. Smith [69] acknowledged that the Froude "propulsive efficiency" can exceed unity, and he used the term "propulsive coefficient" when dealing with wake ingestion. In order to avoid misunderstanding, this thesis replaces the name of Froude propulsive efficiency as "Froude power coefficient" or "power coefficient". A typical example can be found in the experiment of the 1960s where a 1/20 airship model with a stern-mounted wake ingesting propeller was tested at the *NASA* Langley Research Center's wind-tunnel [43]. Compared to a power coefficient of 0.73 for the propeller ingesting undisturbed free-stream, a maximum

value of 1.22 was reported for the *BLI* configuration. After correcting for the increase in hull drag, a value of 1.03 was obtained. Similar results were obtained during the research on some other airships with stern-mounted propellers [44]. It is noted that the "efficiency" is based on V_∞. To correct the misrepresented "efficiency", the velocity V_b of the wake flow to the propeller was considered. In the wind tunnel test, it was observed that for the equal shaft power, the thrust produced by the propeller when ingesting the boundary layer was significantly higher than the thrust produced when operating in the freestream condition. McLemore [43] points out that "the efficiency of the propeller based on the velocity of the flow in which it is actually operating is well below 1.0". Nevertheless, the use of a reduced velocity V_b ($V_b<V_\infty$) referring to the incoming wake flow triggered some confusion, especially when dealing with the power in the form TV_b. As observed from a stationary frame of reference, the airship hull, as well as the propeller was supposed to move forward at the speed of V_∞, but the thrust T was produced at the lower velocity V_b.

To address the "efficiency paradox" from different perspectives, other studies have analyzed the contribution of the wake flow. As explained by Betz [73], the kinetic energy contained in the flow of the upstream body wake should be accounted for when computing propeller performance. Duncan et al. [49] pointed out that possible benefits could be determined by the reduction of the kinetic energy wasted in the slipstream after the propulsor due to the presence of "a forward moving wake current" (referring to the stationary frame of reference). Drela [33] introduced the power balance method (*PBM*) as a means to demonstrate that *BLI* reduces the viscous dissipation of the aircraft wake and the propulsive jet. Arntz, et al. [47] worked on the exergy-based approach, taking into account the heat transfer in the analysis of *BLI* [48].

Building upon this research line, the current study deals with the power conversion processes of integrated *WI* and *BLI* systems, with two main objectives. First, an analysis is proposed to separate the concept of propulsive efficiency from the one of a Froude power coefficient with respect to the effective power conversion. Second, an attempt is made to evaluate the effective power consumption for an aircraft configuration using *WI* or *BLI*. Drela's *PBM* [33] is used to derive the power input and output terms for an isolated propulsor as well as for an integrated vehicle. Therefore, a brief introduction to the theoretical aspects of *PBM* and wake systems is provided in Sec. 3.2. The fundamental characteristics of *WI* design are presented in Sect. 3.3, together with the clarification of Froude power coefficient in the *WI* case. In Sec. 3.4, the characteristics of the body/propulsor interaction are discussed for the *BLI* configuration, focusing on the influence of the body profile drag. Section 3.5 concludes the investigation with the major points of interest in the present study.

3.2 Power balance method and wake system

The wake system (body wake and jet wake) is the key to the analysis of *WI* and *BLI*. The power conversion associated with the wake system is analyzed by using the *PBM* proposed by Drela [33, 46]. The *PBM* employs an integral form of the

kinetic energy equation for a defined control volume (*CV*) encompassing the aircraft. This technique can be used to estimate both power sources and sinks in the flowfield, along with the energy deposition rates as the vital power terms to close the power balance equation. In the *PBM*, the deposition rates are accessed at the so-called Trefftz planes (*TP*s), which normally refers to the outlet plane of a *CV*. For clarity, in this study, a survey plane (*SP*) is defined as the inlet plane or as an internal interface of a *CV*, and a *SP* functions the same as the *TP* to assess the surface integrals of energy deposition rates ($K\dot{E}_w$ and $\dot{E}_p$). The kinetic energy deposition rate $K\dot{E}_w$ contains the axial component $\dot{E}_a$ and the transverse component $\dot{E}_v$. $K\dot{E}_w$ corresponds to the kinetic energy of the wake flow (or boundary-layer flow) crossing a chosen *TP*, as in Eqn. (3.0). It is noted that the integrand of $K\dot{E}_w$, ($\frac{1}{2}(u-V_\infty)^2+\frac{1}{2}(v^2+w^2)$), is based on the relative velocity to V_∞, hence it is positive for both the body wake flow ($u_b < V_\infty$) and the jet wake ($u_j > V_\infty$) which are dominated by $\dot{E}_a$.

$$K\dot{E}_w = \dot{E}_a + \dot{E}_v = \iint_{TP} \rho u \cdot \tfrac{1}{2}(u-V_\infty)^2 dS + \iint_{TP} \rho u \cdot \tfrac{1}{2}(v^2+w^2) dS \tag{3.0}$$

Another energy deposition rate is defined as the pressure-work deposition rate $\dot{E}_p$. This term denotes the pressure energy of the wake flow through a corresponding *TP*. The value of $\dot{E}_p$ depends on the relative velocity to V_∞ and the absolute pressure (p-p_∞), as given in Eqn. (3.1). It is noted that $\dot{E}_p$ can be excluded in the *WI* discussion when the pressure at *TP*s is equal to p_∞, but it should be taken into account in the case of *BLI*.

$$\dot{E}_p = \iint_{TP} (p-p_\infty)\cdot(u-V_\infty)\, dS \tag{3.1}$$

The power sink in the wake system is the viscous loss dominated by the viscous dissipation rate Φ. This power sink applies to the volume integral over the *CV* between an inlet and a specified *TP*. The integrand of viscous dissipation rate Φ in three dimensions contains nine terms. For incompressible flows that exclude bulk viscous stress, the integrand is simplified as in Eqn. (3.2). In the expression, the shear viscous stress consists of the laminar and Reynolds stresses. The integrand is nonzero and positive in the viscous region of the flowfield where velocity a gradient exists, as depicted in the shaded regions of Fig. 3-2.

$$\Phi \cong \iiint_{CV} \left[\left(\mu\frac{\partial u}{\partial y} - \rho u'v'\right)\frac{\partial u}{\partial y} + \left(\mu\frac{\partial w}{\partial y} - \rho v'w'\right)\frac{\partial w}{\partial y}\right] dV \tag{3.2}$$

According to the *PBM*, the major terms are combined in a power balance equation [Eqn. (3.3)]:

$$K\dot{E}_w + \dot{E}_p + \Phi = const \tag{3.3}$$

By placing different *TP*s downstream the wake, it is possible to track the power conversion along the streamwise direction. The $\dot{E}_p$ is isentropically converted into $K\dot{E}_w$ when the pressure is stabilizing towards p_∞, while Φ irreversibly increases in

the streamwise direction. As a result, the $K\dot{E}_w$ gradually decreases and is eventually dissipated in the infinite far field, as illustrated in Fig. 3-2. For a chosen *TP*, the sum of the power is constant [Eqn. (3.3)]. This approach can be extended to both body wake and jet wake, as shown in Fig. 3-2. The total wake energy flow rate is simply the power assessed at the inlet plane SP_1.

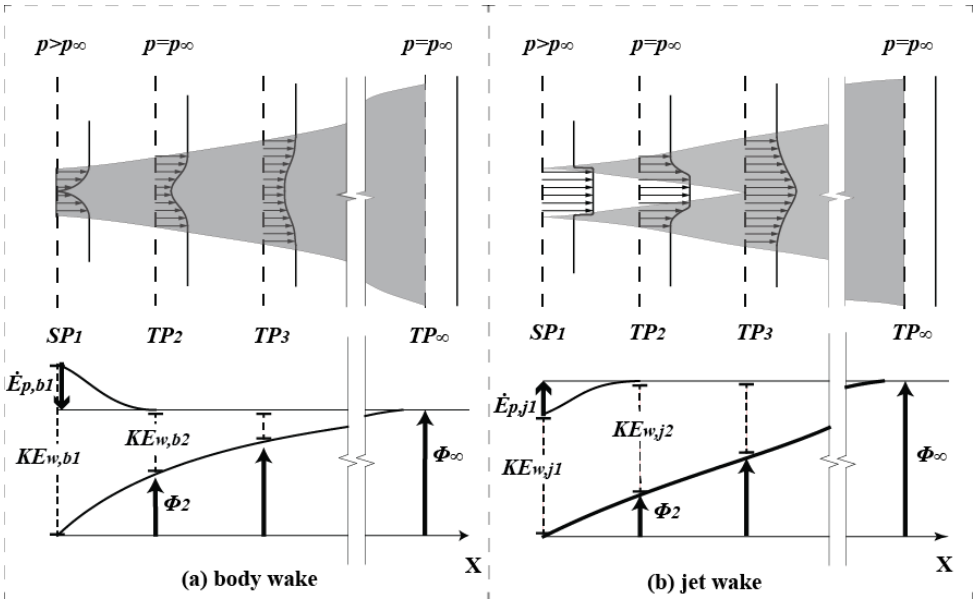

Fig. 3-2. Power balance of the body wake (a) and jet wake (b) at different planes in the streamwise direction.

3.3 The impact of *WI* on power consumption

3.3.1 Power balance for a general wake ingestion actuator disc

The physics of reducing the power consumption of a *WI* actuator disc is discussed in this section. Firstly two special cases are reviewed by using *PBM*, namely a free-stream actuator disc and an ideal wake-filling actuator disc. Then, a more general case of a *WI* actuator is investigated.

i. Froude power coefficient for a free stream actuator disc

A freestream actuator disc is obtained as the classical Froude actuator disc model by providing a uniform incoming free-stream flow of V_∞. A *CV* is built to encompass the fluid around the actuator disc with inner and external boundaries, as shown in Fig. 3-3. The external boundary consists of an inlet, an outlet plane, and a stream tube. They are chosen sufficiently far away from the actuator disc such that the pressure at the external boundary is equal to p_∞. Furthermore, the viscous dissipation referred to the actuator disc (the dissipation over the blade surface, the jet dissipation inside the *CV*, etc.) is neglected within the *CV*. The outlet aligns with a

TP (as shown in Fig. 3-3 by a thick dashed line) where the jet wake is described with a velocity profile $u_j(y)$.

The *KE* production rate represents the power input from the actuator disc, and it is expressed as the time rate of change of *KE* between the inlet and the outlet *TP* in Eqn. (3.4):

$$\dot{KE}_{p,free} = \iint_{TP} \rho u_j \tfrac{1}{2}\left(u_j^2 - V_\infty^2\right) dS \tag{3.4}$$

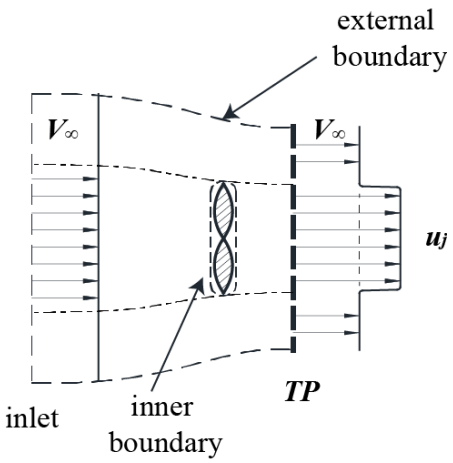

Fig. 3-3. Control volume for the free-stream actuator disc.

The thrust *T* generated by the actuator disc can be obtained from the momentum equation; hence, a thrust power TV_∞ as a power output can be expressed as in Eqn. (3.5). Another power output term is the jet wake *KE* outflow crossing the *TP* in Eqn. (3.6). Because the original actuator disc model is dominated by axial flow, the transverse component $\dot{E}_v$ can be ignored. As discussed in the wake system, $\dot{KE}_{wJ}$ leaves the current *CV* and is eventually dissipated at infinity in the far field.

$$TV_\infty = \iint_{TP} \rho u_j \left(u_j - V_\infty\right) V_\infty dS \tag{3.5}$$

$$\dot{KE}_{w,J} = \dot{E}_a = \iint_{TP} \rho u_j \tfrac{1}{2}\left(u_j - V_\infty\right)^2 dS \tag{3.6}$$

The power balance (3.7) for the free-stream actuator disc can be obtained by subtracting the output terms [Eqn. (3.5) and (3.6)] from the power input [Eqn. (3.4)]. The Froude power coefficient (efficiency) presents the efficiency of the power conversion [Eqn. (3.8)]. It can be noted that, due to the presence of TV_∞ in both numerator and denominator (3.8), the value is bounded between zero and one:

$$\dot{KE}_{p,free} = TV_\infty + \dot{KE}_{w,J} \tag{3.7}$$

$$\eta_{p,free} = \frac{TV_\infty}{\dot{KE}_{p,free}} = \frac{TV_\infty}{TV_\infty + \dot{KE}_{w,J}} < 1 \tag{3.8}$$

If the velocity profile at the *TP* is uniform, the velocity of the jet wake is simply u_j. The Froude power coefficient can be correlated to the upstream and downstream velocity ratios when the cross-sectional area S_j of the jet wake is taken into account. By substituting the uniform velocity profile ($u_j > V_\infty$) in Eqn. (3.8), a simplified form can be derived [Eqn. (3.8)], still bounded between zero and one:

$$\eta_{p,free} = \frac{TV_\infty}{\dot{KE}_{p,free}} = \frac{\iint_{TP} \rho u_j V_\infty (u_j - V_\infty) dS}{\iint_{TP} \rho u_j \frac{1}{2}\left(u_j^2 - V_\infty^2\right) dS} = \frac{\rho u_j (u_j - V_\infty) V_\infty S_j}{\rho u_j \frac{1}{2}\left(u_j^2 - V_\infty^2\right) S_j} = \frac{2}{1+\frac{u_j}{V_\infty}} \tag{3.8}$$

The preceding analysis shows that the power balance equation for a freestream actuator complies with the classical actuator disc model. It additionally allows us to write the expression for the power loss of the jet wake. In this respect, the Froude power coefficient for the freestream actuator can be used as a power conversion efficiency. Its numerator corresponds to the useful output of thrust power, whereas the denominator is the power input given by the actuator disc.

ii. Froude power coefficient for an ideal wake filling actuator disc

An ideal wake-filling actuator disc model was discussed by Betz [73]. It reenergizes the inflow in such a way that the body wake was ideally filled back to the freestream condition, as illustrated in Fig. 3-4. A similar *CV* is drawn with the pressure at the external boundary identical to p_∞. A *SP* is aligned with the inlet plane of the *CV*, where an inflow is given by the velocity profile of a body wake $u_b(y)$.

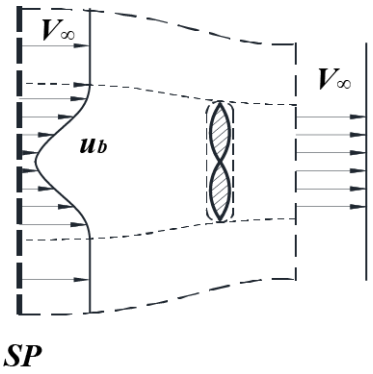

Fig. 3-4. Control volume of an ideal wake filling actuator disc.

In this special case, the power sources are constituted by two terms: the first one is the body wake *KE* crossing the *SP* [Eqn. (3.9)]; this term ($\dot{KE}_{w,b}$) is simplified only to consist of the axial component of *KE* deposition. It enters the *CV* along with the inflow and is considered as an input power. The second input term is $\dot{KE}_{p,ideal}$, the *KE* production rate provided by the ideal wake filling actuator disc [Eqn. (3.10)]. It should be clear that $V_\infty > u_b$, and $\dot{KE}_{p,ideal}$ is positive.

$$\dot{KE}_{w,b} = \dot{E}_a = \iint_{SP} \rho u_b \frac{1}{2}(u_b - V_\infty)^2 \, dS \tag{3.9}$$

$$\dot{KE}_{p,ideal} = \iint_{SP} \rho u_b \tfrac{1}{2}(V_\infty^2 - u_b^2) dS \tag{3.10}$$

The momentum equation quantifies the thrust T as a force needed to cause a change in the momentum. However, it should be noted that the actual thrust is not generated from the momentum excess (with respect to undisturbed freestream state) but from the refilled momentum defect into the momentum neutral of the freestream condition. As a result, the TV_∞ is given by Eqn. (3.11), as a power output of this *CV*.

$$TV_\infty = \iint_{SP} \rho u_b (V_\infty - u_b) V_\infty dS \tag{3.11}$$

For this ideal wake-filling actuator, the combination of Eqns.(3.9), (3.10) and (3.11) obtains the power balance in Eqn. (3.12).

$$\dot{KE}_{w,b} + \dot{KE}_{p,ideal} = TV_\infty \tag{3.12}$$

The equation (3.12) states that the inflow body wake and the actuator disc essentially contribute together to generate TV_∞. In this respect, the Froude power coefficient exceeds unity Eqn. (3.13). The form of power coefficient does not respond to the actual power conversion of this actuator disc because the power source of $KW_{w,b}$ is excluded.

$$\eta_{p,ideal} = \frac{TV_\infty}{\dot{KE}_{p,ideal}} = \frac{\dot{KE}_{w,b} + \dot{KE}_{p,ideal}}{\dot{KE}_{p,ideal}} > 1 \tag{3.13}$$

iii. The general WI actuator disc

A general *WI* actuator disc can be considered as a combination of the aforementioned two special cases, namely the freestream and the ideal wake-filling actuator disc. The classical actuator disc is extended to a more general form to account for the nonuniform inflow, as shown in Fig. 3-5. A *CV* is chosen around the actuator delimited by the external and internal boundaries, as shown in Fig. 3-5. The external boundary is sufficiently far from the actuator disc to assume the pressure is p_∞, and the viscous dissipation inside the *CV* can be neglected.

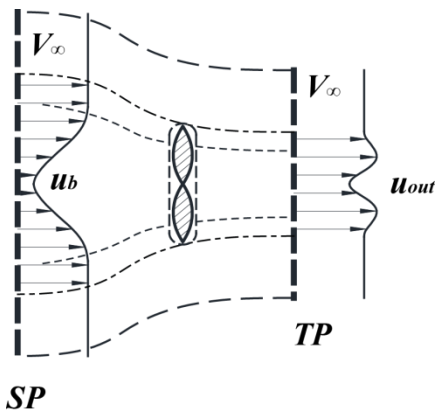

Fig. 3-5. Control volume for a *WI* actuator disc.

In the present *CV*, the inlet coincides with the *SP*. In this plane, the incoming stream possesses a body wake determined by a velocity profile $u_b(y)$. Downstream the actuator, the wake flow leaves the *CV* through the outlet *TP* plane where the flow velocity profile is $u_{out}(y)$. For the *CV*, the two equations [Eqns.(3.14)(3.15)] represent the conservations of mass and momentum. The latter equation assesses the thrust *T* generated by the actuator disc.

$$\iint_{SP} \rho u_b dS - \iint_{TP} \rho u_{out} dS = 0 \tag{3.14}$$

$$T = \iint_{TP} \rho u_{out}^2 dS - \iint_{SP} \rho u_b^2 dS \tag{3.15}$$

Power inputs and outputs are retrieved from the power balance analysis. The inputs are constituted by two terms: the first one is the body wake *KE* inflow through the *SP* entering the *CV* [Eqn. (3.16)]. Note that, when observing from the stationary frame of reference, the actuator disc moves forward at V_∞ and the body wake flux is moving in the forward direction.[When observing at the fixed spatial location, the forward motion of the body wake current is unsteady. But, at the *SP* (moving forward at V_∞) the spatial location of which is unfixed, the probed velocity vector of wake current is independent of time, and is in the forward direction.] The actuator disc gains from the advancing the motion of the fluid; hence, $\dot{KE}_{w,b}$ (more specifically, its axial component $\dot{E}_a$) is considered as an input power. The second power input term is the *KE* production rate given by the actuator disc. In this case, the *KE* production rate is expressed as the increment of fluid *KE* from the *SP* to the *TP* in Eqn. (3.17). The total power input of the *CV* is the sum of two terms, shown in Eqn. (3.18).

$$\dot{KE}_{w,b} = \iint_{SP} \rho u_b \tfrac{1}{2}(u_b - V_\infty)^2 \, dS \tag{3.16}$$

$$\dot{KE}_{p,WI} = \iint_{TP} \rho u_{out} \tfrac{1}{2} u_{out}^2 dS - \iint_{SP} \rho u_b \tfrac{1}{2} u_b^2 dS \tag{3.17}$$

$$\dot{E}_{input} = \dot{KE}_{w,b} + \dot{KE}_{p,WI} = \iint_{SP} \rho u_b \tfrac{1}{2} V_\infty^2 dS - \iint_{SP} \rho u_b^2 V_\infty dS + \iint_{TP} \rho u_{out} \tfrac{1}{2} u_{out}^2 dS \tag{3.18}$$

The power outputs are also constituted by two terms: the first one is TV_∞ as a useful output [Eqn. (3.19)]. The second term is the wake *KE* of the downstream wake outflow leaving this *CV* through the *TP*, as in Eqn. (3.20). The profile of wake outflow $u_{out}(y)$ can be linearized and separated in two contributions: a body wake ($u_b < V_\infty$) and a jet wake ($u_j > V_\infty$). Outside the *CV*, the $\dot{KE}_{w,out}$ of the downstream wake will be eventually dissipated in the far field, as elaborated in the wake system. The total power output of the *CV* is given by Eqn. (3.21):

$$TV_\infty = \iint_{TP} \rho u_{out}^2 V_\infty dS - \iint_{SP} \rho u_b^2 V_\infty dS \tag{3.19}$$

$$\dot{KE}_{w,out} = \dot{E}_{a,out} = \iint_{TP} \rho u_{out} \tfrac{1}{2}(u_{out} - V_\infty)^2 \, dS \tag{3.20}$$

$$\dot{E}_{output} = TV_\infty + \dot{KE}_{w,out} = \iint_{TP} \rho u_{out} \tfrac{1}{2} V_\infty^2 dS + \iint_{TP} \rho u_{out} \tfrac{1}{2} u_{out}^2 dS - \iint_{SP} \rho u_b^2 V_\infty dS \tag{3.21}$$

The balance between total power inputs and outputs can be carried out by subtracting Eqn. (3.21) from Eqn. (3.18). In this respect, by including the continuity [Eqn. (3.14)], the power balance [Eqn. (3.22)] for the general *WI* actuator disc can be written as in Eqn. (3.23):

$$\dot{E}_{input} - \dot{E}_{output} = \tfrac{1}{2} V_\infty^2 \left(\iint_{SP} \rho u_b dS - \iint_{TP} \rho u_{out} dS \right) = 0 \tag{3.22}$$

$$\dot{KE}_{w,b} + \dot{KE}_{p,WI} = TV_\infty + \dot{KE}_{w,out} \tag{3.23}$$

From Eqn. (3.23), TV_∞ can be expressed as described in Eqn. (3.24), which is further substituted into the expression of Froude power coefficient. As a result, the expression for the general *WI* actuator disc is given in Eqn. (3.25). From this equation, the critical condition for power coefficients larger than one can be found: $\dot{KE}_{w,\mathrm{b}} > \dot{KE}_{w,\mathrm{out}}$. This condition shall be satisfied in the aforementioned examples where power coefficients exceed unity.

$$TV_\infty = \dot{KE}_{p,WI} + \dot{KE}_{w,b} - \dot{KE}_{w,out} \tag{3.24}$$

$$\eta_{p,WI} = \frac{TV_\infty}{\dot{KE}_{p,WI}} = \frac{\dot{KE}_{p,WI} + \dot{KE}_{w,b} - \dot{KE}_{w,out}}{\dot{KE}_{p,WI}} = 1 + \frac{\dot{KE}_{w,b} - \dot{KE}_{w,out}}{\dot{KE}_{p,WI}} \tag{3.25}$$

A clear explanation for the power-saving mechanism of the *WI* actuator disc can be identified through Eqn. (3.23). To generate a certain amount of TV_∞ for propulsion, the actuator disc uses the body wake *KE* flow as a power input. Moreover, due to the momentum defect of the ingested body wake, the same thrust can be produced with less momentum excess (u_{out}-V_∞) in the downstream wake, resulting in the lower wake *KE* flow of the downstream wake. Consequently, the power $\dot{KE}_{p,WI}$ given by the actuator disc is substantially reduced for the desired TV_∞.

In summary, the *WI* actuator disc benefits from using the body wake *KE* inflow and also from reducing the downstream wake *KE* outflow. The best performance for this actuator disc can be obtained when capturing the largest contribution of the body wake while minimizing the downstream wake.

3.3.2 Power conservation for a *WI* integrated vehicle

In the preceding discussion on the *WI* actuator disc, $\dot{KE}_{w,\mathrm{b}}$ is considered as a power source (3.23). To present a complete picture, $\dot{KE}_{w,\mathrm{b}}$ is further discussed in two cases, namely, the isolated body and the integrated vehicle which combines the body with the actuator. Moreover, the correlation between the drag force and the power consumption is examined, highlighting the impact of *WI* on the body drag and its influence on the power consumption.

i. Power balance for an isolated body and an ideal WI integrated vehicle

Drela [33] demonstrated the power balance for an isolated two-dimensional (2-D) airfoil and concluded that the total dissipated power in the flowfield was simply equal to the so-called drag power DV_∞. This power balance can be applied to an isolated body with the assumption of zero-lift and nonzero profile drag, as shown in Fig. 3-6. A *TP* coincides with the outlet of the *CV* (the thick, dashed line), where pressure was equal to p_∞ and a non-uniform velocity profile $u_b(y)$ of body wake was observed. For the prescribed *CV*, the body drag *D* was obtained as in Eqn. (3.26). The power balance can be expressed by Eqn. (3.27) [33], in which DV_∞ is considered as the power input to sustain the body against the incoming flow with speed V_∞:

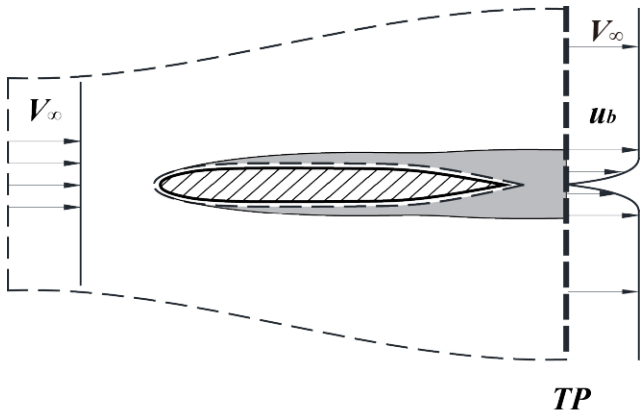

Fig. 3-6. Control volume for the isolated body showing the boundary layer and wake area leading to a velocity defect.

$$D = \iint_{TP} \rho u_b (V_\infty - u_b) dS \tag{3.26}$$

Drag power: $$DV_\infty = \Phi_{BL} + \dot{KE}_{w,b} \tag{3.27}$$

Viscous dissipation: $$\Phi_{BL} \cong \dot{KE}_{loss} = \iint_{TP} \rho u_b \tfrac{1}{2}(V_\infty^2 - u_b^2) dS \tag{3.28}$$

The total power loss consists of two power terms. The first term is viscous dissipation, mainly in the boundary layer (shaded region in Fig. 3-6). It can also be expressed as the kinetic energy loss rate of the *CV* [Eqn. (3.28)]. The second term is the wake *KE* outflow leaving the *CV*. The $\dot{KE}_{w,b}$ is given by the same expression of Eqn. (3.16). From the power balance [Eqn. (3.27)], it can be concluded that $\dot{KE}_{w,b}$ is a product of the DV_∞ from this isolated body.

An ideal *WI* integrated vehicle combines the isolated body with an ideal wake-filling actuator disc. The two elements are supposed to be at a nonintrusive distance (large enough so that their respective pressure fields are not interacting with each other) such that the mutual impact on each other can be ignored. A new *CV* combines the two previously described individual *CVs*, as shown in Fig. 3-7. The

outlet of the left part coincides with the inlet of the right part, obtaining an intermediate *SP* interface (pressure is p_∞). In accordance with the previous assumptions, it is assumed that the viscous dissipation is finite for the body in the left part but neglected for the actuator disc in the right part.

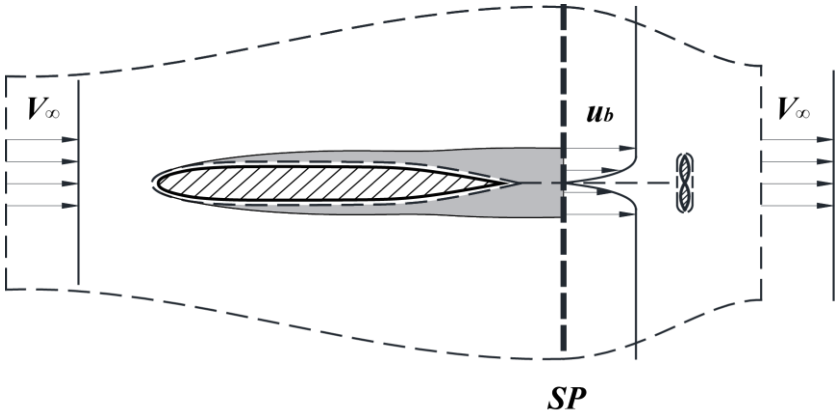

Fig. 3-7. Control volume for the ideal *WI* integrated vehicle.

Since no wake flow is entering or leaving the *CV*, the only power loss term is the viscous dissipation within the left part, which is the same as in Eqn. (3.28). The input term is the *KE* production rate in the right part, the same as in Eqn. (3.10). The identical expressions of Eqn. (3.28) and Eqn. (3.10) indicate the power balance in this case: the power input from the ideal wake-filling actuator disc simply balances the boundary layer (*BL*) dissipation of the body [Eqn. (3.29)]:

$$\dot{KE}_{p,ideal} = \dot{KE}_{loss} \cong \Phi_{BL} \tag{3.29}$$

The actuator disc refills the body wake into freestream condition; thus, the net force of the vehicle is zero, entailing that the actuator thrust *T* balances the body drag *D*. Both forces indeed exist, but it is noted that it is true only under the assumption that the pressure fields of two elements do not interact, and the forces can be quantified from the momentum equation: in the left part of the CV, *D* equals the momentum loss from inlet to the *SP*, which is the same as in the isolated case. In the right part of the *CV*, *T* is expressed as the momentum increase from the *SP* to the outlet plane [Eqn. (3.30)]:

$$T = D = \iint_{SP} \rho u_b (V_\infty - u_b) dS \tag{3.30}$$

By keeping the same trust power TV_∞ in Eqn. (3.12), the power coefficient gives a value larger than one [Eqn. (3.31)]. Since TV_∞ equals DV_∞ in Eqn. (3.27), the power coefficient can also be expressed in Eqn. (3.32). It is clear from both derivations that the power of $\dot{KE}_{w,b}$ is responsible for a power coefficient greater than one:

$$\eta_{p,ideal} = \frac{TV_\infty}{\dot{KE}_{p,ideal}} = \frac{\dot{KE}_{w,b} + \dot{KE}_{p,ideal}}{\dot{KE}_{p,ideal}} > 1 \tag{3.31}$$

$$\eta_{p,ideal} = \frac{TV_\infty}{\dot{KE}_{p,ideal}} = \frac{DV_\infty}{\Phi_{BL}} = \frac{\Phi_{BL} + \dot{KE}_{w,b}}{\Phi_{BL}} > 1 \tag{3.32}$$

The body wake is generated by the body and is immediately captured by the wake-filling actuator disc. It is an intermediate product within the *CV*, which is only observed between the two elements. Therefore, $\dot{KE}_{w,b}$ is a transient power term in the *CV*, and it can be indeed measured at the *SP*. It should be noted that the power conservation is indeed satisfied [Eqn. (3.29)]. This indicates that Froude power coefficient does not correspond to the effective power conversion efficiency in the *WI* integrated vehicle. The numerator contains a transient power of $\dot{KE}_{w,b}$, yielding a power coefficient larger than one, as observed in the previous section. When the virtual power conversion [Eqn. (3.29)] is considered, the actual power efficiency can be demonstrated to be one (3.33):

$$\eta_{real} = \frac{\Phi_{BL}}{\dot{KE}_{p,ideal}} = 1 \tag{3.33}$$

ii. Power balance for a general WI integrated vehicle

The more general case for a *WI* integrated vehicle can be obtained by combining the isolated body with the general *WI* actuator disc. A new united *CV* is shown in Fig. 3-8. A *SP* is an internal interface, and a *TP* coincides with the *CV*'s outlet plane where the outflow is described by a non-uniform velocity profile $u_{out}(y)$. The same assumption of p_∞ at the *SP* and the *TP* is maintained, and the dissipation within the right part of the *CV* pertaining to the actuator disc is neglected. Provided with the continuity equation [Eqn. (3.14)], the momentum equations [Eqns. (3.26) and (3.15)] for the two elements can be manipulated to obtain the net force *N* of the entire vehicle, as shown in Eqn. (3.34).

When adding the power balance equations [Eqn. (3.23) and Eqn. (3.27)], the power balance for the integrated vehicle can be obtained as in Eqn. (3.35). In the manipulation process, the $\dot{KE}_{w,b}$ at the *SP* is canceled as a transient power. A net force power NV_∞ denotes (TV_∞-DV_∞). In this power balance equation, $\dot{KE}_{p,WI}$ is the power input, whereas rest of the terms on the right are the power output and power sink of the *CV*:

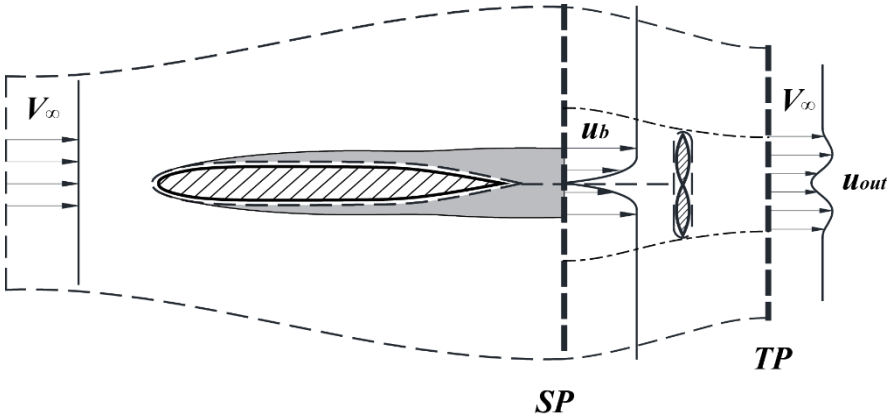

Fig. 3-8. Control volume for the general *WI* integrated vehicle.

$$N = T - D = \iint_{TP} \rho u_{out}(u_{out} - V_\infty) dS \tag{3.34}$$

$$\dot{KE}_{p,WI} = NV_\infty + \Phi_{BL} + \dot{KE}_{w,out} \tag{3.35}$$

When considering the summation of three terms as the "actual power output", the real efficiency can be identified as the power output over the input of $\dot{KE}_{p,WI}$. This real efficiency is 100% and hence not very informative. In practice, it is not convenient to measure viscous dissipation. On the other hand, by taking NV_∞ as the numerator in efficiency, this definition doesn't provide much information either: zero value is obtained at the equilibrium condition (T=D) of the vehicle. Therefore, the conventional expression given by Froude is still used, but the concept of propulsive efficiency is replaced with a power coefficient to avoid confusion. The coefficient can be considered as a parameter correlating the actuator disc thrust T with the power input of actuator disc $\dot{KE}_{p,WI}$, corresponding to a force term in Eqn. (3.34) and a power term in Eqn. (3.35).

iii. The relationship between the drag force and power consumption

In this part, the correlation between force and power is reviewed, highlighting the impacts of *WI* on the body drag D and power consumption. For a given isolated body, a momentum thickness and a kinetic energy thickness are defined by a boundary-layer profile, as shown in Eqn. (3.36) and (3.37), as a function of the Reynolds number. For simplicity, the classical case of a flat plate with a laminar boundary-layer is discussed, such that the solutions from Blasius [94] are used[Eqn. (3.38)]:

$$\theta \equiv \iint_{TP} \frac{u}{V_\infty}\left(1 - \frac{u}{V_\infty}\right) dS \tag{3.36}$$

$$k \equiv \iint_{TP} \frac{u}{V_\infty}\left(1 - \frac{u^2}{V_\infty^2}\right) dS \tag{3.37}$$

$$\theta = 0.664\sqrt{\frac{\nu \cdot x}{V_\infty}}; \quad k = 1.044\sqrt{\frac{\nu \cdot x}{V_\infty}} \tag{3.38}$$

The momentum thickness θ quantifies the profile drag D of the plate in Eqn.(3.39), hence the power of DV_∞ in Eqn.(3.40). These two equations can be combined into one equation by cancelling the variable of V_∞, as in Eqn. (3.40). In this manner, the power DV_∞ follows the form in Eqn. (3.40):

$$D = \rho V_\infty^2 \theta = 0.664\rho(\nu \cdot x)^{\frac{1}{2}} \cdot V_\infty^{\frac{3}{2}} \tag{3.39}$$

$$DV_\infty = \rho V_\infty^3 \theta = 0.664\rho(\nu \cdot x)^{\frac{1}{2}} \cdot V_\infty^{\frac{5}{2}} \tag{3.40}$$

$$DV_\infty = \left[1.314\rho^{-\frac{2}{3}}(\nu \cdot x)^{-\frac{1}{3}}\right] \cdot D^{\frac{5}{3}} \tag{3.40}$$

The kinetic energy thickness k can determine the kinetic energy loss rate or the *BL* dissipation rate of Φ_{BL}, as in Eqn. (3.41). Once we put this equation [Eqn. (3.41)] together with Eqn. (3.39) and combine them into one equation by cancelling V_∞, the power Φ_{BL} and the drag force D are correlated. The expression is given as Eqn. (3.42) :

$$\Phi_{BL} = \dot{KE_{loss}} = \tfrac{1}{2}\rho V_\infty^3 k = 0.522\rho(\nu \cdot x)^{\frac{1}{2}} \cdot V_\infty^{\frac{5}{2}} \tag{3.41}$$

$$\Phi_{BL} = \left[1.033\rho^{-\frac{2}{3}}(\nu \cdot x)^{-\frac{1}{3}}\right] \cdot D^{\frac{5}{3}} \tag{3.42}$$

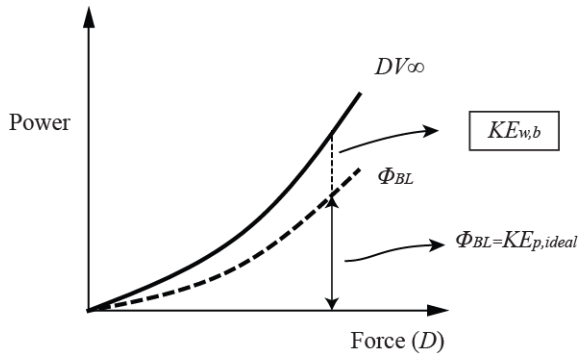

Fig. 3-9. The relationship between body drag and power.

With Eqns. (3.40) and (3.42), a plot can be drawn showing two power terms versus the body drag *D*, as shown in Fig. 3-9 (solid line for DV_∞, and dashed line for Φ_{BL}). The plot illustrates that the power DV_∞ can be decomposed, in accordance with the power balance equation [Eqn. (3.27)]. The $\dot{KE_{w,b}}$ denotes the gap between the two curves in Fig. 3-9. As shown in Eqn. (3.43), $\dot{KE_{w,b}}$ takes about 21% out of the power consumption of DV_∞ in the flat-plate case [33].

$$\frac{\dot{KE}_{w,b}}{DV_\infty} = \frac{DV_\infty - \Phi_{BL}}{DV_\infty} = \frac{\left[1.314\rho^{-\frac{2}{3}}(\nu\cdot x)^{-\frac{1}{3}}\right]\cdot D^{\frac{5}{3}} - \left[1.033\rho^{-\frac{2}{3}}(\nu\cdot x)^{-\frac{1}{3}}\right]\cdot D^{\frac{5}{3}}}{\left[1.314\rho^{-\frac{2}{3}}(\nu\cdot x)^{-\frac{1}{3}}\right]\cdot D^{\frac{5}{3}}} \times 100\% \approx 21\% \qquad (3.43)$$

An integrated vehicle can be obtained by combining the same flat plate with an ideal wake filling actuator disc. Under the assumptions made previously for the ideal *WI* integrated vehicle, the friction drag D of the plate remains unchanged as in Eqn. (3.30), whereas the power consumption is reduced to Φ_{BL} according to Eqn. (3.29). In this ideal WI integrated case, θ and k in Eqn. (3.38) can be substituted into the power coefficient of Eqn. (3.32), obtaining a value of approximately 1.27. It represents the actual power consumption curve Φ_{BL} below the curve of DV_∞ in Fig. 3-9.

In this figure, the power consumption drops along a vertical line for a given condition, illustrating that *WI* reduces the power consumption without reducing the body drag D; hence the relationship between the force and power is not continuous-monotonic. It is noted that *WI* is distinctive from many other technologies applied to the aircraft that coincidentally reduce the drag force and power consumption.

3.4 Integration issues for the *BLI* configuration

In the preceding discussion on *WI*, it is assumed there is no interaction between the pressure fields of the body and actuator elements, and the viscous loss related to the actuator disc is neglected. In the more realistic *BLI* configuration these assumptions are not valid; hence, they are dropped in this section to investigate the impacts on body drag force and power consumption in the *BLI* configuration.

3.4.1 Interaction impact on body profile drag

The propulsor(s) is/are installed at the body tail (or the trailing edge) in the *BLI* configuration. Due to this integration, the propulsor and body elements are immersed in a pressure field, which is not equal to p_∞. This part mainly investigates the influence of *BLI* on the body profile drag. In contrast to the momentum assessment at a *TP*, in the following discussion, the drag D is studied as the aerodynamic force imposed on the body surface, consisting of the pressure and viscous drag components. Since the effect of the body/propulsor interaction highly depends on the characteristics of the body shape and the propulsor, the following analysis is limited to a general qualitative discussion.

i. Impact on pressure drag

The interaction effect on the pressure drag is demonstrated by employing numerical simulations for two example cases, namely, an isolated body and a *BLI* integrated vehicle. The latter case combines the same body element with an actuator disc model. The body element employs a body of revolution previously tested in the wind tunnel [95]: The length of this body L is 1.35 m and its diameter is 0.16 m. It denotes of the typical shape of an aircraft fuselage, consisting of a cylindrical mid-section, a front body, and a rear body. Being axisymmetric, the geometry of the

body is simplified as a 2-D profile that is interpolated between 100 equally spaced coordinate points. The actuator disc model placed at the body tail is 0.2 m in diameter, consisting of suction and pressure sides. The entire model is at the center of a 7.4*L*×3.7*L* rectangular domain, with an inflow velocity of 26 *m/s*. The simulated Mach number is 0.08, and the Reynolds number (based on the body length) is 2.3 million. The incompressible steady Reynolds-averaged Navier-Stokes (*RANS*) simulation is performed by employing the commercial software *FLUENT*®. The second order upwind discretization scheme is chosen for the simulation and uses the realizable k-ε model with the enhanced wall treatment for modelling the fully turbulent boundary layer. Determined by a mesh size dependence analysis, a structured mesh with 0.14 million cells is used for the simulation with the *y+* value of less than four. An identical mesh is used for both cases: the isolated body and the integrated vehicle. An actuator pressure jump (uniform pressure jump) of 42.5 Pa is assigned to maintain the equilibrium condition (*T=D*) of the vehicle.

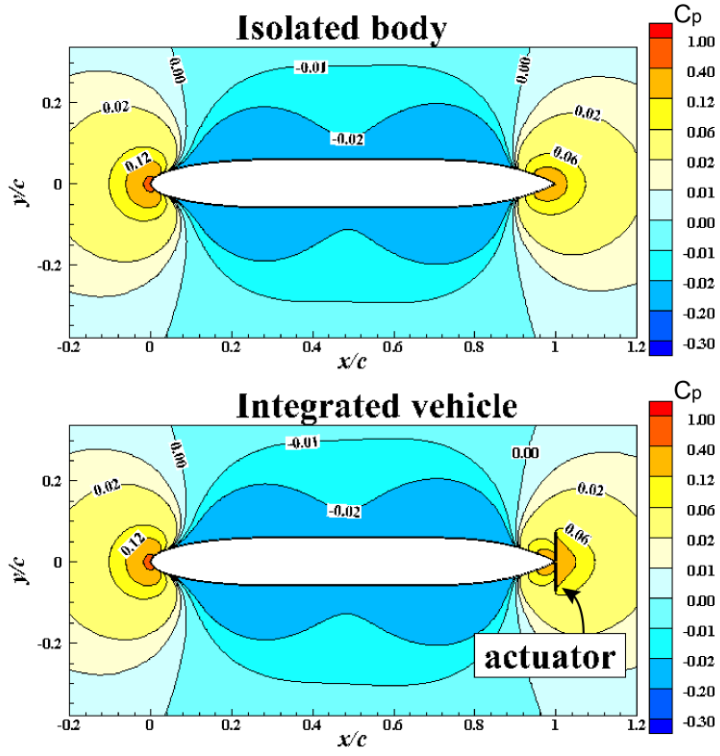

Fig. 3-10. Pressure coefficient contour of an isolated body (top) and an integrated vehicle (bottom), numerical simulation, 2D axisymmetric steady RANS.

The simulation results of body drag components are listed in Table 3-1. In the *BLI* configuration, the profile drag of the body is increased by 6.4%, mainly due to an increase in pressure drag (accounts for 6.1% increase). The increase in pressure drag can be elaborated by the change in the pressure distribution over the body surface. For the baseline case (isolated body), the pressure coefficient contours are shown in

Fig. 3-10 (top). The pressure recovery region is located at the rear of the body (0.8 ~1.0 *x/c*), where pressure gradually increases along the axis against the high pressure on the surface of the froe body. In the *BLI* configuration, the pressure distribution of the body is altered due to the presence of the actuator disc, particularly in the region before the propulsor, corresponding to the suction side of the actuator disc, as shown in Fig. 3-10 (bottom). Influenced by the propeller suction, the local pressure of the rear body is reduced, this weakens pressure recovery. As a result, the pressure drag of the body increases.

Table 3-1. Impact of BLI on the body drag

	$D_{pressure}$ (N)	$D_{viscous}$ (N)	$D_{profile}$ (N)
Isolated body	0.243	1.010	1.253
BLI integrated vehicle	0.320	1.013	1.333

Considering the actuator as a part of the vehicle, the increased body pressure drag corresponds to an increase in the required actuator thrust at the equilibrium condition. The extra suction at the aft body is compensated by the high pressure at the pressure side (back) of the actuator, as shown in Fig. 3-10 (bottom). In this case, the body/propulsor interaction causes a less adverse (positive) pressure gradient over the rear body in front of the suction side of propulsor. When the pressure recovery occurring over the surface of the rear body is partially shifted to the pressure side of the actuator, flow separation is less likely to occur at the rear body. As a result, this increase in pressure drag of the body should not be considered harmful to the performance of the entire vehicle.

ii. Impact on viscous drag

In the aforementioned simulation, the viscous drag (skin friction) acting on the body surface is slightly increased in the *BLI* configuration. The impact of body/propulsor interaction on the viscous drag of the body is illustrated in the following analysis for a simplified case, by assuming the body as a flat plate. Since there is no pressure drag for the flat plate, only skin friction contributes to the profile drag.

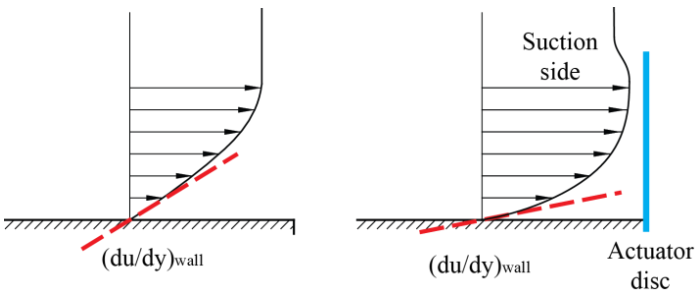

Fig. 3-11. Velocity gradient for an isolated plate (left) and the integrated plate (right).

For the isolated flat plate with a fully attached laminar *BL* (no separation), it can be assumed that the local viscous drag is proportional to the velocity gradient at the wall, as shown in the left side of Fig. 3-11. Once an actuator is placed at the end of the plate, the *BL* profile does not remain the same. In the region close to the actuator, as shown in the right side of Fig. 3-11, the flow accelerates toward the suction side of the actuator due to the negative pressure gradient, whereas the nonslip condition still holds at the wall. The interaction increases the velocity gradient at the wall (slope of the red dashed line), and hence the local viscous drag (wall shear stress). As a result, the total viscous drag of the flat plate increases, and a thinner boundary layer is observed. Similarly, this effect could be extended to the body with pressure drag component, as discussed previously.

Whereas both the pressure drag and viscous drag of the body can increase due to the body/propulsor interaction in *BLI* configuration, this situation is different for the *WI* configuration where no interaction effect is assumed. When applying the relationship between the drag force and power consumption, we can identify two different mechanisms of *BLI*: first, the interaction increases the body profile drag; second, the power-saving mechanism reduces the power consumption. These two mechanisms can explain the phenomenon reported in the wind-tunnel tests on the airship [43].

3.4.2 Power balance for the aircraft utilizing *BLI*

In the more complicated case of an aircraft utilizing *BLI*, the integrated vehicle can be extended by adding lifting and control surfaces, as demonstrated in Fig. 3-12 (left). The total airframe drag *D* of the aircraft contains more components than the body profile drag: for instance, lift induced drag, wing profile drag, wave drag, etc. The *CV* for the aircraft is built as shown on the top left of Fig. 3-12. The net force *N* of the entire aircraft is expressed by the momentum integral [Eqn. (3.44)], in which the pressure contribution is included. It is noted that the airframe drag *D* will increase due to the body/propulsor interaction:

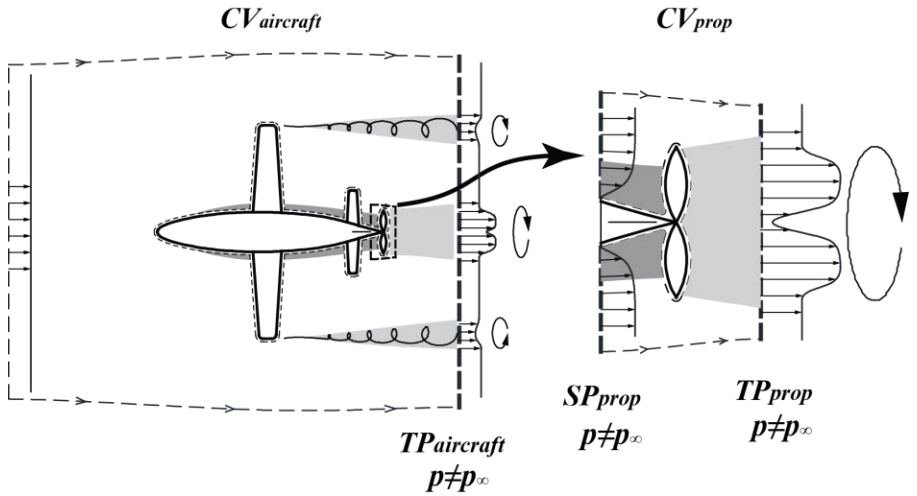

Fig. 3-12. *CV*s for the *BLI* integrated aircraft and the isolated *BLI* propulsor.

$$N = T - D = \iint_{TP}[(p - p_\infty) + \rho u(u - V_\infty)]dS \tag{3.44}$$

The power balance equation established for the $CV_{aircraft}$ is given in Eqn. (3.45). It has a similar form as Eqn. (3.35) for the *WI* integrated vehicle. Note that the power source is the shaft power P_W given by the propulsor. The power output and sink terms are NV_∞, the viscous dissipation within the $CV_{aircraft}$, and the wake energy outflow through the $TP_{aircraft}$. The wake energy outflow contains the *KE* deposition rate (including axial and transverse components $\dot{E}_a$ + $\dot{E}_v$) and pressure-work deposition rate $\dot{E}_p$, as introduced in the wake system:

$$P_W = NV_\infty + \Phi_{CV,aircraft} + \left(K\dot{E}_w + \dot{E}_p\right)_{TP,aircraft} \tag{3.45}$$

For the propulsor of the aircraft, CV_{prop} can be extracted from the $CV_{aircraft}$ as shown in Fig. 3-12 (right). The power balance for the *CV* of this *BLI* propulsor can be written as in Eqn. (3.46). The power input consists of the wake energy ($K\dot{E}_w$ + $\dot{E}_p$) of the boundary-layer flow which enters the CV_{prop} through SP_{prop}, and the shaft power P_W. It is noted that the pressure-work deposition rate $\dot{E}_p$ is included as a component of the wake energy. The power output contains TV_∞, the wake energy outflow through TP_{prop}, and the viscous dissipation within CV_{prop}. The propulsor shares the similar power saving mechanism as the *WI* actuator (3.23).

$$\left(K\dot{E}_w + \dot{E}_p\right)_{SP,prop} + P_W = TV_\infty + \left(K\dot{E}_w + \dot{E}_p\right)_{TP,prop} + \Phi_{CV,prop} \tag{3.46}$$

This brief discussion entails that, when considering the aircraft design using *BLI*, the minimization of the airframe drag might not be an optimal criterion for performance optimization. Given a typical approach followed by the aircraft industry in separately designing airframe and propulsion units, separate guidelines are followed that minimize the aircraft airframe drag from one side and the power consumption from the other. By taking into account the body/propulsor interaction and the power-saving mechanism, a criterion for minimization of power consumption should be used when optimizing the aircraft design using *BLI*.

3.5 Conclusions

In the present chapter, a conceptual analysis of the power conversion in the *WI* and the *BLI* configurations has been carried out. The main conclusions are summarized in the following:

1. In both the *BLI* and the *WI* configuration, the propulsor uses the wake energy (mainly the axial kinetic energy and the pressure work) of body wake flow and reduces the wake energy of the downstream wake flow, thereby reducing the power consumption to generate an equivalent thrust at the same flight condition.
2. The energy flow rate of the body wake (boundary layer) is mainly responsible for power coefficients being greater than one. It is considered as a power input for

the *WI* (*BLI*) propulsor but as a transient power for the integrated vehicle (aircraft).

3. For a body with fully attached boundary layer in isolation, the body/propulsor interaction increases the body drag in the *BLI* configuration. This effect is not detrimental to the performance because the interaction partially shifts the pressure recovery to the pressure side of the propulsor.
4. To design an aircraft using *BLI*, it is suggested to use minimization of the effective power consumption as the design criteria rather than solely focusing on airframe drag.

Chapter 4 Power balance method applied to numerical simulations

The previous chapter discussed the theory and the mechanisms of *BLI*, namely the power saving mechanism, and the body/propulsor interaction. The Power Balance Method (*PBM*) was used to investigate the power conversions related to *BLI*. This chapter is dedicated to investigating the mechanisms of *BLI* through numerical simulations. The Power Balance Method (*PBM*) is used to post process the simulation data such that the detailed processes involved in the power conversion can be determined. Two main objectives of this chapter are:

- Establishing the detailed process of typical power conversions for an isolated actuator disc, an isolated flat plate and a vehicle which combines the actuator and the flat plate in a *BLI* configuration;
- Quantifying the various influence of *BLI* and analysing the mechanisms in order to support the theoretical analysis.

To achieve these two major objectives, the analysis of power is restricted to only mechanical powers. That excludes the thermal power in numerical simulations. Additionally, numerical simulations are limited to 2D (planar) steady laminar incompressible flows, which allows the exclusion of complicated flow physics, such as turbulence, compressibility, etc. This simplification allows the analysis to focus on the mechanisms elaborated in the theoretical analysis of *BLI* in Chapter 3.

The presented simulation study primarily analyzes power conversions of axial wake flows, a classical actuator disc, a flat plate, and an integrated vehicle which combines the actuator disc and the plate in a *BLI* configuration. These typical power conversions are closely related to the mechanisms of *BLI*. To establish a progressive understanding, this chapter is organized as follows: Section 4.1 introduces the principle of combining *PBM* with numerical simulations. In Section 4.2, the *PBM* is applied to the simulations of wake flows, namely a jet wake and a body wake. Section 4.3 analyzes the typical power conversion processes of an actuator disc and flat plate. Section 4.4 discusses the simulation of the integrated vehicle utilizing *BLI*. The main conclusions of this research are summarized in Section 4.5.

4.1 Power balance method in Computation Fluid Dynamics

The Computation Fluid Dynamics (*CFD*) is a tool extensively used in the research of aircraft [96]. As compared to experiments, such as the wind tunnel test and flight test, *CFD* simulations are usually less expensive and less time-consuming. A validated *CFD* code is also capable of providing credible results [97, 98]. *CFD* simulations resolve a computational domain, obtaining the flow field with fine details. The *PBM* is a method which evaluates “powers” of the flow [33]. It might be possible to combine *PBM* with *CFD* simulations. The subsequent paragraphs elaborate as to why *PBM* can be used to process the flow field from numerical simulations.

4.1.1 Compatibility between finite volume method and power balance method

Depending on the numerical method of solving partial differential equations, *CFD* can be classified as a finite volume, finite difference, or finite element method. [96]. Despite the choice of the method, conservation laws shall be satisfied in *CFD* simulation.

In fluid mechanics, the mechanical energy equation is different from the general energy equation [46]. The former is derived from the momentum equation, consisting of the energy terms of kinetic energy, pressure work, and viscous dissipation. The latter equation is about the first law of thermodynamics, additionally including thermal energy. The diagram in Fig. 4-1 shows the relation between the conservations of energy and mechanical energy. On the other side, *PBM* uses an integral form of the mechanical energy equation [33, 46]. In principle, *PBM* should comply with the *CFD* simulation when conservation laws are satisfied.

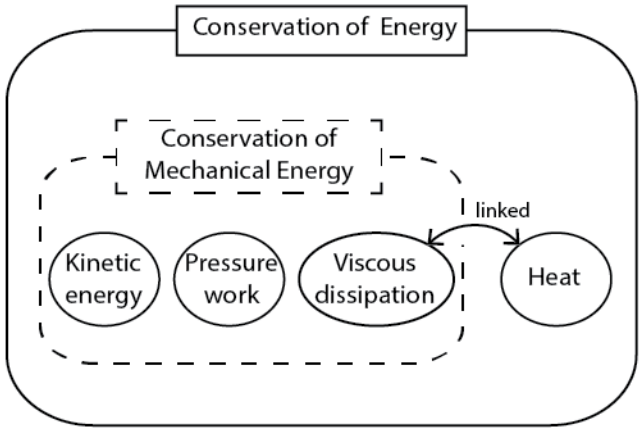

Fig. 4-1. The diagram of the conservation of total energy and mechanical energy.

The top drawing of Fig. 4-2 illustrates the simplified flowchart of the *CFD* simulation that utilizes the Finite Volume Method (*FVM*) to solve the Naiver-Stokes equations. For the simulation, an entire computational domain is discretized into a large number of finite control volumes. The *FVM* computes flow variables of an individual volume such that the conservation of mass, momentum and energy are satisfied. Meanwhile, the flux of the conserved quantities is transferred to the adjacent volumes, such that conservation laws can be satisfied within the entire domain. On the other side, *PBM* applies the integral form of the mechanical energy equation, which is obtained by multiplying the momentum equation (vector form) with velocity (vector) [33, 46]. As a result, the mechanical energy conservation for the entire computational domain should be satisfied. This relation between *PBM* and *FVM* is schematically shown in Fig. 4-2. Note that the total energy conservation is satisfied in *CFD* simulation, but the thermal energy is not included in *PBM* because it is deemed as less relevant in the discussion of the conversion of mechanical

energy. The above discussion implies that *PBM* complies with the numerical simulation using *FVM*, which is available in most of the commercial *CFD* software.

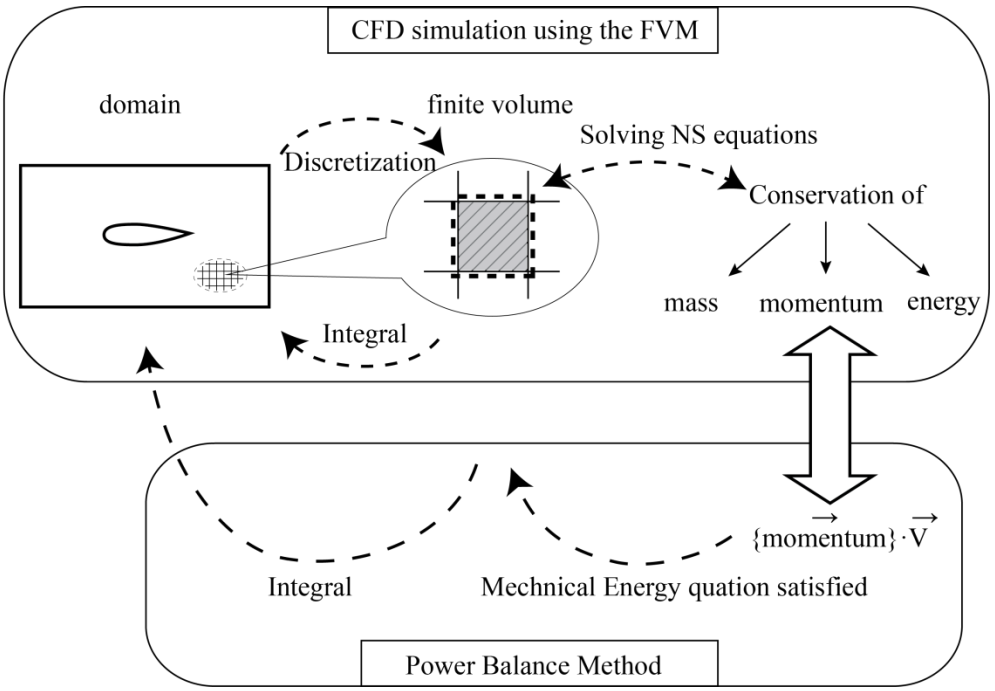

Fig. 4-2. Diagram of Power Balance Method to process the flow field of the simulation using the Finite Volume Method.

4.1.2 Computational domain

The *PBM* shows power terms at corresponding Trefftz Planes (*TP*), such that the change in power can be tracked and power conversion can be analyzed. A special computational domain in CFD simulations is required for *PBM*, as introduced in the following paragraphs.

For a 2D computational domain with the horizontal free stream velocity vector V_∞, a *TP* is defined as a vertical plane to assess powers such as energy deposition rates. Series of vertical *TP*s are placed along the *x*-axis to illustrate the change of energy deposition rates. These *TP*s separate the entire domain into individual Control Volumes (*CV*), as shown in the top of Fig. 4-3. For a certain *TP* denoted by the TP_i, a corresponding subdomain CV_i is defined as the collection of individual domains from the first individual *CV* to the one just upstream the TP_i. This subdomain is used to evaluate the power in the form of volume integral, such that *PBM* shows the viscous dissipation rate Φ_i at different *x* locations, and thus traces the change of Φ_i.

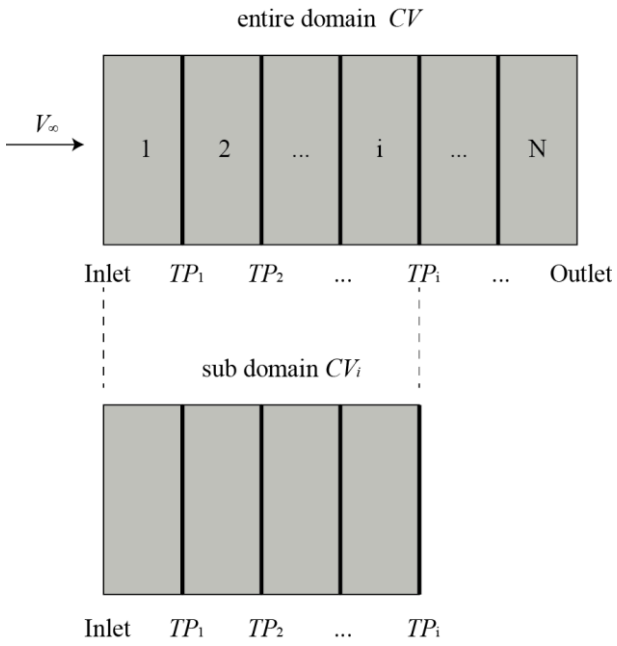

Fig. 4-3. Control volume definition and domain division.

Power terms in this defined computational domain can be evaluated. The wake kinetic energy flow $K\dot{E}_w$ and the pressure work-defect rate $\dot{E}_p$ correspond to a certain TP_i. By using *SI* units for all flow variables, the unit of mechanical power term is [W].

4.2 Power balance method in simulations of jet wake and body wake

This section discusses the power conversion for two simple cases, namely a jet wake and a body wake. Their flow fields are obtained from 2D steady laminar incompressible Navier-Stokes *CFD* simulations. In the *PBM* applied to a computational domain, $K\dot{E}_{w,\iota}$, $\dot{E}_{p,i}$ and Φ_i are the involved mechanical powers for the wakes. The three powers establish a power balance equation as in Eqn. (4.1). As discussed in Chapter 3, $\dot{E}_{w,i}$ denotes the wake energy flow rate evaluated at an arbitrary TP_i, consisting of $K\dot{E}_{w,\iota}$ and $\dot{E}_{p,i}$ as in Eqn. (4.2). Φ_i is the viscous dissipation in a subdomain CV_i. The summation of $\dot{E}_{w,i}$ and Φ_i shall be constant. As a total power of the wake, the summed power for the arbitrary TP_i should be equal to the total power $\dot{E}_{w,inlet}$ for the inlet.

$$K\dot{E}_{w,\iota} + \dot{E}_{p,i} + \Phi_i = \dot{E}_{w,i} + \Phi_i = \dot{E}_{w,inlet} = const \tag{4.1}$$

$$K\dot{E}_{w,\iota} + \dot{E}_{p,i} = \dot{E}_{w,i} \tag{4.2}$$

The results of *CFD* simulations usually contain numerical errors. Therefore, the equation (4.1) might not be explicitly satisfied. This discrepancy is evaluated as an

error defined in Eqn. (4.3). This error is the relative difference between the total powers of the wake accessed at the TP_i and the inlet.

$$error = \frac{(\dot{E}_{w,i}+\Phi_i)-\dot{E}_{w,inlet}}{\dot{E}_{w,inlet}} \tag{4.3}$$

4.2.1 PBM applied to jet wake

A simple jet wake model is defined by its axial velocity u_j, higher than V_∞, with ambient pressure p_∞ at the inlet. In this case, the u_j at the inlet is 12 *m/s*, with V_∞ of 10 *m/s*. The (half) width of the jet w_j is 0.01 *m*. The Reynolds number based on the wake height is about 1400, indicating that the flow is laminar. The air is set to have a density of 1.225 kg/m^3 and a viscosity of 1.7894×10^{-5} Ns/m^2. The jet wake enters a $5w_j \times 12w_j$ rectangular domain, as shown in Fig. 4-4 (top). The domain is bounded by a vertical inlet, a vertical outlet, and two horizontal planes (top and bottom planes). The bottom plane is defined as a symmetry boundary for this symmetrical flow model. The top plane is also set as a symmetry plane to prevent flow penetration. There are 4 *TP*s inside the domain as interior planes, as shown in Fig. 4-4 (bottom). These *TP*s separate the domain into individual volumes that combine corresponding subdomains.

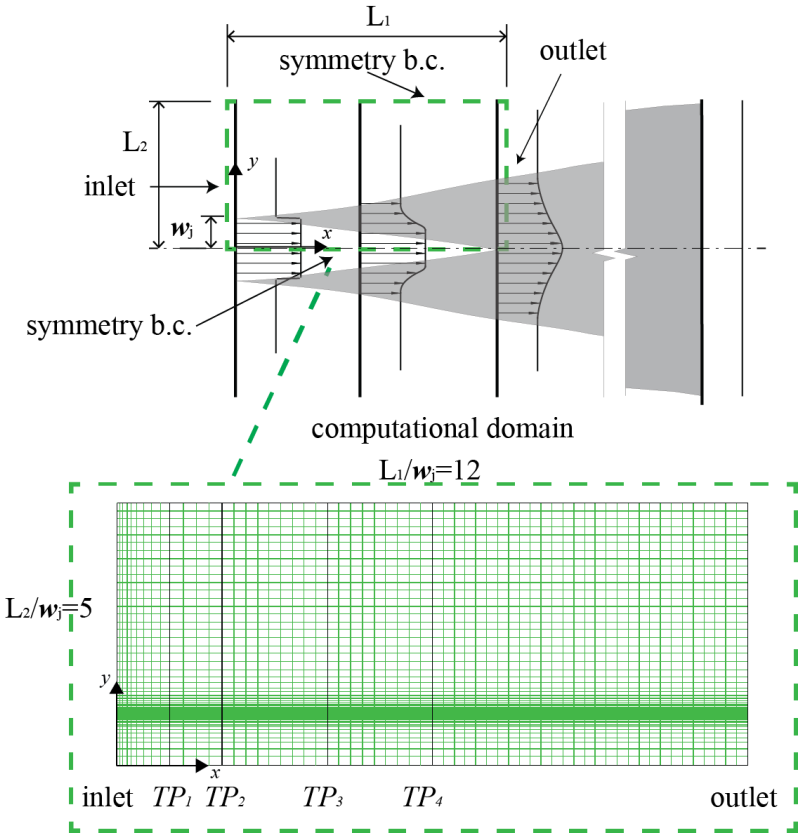

Fig. 4-4. A jet wake flow Domain and the definition of the computational domain.

The simulation employs the commercial software *FLUENT*™, using structural mesh with 4680 cells (determined by a mesh size dependence analysis). The mesh is refined near the shear layer region, as shown in the bottom of Fig. 4-4. A simple mesh size sensitivity study was conducted, showing a 0.1% difference in the total viscous dissipation when the mesh density of the domain was increased by 4 times. The simulation uses the second order upwind for spatial discretization and the *SIMPLE* scheme for the pressure-velocity coupling [96, 99, 100].

The *PBM* is used after the simulation to process the flow field. Table 4-1 presents the involved power terms accessed at various x locations. $K\dot{E}_{w,\iota}$ and Φ_i are calculated by using the expressions in Section 3.2. It is noted that $\dot{E}_{p,i}$ has a zero value, and hence is not listed. This is because of the constant pressure p_∞ in the flow field. As a result, $\dot{E}_{w,i}$ is equal to $K\dot{E}_{w,\iota}$ when $\dot{E}_{p,i}$ is zero.

Table 4-1. Power terms at various locations of *TP*s in the simulation of a jet wake

x/w_j	Plane	$K\dot{E}_{w,\iota}\,(W)$	$\Phi_i\,(W)$	$\dot{E}_{w,i} + \Phi_i\,(W)$	$\Phi_i / \dot{E}_{w,inlet}$	error
0	inlet	0.2940	-	0.2940	0.00%	0
1	TP_1	0.2912	0.0024	0.2936	0.82%	0.14%
2	TP_2	0.2901	0.0034	0.2935	1.17%	0.16%
4	TP_3	0.2885	0.0049	0.2934	1.67%	0.20%
6	TP_4	0.2873	0.0060	0.2934	2.06%	0.22%
12	outlet	0.2847	0.0086	0.2932	2.92%	0.26%

The change of power for the jet wake is shown in Fig. 4-5. The top picture shows the contours of the integrand of Φ. The high-intensity region corresponds to the viscous shear layer. This picture also plots velocity profiles, showing that the profiles are flattened when the jet flows downstream. The bottom figure visualizes the change of powers. The X-axis denotes the x location of *TP*s, and Y-axis corresponds to the powers tabulated in Table 4-1. This figure illustrates the power conversion process of the jet wake: Dissipation Φ (red dashed line) irreversibly increases along with the x axis, while $K\dot{E}_w$ (the gap between the two power lines) gradually reduces. The summation of $K\dot{E}_w$ and Φ is almost constant as a total power. At the outlet, 2.92% of the total power is converted into dissipation Φ.

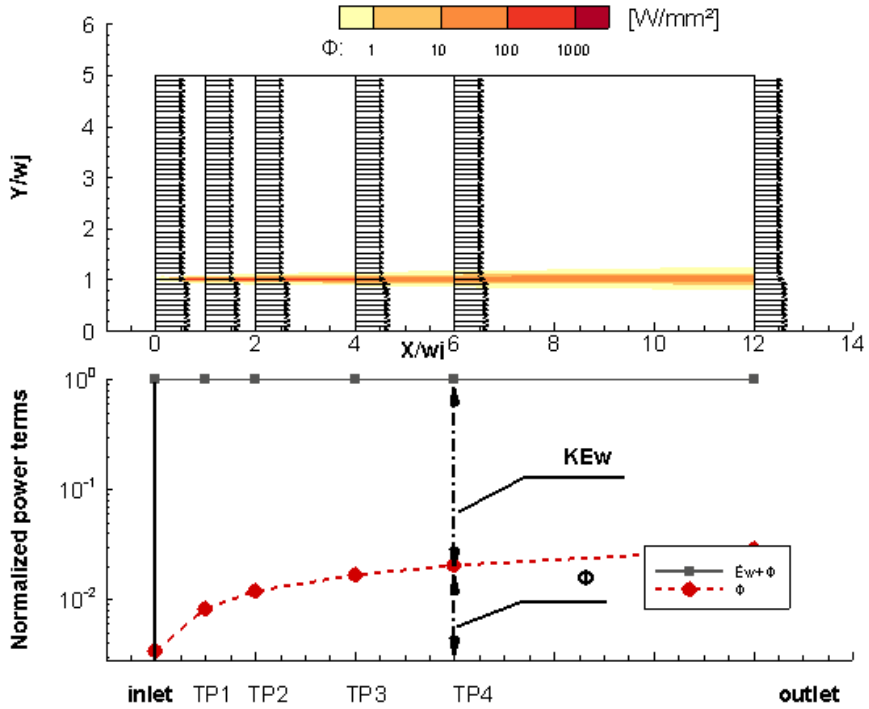

Fig. 4-5. Contours of the integrand of viscous dissipation (top) and the power conversion of the jet wake (bottom).

A tiny reduction of the total power along the *x* axis can be noted. This reduction is evaluated as an error expressed by Eqn. (4.3), whose value is 0.26% for the outlet. The error might result from the numerical errors of *CFD* simulation, such as artificial dissipation and residuals [96, 101, 102]. Considering the small impact on the analysis, this error is not discussed further.

4.2.2 PBM applied to body wake

Beside of the jet wake, the body wake is another important flow parameter for the understanding of *BLI*. As discussed in Chapter 3, a body wake is downstream of a boundary layer flow, characterized by its axial velocity u lower than V_∞. The following paragraphs analyze the power conversion of a typical body wake.

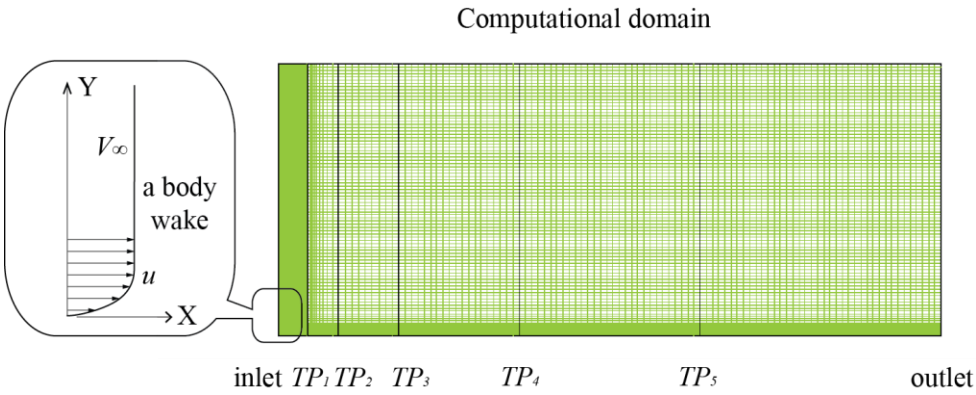

Fig. 4-6. A body wake enters a computational domain.

In the *CFD* simulation, a velocity profile of a body wake is assigned to the rectangular domain of 0.05 $m \times 0.11$ m, as shown in Fig. 4-6. The profile is obtained from another simulation, such as the boundary layer profile at the trailing edge of a flat plate, which is elaborated with more details in Section 4.3. The Reynolds number of the flow over the flat plate is 6850 (based on the flat plate length L, 0.01m), thereby allowing the flow to be simulated as laminar. The domain is shown in Fig. 4-6 includes 22000 cells, with 5 *TP*s to analyze the flow development along the x axis. The simulation of the body wake applies the same conditions and discretization methods as in the previous case of the jet wake.

Table 4-2. Power terms vs x locations of *TP*s in the simulation of a body wake

X/L	Plane	$K\dot{E}_{w,\iota}$ (W)	$\dot{E}_{p,i}$	Φ_i (W)	$\dot{E}_{w,i} + \Phi_i$ (W)	error
0	inlet	0.0196	0.0051	-	0.0247	0
0.5	TP_1	0.0166	-0.0002	0.0084	0.0248	0.35%
1	TP_2	0.0132	-0.0001	0.0117	0.0249	0.59%
2	TP_3	0.0099	-0.0000	0.0149	0.0248	0.34%
4	TP_4	0.0071	-0.0000	0.0177	0.0248	0.34%
7	TP_5	0.0053	-0.0000	0.0195	0.0248	0.36%
9	outlet	0.0042	-0.0000	0.0206	0.0248	0.38%

The *PBM* is used to process the flow field of the body wake, such that the three powers, $K\dot{E}_{w,\iota}$, $\dot{E}_{p,i}$ and Φ_i are evaluated. Table 4-2 lists these powers, their summation and the error. It should be noted that the pressure work rate $\dot{E}_{p,i}$ for this body wake is non-zero and positive at the location of the inlet, $\dot{E}_{p,i}$ becomes nagative with a small value after the inlet. This is because the pressure at the inlet is smaller than p_∞, and then pressure becomes slightly higher than p_∞ after the inlet. This might be associated with the inlet boundary condition: the flow represented by a velocity profile is forced to flow through a parallel channel. Despite this phenomenon, the

summation of the three powers is constant along the *x* axis, with the error for any *TP* being lower than 0.6%.

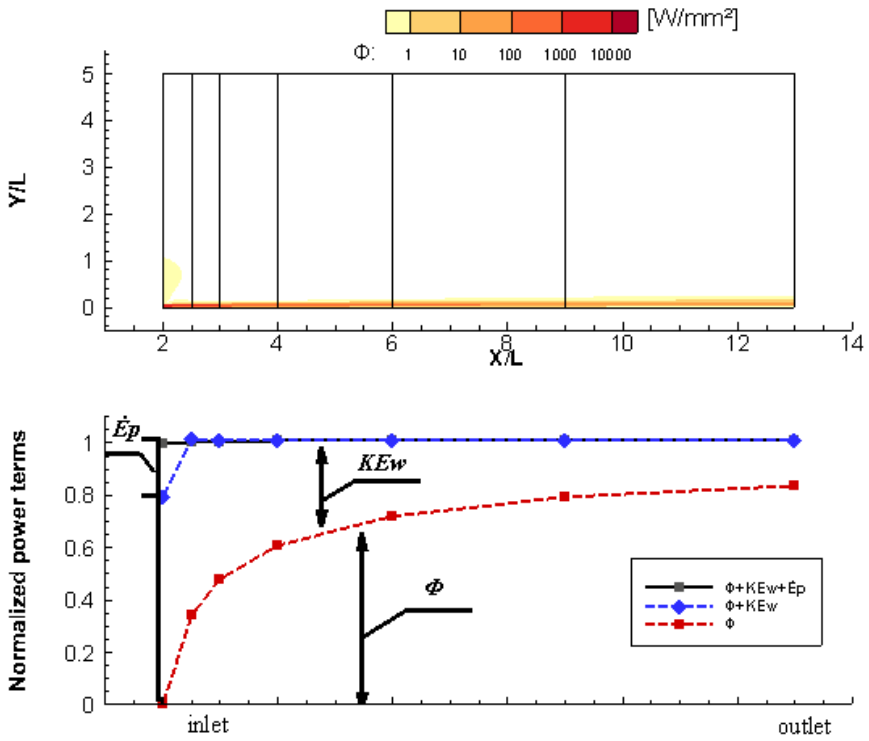

Fig. 4-7. Contours of the integrand of viscous dissipation (top) and power conversion of the body wake flow (bottom).

The results of this study are presented in Fig. 4-7. The contours in the top figure show that the Φ is most intensive in the region near the inlet. The bottom plot in Fig. 4-7 presents the powers of the body wake at the corresponding *x* location, showing the power conversion process. The total power of the body wake is constant, and Φ consistently increases. The $\dot{E}_p$ at the inlet is reduced along the *x* axis and completely dropped out at the TP_1 where the pressure is stabilized to p_∞. The transferring of $\dot{E}_p$ and the conversion of Φ occur at the same time in the small space between the inlet and TP_1. In this small region, about 1/3 of the total power is converted into viscous dissipation.

4.3 Power balance method in simulations of an actuator disc and a flat plate

In the above paragraphs, the power conversions of a jet wake and a body wake are quantitatively analyzed by processing the flow field obtained from *CFD* simulations. A key feature of both analyses discussed above is the conservation of the total power of wakes along the *x* axis. This section discusses the power conversion of two more cases, namely a classical actuator disc and a flat plate.

This section aims to enhance the understanding of *BLI* by analyzing the power conversions of an actuator disc and a flat plate, and next section looks into an integrated vehicle that assembles the actuator disc and plate in a *BLI* configuration. The *CFD* simulations of the three models employ a common computational domain, such that influences of model geometry and mesh are excluded when comparing the power-conversions. The domain is 0.05 m × 0.13 m in dimension and separated by 9 *TP*s, as shown in Fig. 4-8. The flat plate is aligned with the symmetry plane and the actuator is placed at the trailing edge (*TE*) of the plate. With simple modifications of boundary conditions, this domain can be used in each of the three simulations. These modifications for each model are elaborated accordingly in the following paragraphs.

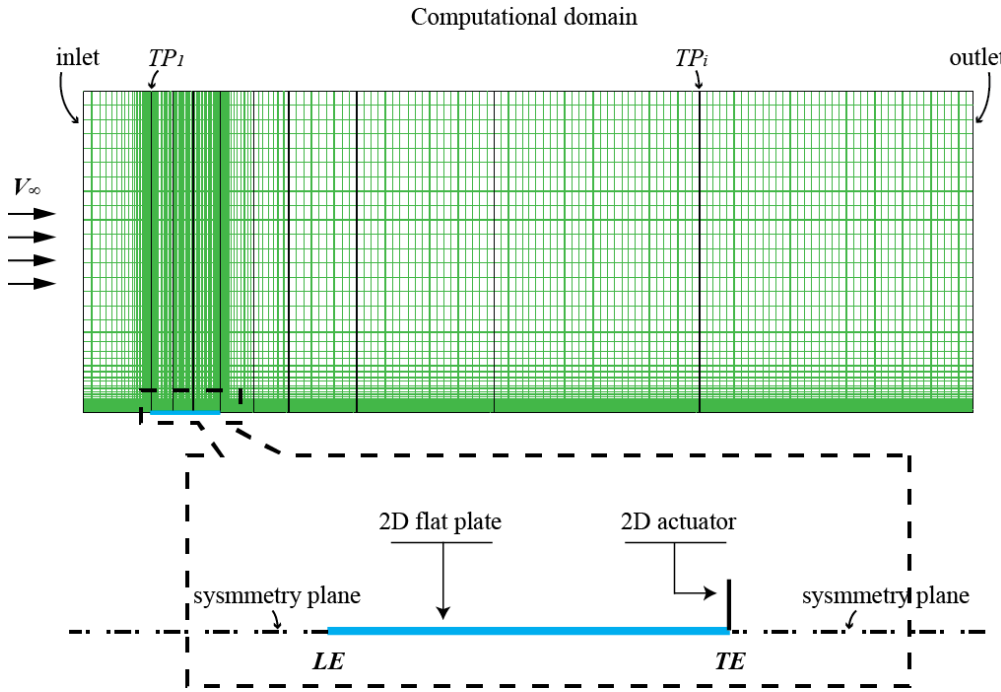

Fig. 4-8. A common computational domain for an actuator disc, a flat plate, and an integrated vehicle model

4.3.1 PBM applied to an actuator disc model

This part discusses a simulation performed for an actuator disc which represents a propeller model that accelerates free stream airflow. As introduced in Chapter 2, the flow for the classical actuator disc is considered to be axial and inviscid. This study assumes the flow to be 2D and viscous, such that 2D laminar simulation can still be performed for the actuator disc. The simulation utilizes the computation domain shown in Fig. 4-8, where a pressure jump (line) plane represents the actuator disc and a symmetry plane replaces the boundary of a flat plate. The plane of actuator disc is 0.0006 m^2 in area A, with a constant pressure jump ΔP of 200 *Pascal*. Therefore, this actuator disc model generates a thrust of 0.12N (T=$\Delta p \times A$). The

inflow velocity V_∞ is 10m/s, corresponding to a Reynolds number of 6850 (based on the length of 2D plate, 0.01m) and the Mach number of 0.03.

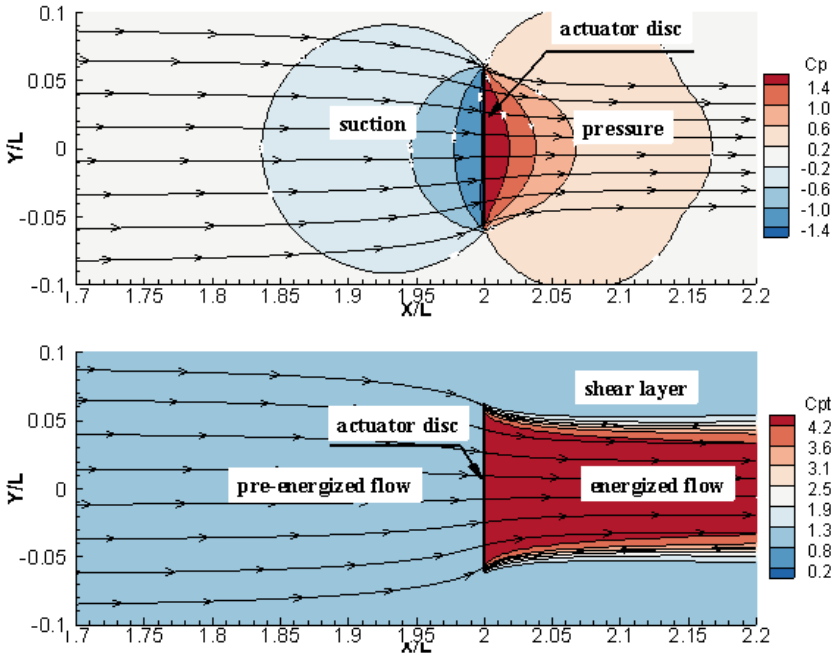

Fig. 4-9. Contours of pressure coefficient (top) and the coefficient of total pressure (bottom) around an actuator disc, including a mirrored flow field

The simulation applies the same method as elaborated in the previous cases of the wakes, obtaining a flow field around the actuator disc. In the top figure of Fig. 4-9, the contours of pressure coefficient show a suction region and a high-pressure region on the suction side and the pressure side respectively. The streamlines indicate a contraction of the flow. The bottom figure of Fig. 4-9 illustrates the contours of total pressure coefficient. The abrupt increase in total pressure with air passing through the actuator disc indicates that it energizes the flow. The energized flow is actually the jet wake behind the actuator disc. The shear layer of the jet wake is highlighted by the decrease of total pressure towards the outer flows of the jet wake. Once the flow is extended to be 2 dimensional and viscous, the power balance equation for the classical actuator disc in Chapter 3 is modified, as shown in Eqn. (4.4).

$$P_K = TV_\infty + \dot{E}_w + \Phi \tag{4.4}$$

$$P_K = \oiint_{actuator}(p - p_\infty) \cdot udS = \int_{actuator} \Delta p \cdot udS \tag{4.5}$$

A notable change is the addition of viscous dissipation of Φ as power output. The wake energy flow rate $\dot{E}_w$ in Eqn. (4.4) is also extended, including the wake kinetic energy $K\dot{E}_w$ and pressure work rate $\dot{E}_p$. Furthermore, the input power given

by actuator disc is modified as mechanical energy addition rate P_K [33], expressed as Eqn. (4.5). P_K is used in this study because its surface integral relies on the actuator (line) plane as a well-defined boundary[1].

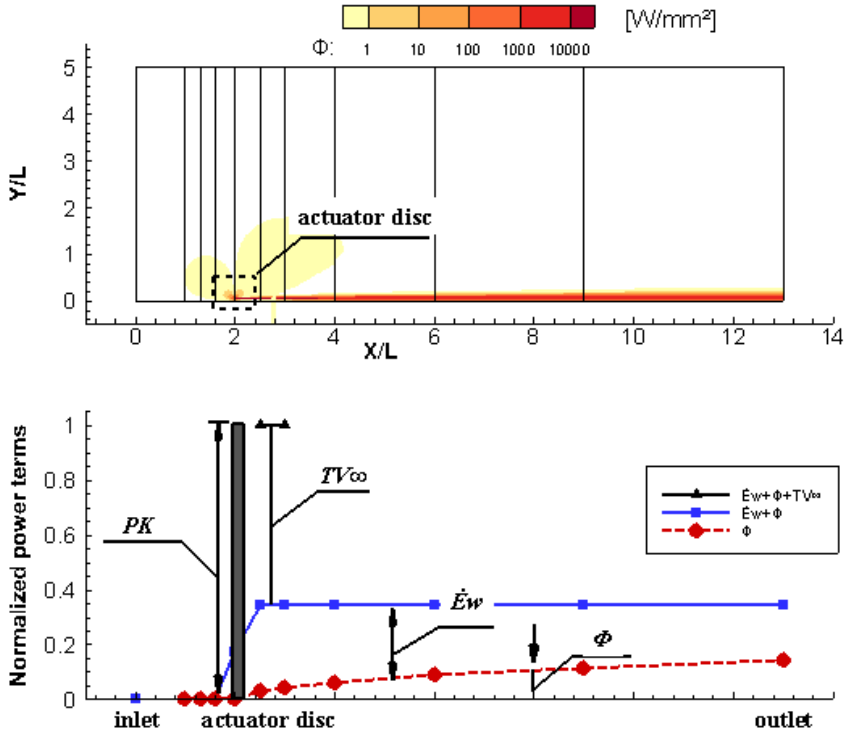

Fig. 4-10. Contours of the integrand of viscous dissipation (top) and power conversion of the actuator disc (bottom)

The *PBM* is used to analyze the flow field around the actuator disc. The involved powers in Eqn. (4.4) are evaluated according to their expressions. These powers are plotted for clarity. The top figure in Fig. 4-10 shows the integrand of Φ and also displays the x locations of the actuator disc and *TP*s. The plot of power conversions is shown in the bottom of Fig. 4-10. The input power of P_K is calculated with the Eqn. (4.5), obtaining a value of 1.836 W (denoted by the height of a shaded bar). As two output powers, the powers of Φ and $\dot{E}_{w,}$ are evaluated and plotted at corresponding x locations. The summation of these two powers behind the actuator disc is constant (a blue curve denotes $\Phi + \dot{E}_w$). The power output of TV_∞ is simply T (0.12N) multiplied with V_∞ (10m/s), obtaining a value of 1.2 W (denoted by the gap between the blue curve and the short black curve for $\Phi + \dot{E}_w + TV_\infty$). It is noted that

[1] P_K apples surface integral over the inner boundary of a *CV*. While the *KE* production rate $K\dot{E}_p$ introduced in Chapter 3 uses surface integral over the external boundary of the *CV*. The two expressions of input power can be correlated as: $P_K = K\dot{E}_p + \Phi_{CV}$.

P_K is almost equal to the value of $\Phi + \dot{E}_w + TV_\infty$. A tiny inequality (0.6%) between them is attributed to the error of the *CFD* simulation.

With *PBM* processing the simulation data, the bottom plot in Fig. 4-10 clearly shows the typical power conversion of an actuator disc model: the mechanical energy addition P_K given by the actuator disc partially becomes TV_∞ (TV_∞ making up 65.4% of the P_K. Note that the classical definition of power (propulsive) coefficient ($TV_\infty/K\dot{E}_{p,}$) gives a value of 76.1%. The high value of the power coefficient is attributed to its denominator which excludes the viscous dissipation within the *CV*). The rest of P_K is transferred into the $\dot{E}_w$ of the jet wake. In the downstream region behind the actuator disc, $\dot{E}_w$ gradually reduced due to viscous dissipation Φ.

4.3.2 PBM applied to a flat plate model

This part discusses the *CFD* simulation of a flat plate. The computational domain shown in Fig. 4-8 is used for this simulation. The boundary condition of the flat plate is kept as a wall. Nevertheless, in the current simulation, the actuator disc plane in the previous simulation is changed to be an interior plane. The plate is $0.01m$ in length L. The speed of incoming airflow V_∞ is 10 m/s. The Reynolds number is approximately 6850 (based on the length of plate L). A 2D laminar simulation is performed for this flat plate model, with same model settings as previously discussed in the simulations of wakes.

The force exerted on the flat plate is the viscous drag D. As introduced in Chapter 3, the power balance equation for this flat plate is given by Eqn. (4.6). The drag power (DV_∞) is an input power to the flat plate. The output powers are the viscous dissipation Φ and the wake energy flow rate $\dot{E}_w$.

$$DV_\infty = \Phi + \dot{E}_w \tag{4.6}$$

The simulation computes the flow field, and then *PBM* is used to analyze the powers. The top of Fig. 4-11 shows the intensity of Φ and the x locations of *TP*s. The boundary layer of the plate is denoted by the contours between the Leading Edge (*LE*) and the Trailing Edge (*TE*). The body wake of the plate is characterized by the contours downstream of the *TE*. The change in the various powers is plotted in the bottom of Fig. 4-11. The viscous drag D obtained from the simulation is 0.0106 N. Thus DV_∞ is 0.106 W, which is represented by the height of the rectangle. The Φ and $\dot{E}_w$ are calculated and plotted at the corresponding x locations. The bottom plot shows that DV_∞ is almost equal to the value of ($\Phi + \dot{E}_w$) at the *TE*. The relative difference between them is about 0.7 %, the numerical error of the simulation.

The bottom plot shows the power conversion of the flat plate. The input power of DV_∞ is converted into Φ and $\dot{E}_w$. The Φ increases rapidly along the x-axis in the region of the boundary layer (between the *LE* and *TE*). About 40% of the input power is dissipated from the *LE* to the location of 30% L. The Φ evaluated at the *TE* denotes the boundary layer dissipation Φ_{BL}, making 76.5% of the power input. This also indicates the rest portion is 23.5%, corresponding to the $\dot{E}_w$ of the body wake.

This portion is slightly higher than the value given by Drela (about 21%) [33]. This difference in portion might be attributed to the blockage effect caused by the rectangular computational domain. The blockage effect is excluded in the theoretical analysis.

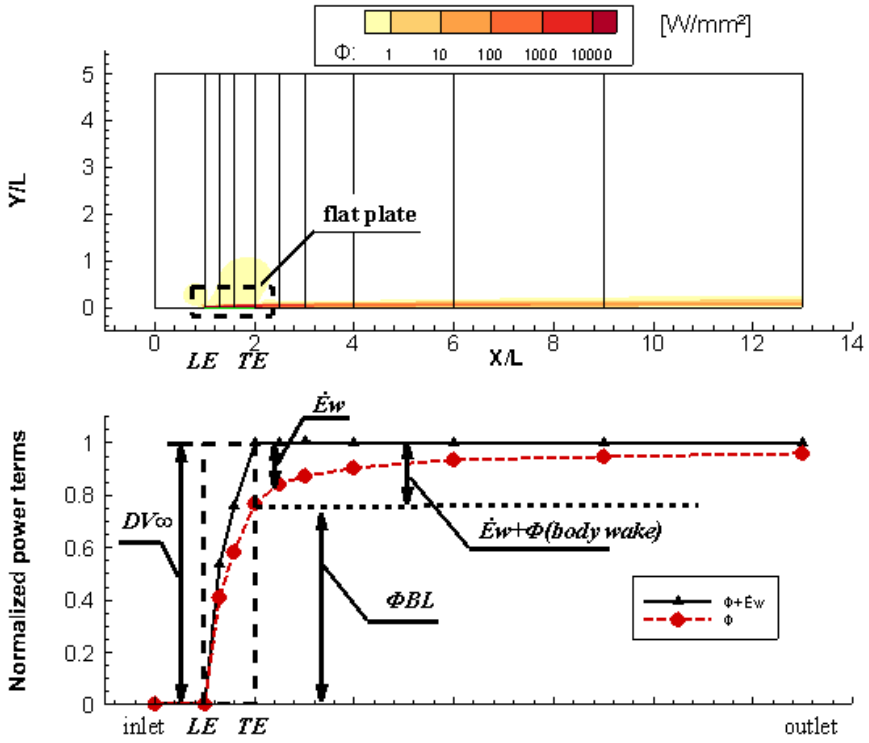

Fig. 4-11. Contours of the integrand of viscous dissipation (top) and the power conversion process for a flat plate (bottom)

A change of $\dot{E}_w$ is highlighted in the analysis. The change of $\dot{E}_w$ along the *x*-axis is increasing in the region of the boundary layer (between *LE* to the *TE*), but decreasing in the region of body wake (behind the *TE*). This difference is attributed to two boundary conditions: the non-slip wall condition and the far-field condition. The wall condition of the flat plate tends to decelerate the boundary layer flow, increasing the $\dot{E}_w$. On the other hand, the condition of the far field tends to accelerate body wake flow to reach the velocity of V_∞, thereby decreasing the $\dot{E}_w$. Despite the different change along the *x* axis, $\dot{E}_w$ is clearly a product of DV_∞ of the flat plate. The special role of $\dot{E}_w$ is further investigated in the subsequent case of an integrated vehicle using *BLI*.

4.4 Power balance method in simulations of an integrated vehicle

This section presents a simulation study of an integrated vehicle combining a flat plate with a wake filling actuator disc model in a *BLI* configuration. This study aims

to analyze the mechanisms of *BLI*, focusing on the power conversion and the body/propulsor interaction.

The *CFD* simulation of the vehicle uses the computational domain shown in Fig. 4-8. The wake filling actuator disc is placed at the *TE* of the plate, such that the actuator disc model is ingesting the boundary layer. The boundary condition of the flat plate is kept as a no-slip wall condition. The actuator disc model is represented by a pressure jump plane with a non-uniform distribution of Δp, such that the model perfectly refills the total pressure defect[2] of the boundary layer flow [69].

$$\Delta p(y) = \Delta p_t(y) = p_{t,const} - p_{t,upstr}(y) \tag{4.7}$$

During the computation process of simulation, the value of Δp is updated through a User Defined Function (*UDF*). The Δp is obtained by subtracting a constant total pressure $p_{t,const}$ with the total pressure $p_{t,upstr}$ probed at an upstream plane in front of the actuator model, as shown in Eqn. (4.7). The scheme of the wake filling actuator disc is illustrated in Fig. 4-12. To maintain an perfect equilibrium (T=D) is tricky in this simulation, thus $p_{t,const}$ is defined to be slightly higher than the total pressure of free stream $p_{t\infty}$ in the *UDF*. This leads to the thrust T higher than the drag D (N is slightly higher than zero).

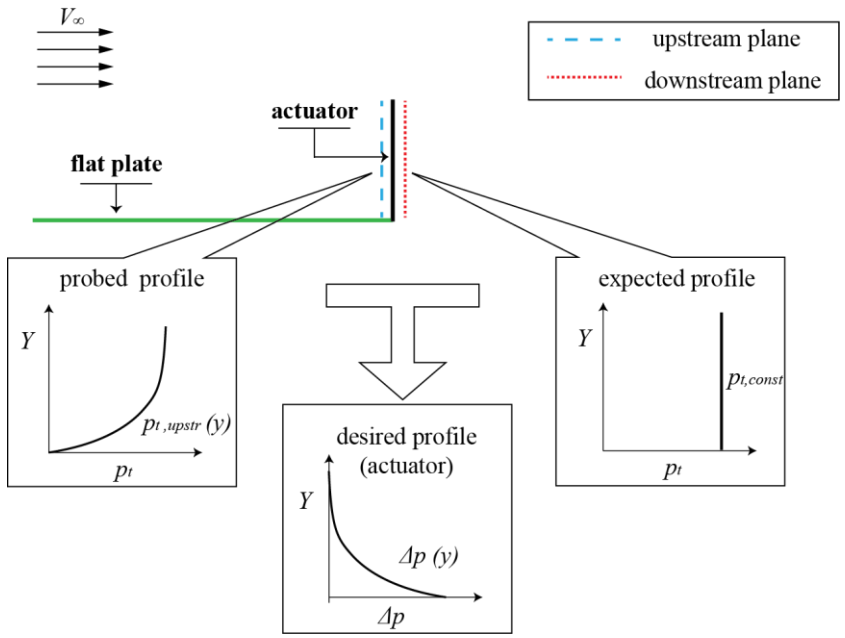

Fig. 4-12. The scheme of a wake filling actuator model

[2] Total pressure is used because the jump of total pressure is identical to the static pressure jump of the actuator disc. This is related to the continuity of velocity through the actuator disc.

The results of the simulation, the flow field around the wake filling actuator disk is shown in Fig. 4-13. The top picture presents the contours of (static) pressure coefficient C_P. A notable phenomenon is that the flat plate is partially immersed in the suction region of the actuator model, creating a negative pressure gradient along the x axis of the plate. This phenomenon supports the body/propulsor interaction discussed earlier in Chapter 3. Another phenomenon is the elliptical contours of C_P, whose centre coincides with the centre of the actuator model. This elliptical pattern is due to the non-uniform distribution of Δp. The bottom drawing of Fig. 4-13 depicts the contours of the coefficient of total pressure C_{Pt}. The laminar contours of C_{Pt} over the flat plate denote the boundary layer. In the region behind the actuator disc, C_{Pt} is uniform with a value slightly greater than 1. This clearly shows that the actuator model fills the total pressure defect of the boundary layer flow. The forces acting on the vehicle can be evaluated. The net force N is obtained by subtracting the drag D from the thrust T, as Eqn. (4.8).

$$N = T - D \tag{4.8}$$

$$T = \oiint_{actuator} \Delta p(y)\, dS \tag{4.9}$$

The viscous drag D (0.0125 N) of the plate is obtained from the simulations. The T (0.0130 N) of the actuator disc is calculated by using Eqn. (4.9). Therefore, the obtained value of N is 0.0005 N.

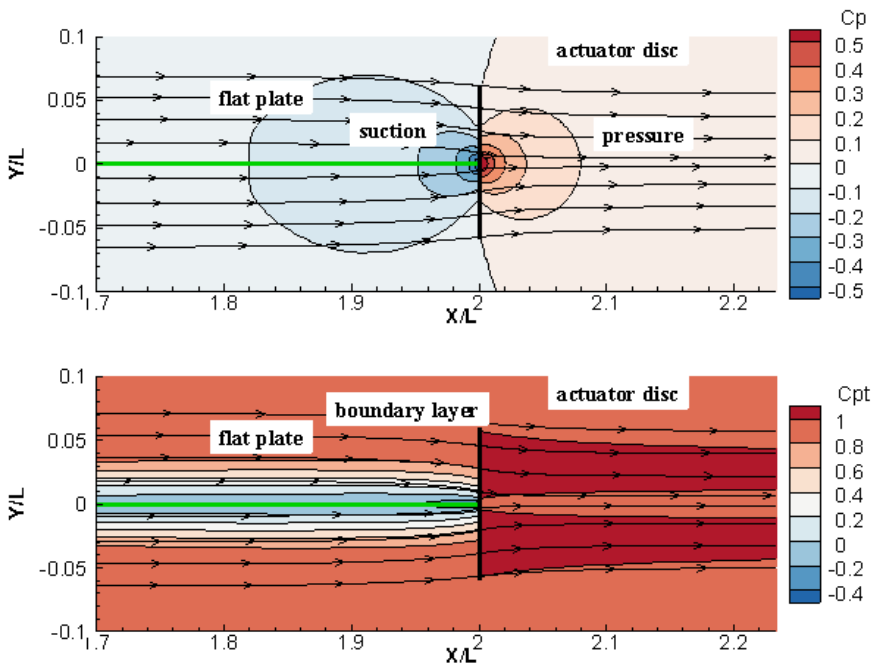

Fig. 4-13. Contours of pressure coefficient (top) and the coefficient of total pressure (bottom) around the wake filling actuator disc, including a mirrored flow field

The *PBM* is used to analyze the power conversion process. The power balance equation for the vehicle is derived in Chapter 3, and given in Eqn. (4.10). The input power of P_K is calculated with Eqn. (4.5), with a value of 0.0936 *W*. The output power of NV_∞ is 0.005 *W* (*N* is 0.0005 *N* and V_∞ is 10m/s). The wake energy flow rate $\dot{E}_w$ and viscous dissipation Φ are evaluated within the computational domain.

$$P_K = NV_\infty + \dot{E}_w + \Phi \tag{4.10}$$

The top drawing in Fig. 4-14 shows the integrand of Φ of the flow field. The high-intensity region corresponds to the boundary layer over the plate. Behind this boundary layer, the low-intensity region is notably different from the body wake of the plate in isolation. The bottom plot of Fig. 4-14 illustrates the change of powers. The input power of P_K (0.0936 *W*) denotes the height of the shaded bar located at the same *x* position of the actuator model. The curves with different colours represent the output powers in Eqn. (4.10). This plot shows that the input power of P_K tends to be equal to (Φ+ $\dot{E}_w$+ NV_∞), with the relative difference of 1.1% as the numerical error of the simulation. The error becomes larger when compared to the case of the isolated actuator disc (0.6%) or the flat plate (0.7%). This increase in numerical error might be caused by the *UDF* function that updates the value of pressure jump in each iteration during computation. This unstable boundary condition defined by *UDF* potentially increases the error.

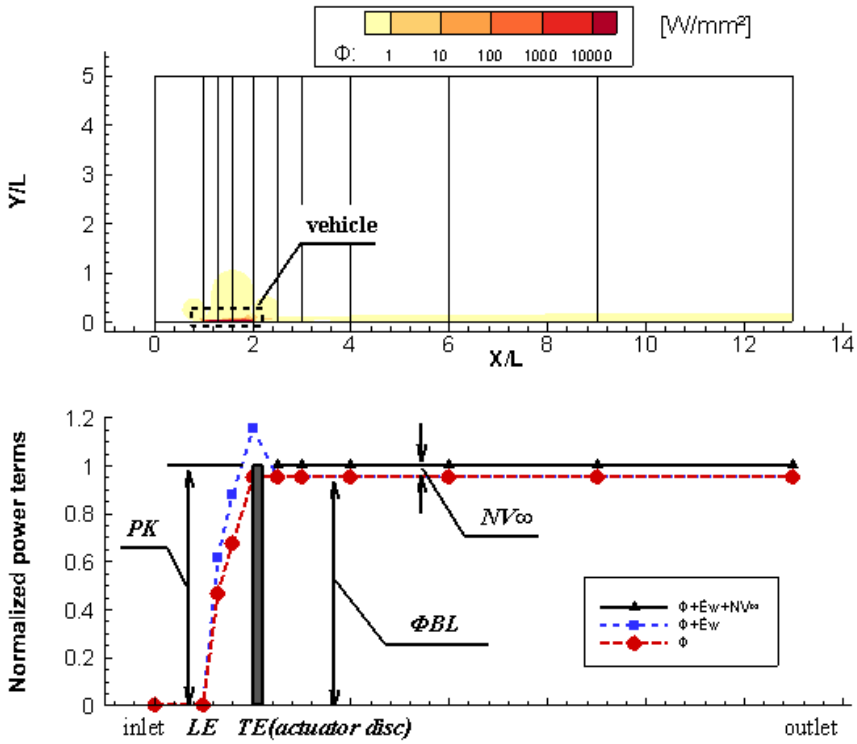

Fig. 4-14. Contours of the integrand of viscous dissipation (top) and the power conversion (bottom) of the integrated vehicle.

The bottom plot in Fig. 4-14 shows the power conversion of the simulated vehicle. The input power P_K primarily becomes the viscous dissipation boundary layer Φ_{BL} and the rest part of P_K turns into NV_∞. In the process of power conversion, $\dot{E}_w$ is clearly a transient power whose value keeps increasing from the *LE* until the *TE* and then abruptly drops to zero at the region behind the *TE*. The prompt drop of $\dot{E}_w$ is caused by the actuator disc model that fills the total pressure defect of the boundary layer. Chapter 3 has elaborated that the $\dot{E}_w$ of the body wake is mainly responsible for the power coefficient η_p being greater than unity. With the simulation results of T and P_K, the value of η_p for the vehicle is 1.38, slightly higher than the value of 1.27 as obtained from the theoretical analysis of the same vehicle. The difference between the two values might be related to the body/propulsor interaction, whose influence could not be evaluated in the theoretical analysis.

4.5 Summary of numerical simulations

The simulation study presented in this chapter shows the typical process of power conversion in a jet wake, a body wake, an actuator disc, a flat plate, and an integrated system. Moreover, this study provides the numerical evidence of the mechanisms involved in *BLI*, namely the power saving mechanism and the body/propulsor interaction. These two mechanisms could change the power and force involved in a vehicle using *BLI*. The influences are discussed by comparing two models of a flat plate and an integrated vehicle that combines the same plate and a wake filling actuator disc. The *CFD* simulations of the two models use identical mesh and the same boundary conditions. **Table 4-3** presents the drag force and key power terms.

Table 4-3. comparison between the isolated flat plate and the integrated vehicle

	Force (N)	Power (W)		
	viscous drag	power input	Φ_{BL}	NV_∞
Isolated plate	0.0106	0.1064	0.0811	0
Integrated vehicle	0.0125	0.0936	0.0878	0.0005
Relative difference	+17.9%	-12.0%	+8.2%	-

The body/propulsor interaction has an impact on the drag force of the flat plate. The value of D for the integrated vehicle is 17.9% higher than that of the isolated plate. This drag increase due to *BLI* is evidenced by the pressure distribution on the plate's surface where a negative pressure gradient along the x direction tends to increase the wall shear stress, as shown in the top of Fig. 4-13.

The power consumption of the integrated vehicle is reduced due to *BLI*. **Table 4-3** shows that the input power (P_K) of the vehicle is 12% lower than that (DV_∞) of the isolated plate. This reduction of power is achieved with a finite value of NV_∞. The

power saving mechanism is supported by the fact that the transient power $\dot{E}_w$ is cancelled behind the actuator disc model. This study also shows that *BLI* increases the boundary layer dissipation Φ_{BL} by 8.2%. This increase might be related to the body/propulsor interaction which causes higher shear stress of the boundary layer.

In this chapter, 2D laminar incompressible Navier-Stokes *CFD* simulations are performed for the models analyzed in Chapter 3, namely a jet wake flow, a body wake flow, an actuator disc model, a flat plate, and an integrated vehicle. The key findings of this research are summarized below:

1. The Power Balance Method can be used to analyse the flow field obtained from numerical simulations using *CFD*.
2. This simulation study demonstrates the typical power conversions, showing the special role of wake energy flow rate in the case of a flat plate and an integrated vehicle.
3. The simulation research supports the theoretical analysis of the mechanisms of *BLI* and evaluates the impacts of *BLI* on power terms and the drag force. In the special case of an integrated vehicle, the power saving mechanism reduces the actual power consumption by 12% as compared to an isolated flat plate. The body/propulsor interaction increases the viscous drag by 17.9% and increases the boundary layer dissipation by 8.2%.

Chapter 5 Experimental study of the flow mechanisms associated with a propulsor ingesting a body wake

This chapter presents an experimental study in order to provide experimental proof of the flow physics as discussed in the theoretical analysis in Chapter 3. More specifically, the current experimental research aims to quantify the power conversion processes involved in a propulsor ingesting body wake. Stereoscopic Particle Image Velocimetry (*PIV*) has been employed for the first time to visualize the flow in wake ingesting propellers. The power balance method is used to quantify the power conversion mechanisms using the data obtained from the experiments. The results prove that the dominant mechanism responsible for the efficiency enhancement is the utilization of body wake energy by the wake ingesting propeller.

5.1 Introduction

In this chapter, an effort is made to study the fundamental power conversion processes involved in *BLI* and *WI* configurations by studying the flow between the body and the propulsor. Wind-tunnel experiments are conducted by employing a propeller ingesting the wake from an axisymmetric aircraft fuselage. Flow fields measurements are acquired with stereoscopic *PIV* [103]. The *PIV* velocity information is used as input in *PBM* to compute the actual power conversion for the propeller. This methodology is meant to overcome some of the misunderstandings in previous experimental studies found in literature, where the incoming energy was assumed to be still proportional to the freestream velocity even in presence of a developed boundary layer.

This chapter is organized into four sections: the first section introduces the background and motivation for this research. Section 5.2 specifies the experimental setup, procedures, and facilities. Section 5.3 presents and elaborates the results and section 5.4 provides the main conclusions.

5.2 Experimental Setup and Procedure

5.2.1 Test configurations

This experimental research investigates three configurations as shown in Fig. 5-1, Free Stream Propulsion (*FSP*), Boundary Layer Ingestion (*BLI*), and Wake Ingestion (*WI*). In the *FSP* configuration, a propeller model is operated in a free stream with uniform inflow conditions, while the drag of the body is evaluated in the absence of a propulsor (Fig. 5-1). In the *BLI* configuration, the propeller is operating just aft of the body. The distance between the propeller and the body is small enough to allow mutual interference of the pressure field of the body with the one of the propeller. In such a configuration, the propeller ingests the boundary layer developed on the surface of the body. In the third configuration, the propeller is mounted downstream of the body, but at a far enough distance such that the body pressure field has recovered to its uniform value. Thus, the main influence of the body on the propeller

in *WI* configuration is due to the body wake impinging on the propeller and not due to the pressure change. In this experiment, *WI* is distinct from *BLI* by the distance between the propeller and the body.

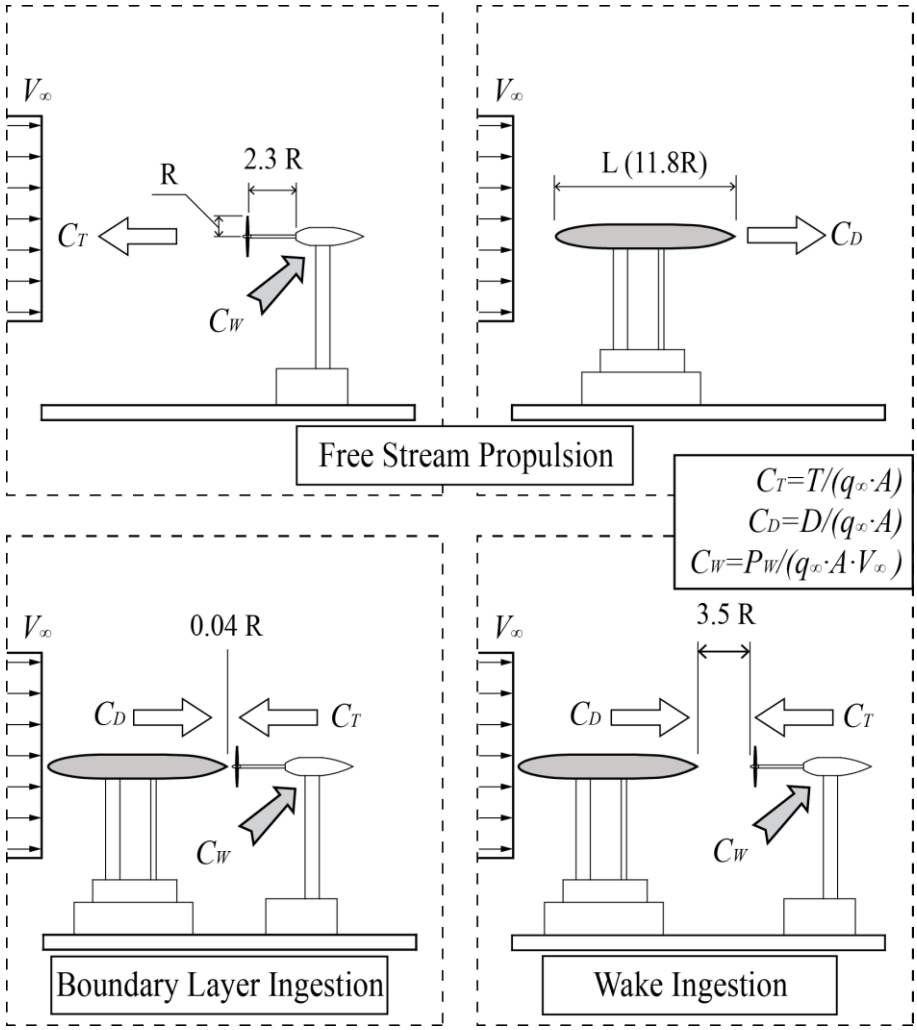

Fig. 5-1. Schematic of various configurations tested in the wind tunnel.

The main features of the experimental setup are as follows:

- Flexible architecture; such that the relative positions of the propeller and body can be easily changed;
- The experiment is focused on the integration effects between the propeller and the body and therefore, the setup excludes the effect of other aircraft components, such as wings and empennages.

- Simple and reproducible, as the chosen body is axisymmetric. As a result, the boundary layer and the body wake are axisymmetric;
- Primarily two measurement techniques have been employed in the present investigation a.) the thrust and torque sensors to measure overall force balance and b.) stereoscopic *PIV* for velocity measurements and flow field visualization.

The specifics of the setup are as follows:

- In the *FSP* configuration, the propeller and body are tested separately in the same airflow condition (see Fig. 5-1);
- The propeller is mounted on a long tube from the pod at a distance of 0.26m (2.3 *R*, *R* is the propeller radius) to minimize any interference effects between the propeller and the pod.
- Experiments are carried out making sure that the drag of the supporting struts is accounted for. The body drag coefficient (C_D), the propeller thrust coefficient (C_T) and the propeller power coefficients (C_W) are measured as a function of the flow Reynolds number and the propeller advance ratio (both based on V_∞).
- During the tests for *WI* and *BLI* configurations, the conditions of the wind tunnel are kept the same as the in the *FSP* configuration.
- In the *BLI* configuration, the propeller is placed coaxially downstream the body at a minimum possible distance of 0.005 m (= 0.04 *R*);
- In the *WI* configuration, the propeller is placed coaxially downstream the body at a distance of 0.4 m = 3.5 *R* in order to avoid any pressure field interference between the body and the propeller (as shown in Fig. 5-1). A pressure survey by using a pitot-static tube was used to determine this distance.

5.2.2 Wind tunnel and experimental models

Experiments have been carried out in the low-speed closed-loop open-jet facility (*OJF*) wind tunnel of Delft University of Technology. The wind tunnel has an octagonal test section with a span and height of 2.85 m and a contraction ratio of 3:1. The airflow is uniform with the turbulent intensity of approximately 0.5% when measured at 1 m downstream of the contraction. A 500 kW electric motor enables a max flow speed of about 32 m/s while a heat exchanger with a cooling capacity of 350 kW keeps the flow temperature constant at 20 ℃. More details and specifications about this facility can be found in Reference [104].

In order to keep the analysis generic and independent of any particular configuration, a body of revolution is used to emulate an aircraft fuselage, with the shape as designed in reference [95]. The body has a cross-sectional area of 0.0201 m ²with a length of 1.35 m. Due to the relatively small size of the model with

respect to the test section (area ratio 0.22%), the wind tunnel blockage corrections are not required [105]. Experiments are performed at a constant airflow speed (V_∞) of 26 m/s, with an L-based Reynolds number of 2.3 million. The boundary layer over the body is forced to transition at 0.2 L by a 60 °zig-zag 3D-turbulator tape (0.2 mm thickness and 6 mm point-to-point distance). This body is connected to a balance which measures the axial force.

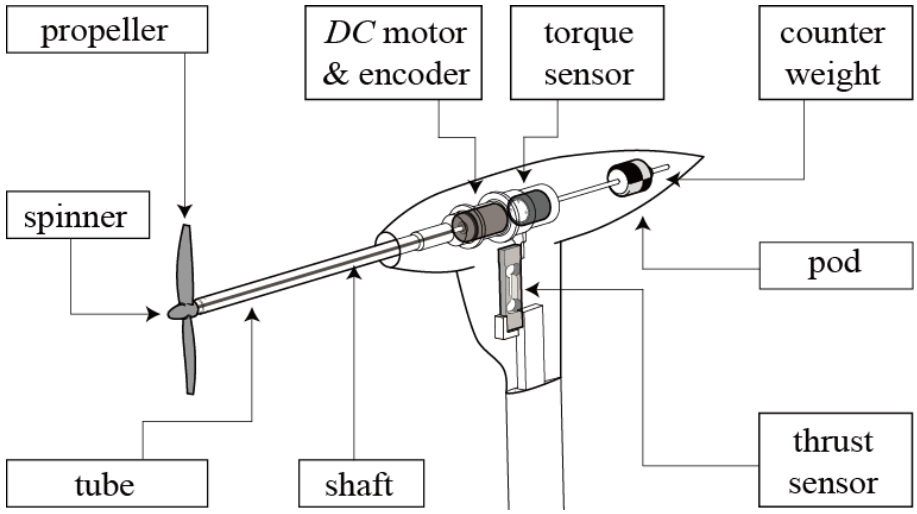

Fig. 5-2. Schematic of the propeller unit with the installed motor and embedded sensors.

The design of the propeller unit is shown in Fig. 5-2. A Maxon© *RE*40 DC motor drives an *APC*© 9×10 (0.114 m in radius *R*, 0.254 m in pitch) propeller. A *GW INSTEK*© *PSP*-405 power-supply provides a maximum output of 40 V and 5 A. The thrust T is measured through a *PCM*© *SP*-1004 load cell with a maximum load of 5.88 N (0.6 kg). The shaft power is obtained as the product of the propeller rotational speed n with the reaction torque Q, both measured by a Maxon© *MR* type digital encoder and a Transducer Techniques© *RTS*-25 torque sensor (range of ±0.176 Nm). The propeller is mounted on a long shaft to reduce the propeller/pod interference and still allowing for an easy optical access for *PIV* measurements. The pod is designed with an open nose (such that the pressure inside the pod equals to the total pressure of free stream) in order to cancel any balancing issues created due to the dynamic pressure force over the spinner.

5.2.3 Stereoscopic *PIV* measurement setup

The stereoscopic *PIV* technique is used to measure the flow field around the propeller. The schematic of the *PIV* setup is illustrated in Fig. 5-3 (a). Two LaVision© Imagers Pro LX camera with 16 Mpix resolution (4870×3246 px^2, 7.4

μm/px pixel pitch) and equipped with two Nikon© lenses (focal length *f*=105 mm and an aperture of *f#*=4) are used. The cameras are positioned at a distance of about 0.8 m from the target with a relative stereoscopic angle of 77°. The final *FOV* obtained is of about 280×180 mm^2, with a digital resolution of 14.7 px/mm. With the magnification of about 0.13 and an aperture of *f#*=4, the expected particle size on the sensor is around 0.9 px [106]. In order to mitigate the peak-locking effect, the particle size is increased to about 1.5 px by shifting the relative distance of the focus plane with respect to the laser plane [103]. A Quantel Evergreen© Nd: YAG laser system (output 200 mJ/pulse) is employed with laser optics to form a 2.5 mm thick laser sheet on a surface of about 300×200 mm^2. A SAFEX© smoke generator is used to produce seeding particles. A series of 700 uncorrelated vector fields are measured per test case. Acquisition and processing of the particle images are carried out with LaVision© Davis 8.1.4 software. The ensemble of mean velocity and fluctuations are obtained by averaging the 700 uncorrelated vector fields. Table 5-1 summarizes the system parameters of the stereoscopic *PIV* measurement system.

Table 5-1. System parameters of the stereoscopic *PIV*.

PIV parameters	***Measured values***
FOV (*X*×*Y*)	280×180 mm^2 (4870×3246 px^2)
Digital resolution	14.7 px/mm
Magnification factor	0.13
Number of samples	700
Interrogation size	16 × 16 px, 50% overlap
Vector resolution and spacing	0.91 mm, 0.46 mm

The 2D field vector fields are acquired in the propeller mid-plane. The velocity fields are used as input for the *PBM*. The *PBM* requires a velocity of the flow field encompassing propeller and body units. Such information is made available by assuming axisymmetric flow in the present campaign. A 3D control volume (*CV*) is thus generated by revolving the 2D stereoscopic vector fields along the propeller axis. Such a *CV* has the propeller surface defining the inner boundary of the *CV*. The external boundaries of the *CV* are the inlet plane, the outlet plane, and the outer stream tube.

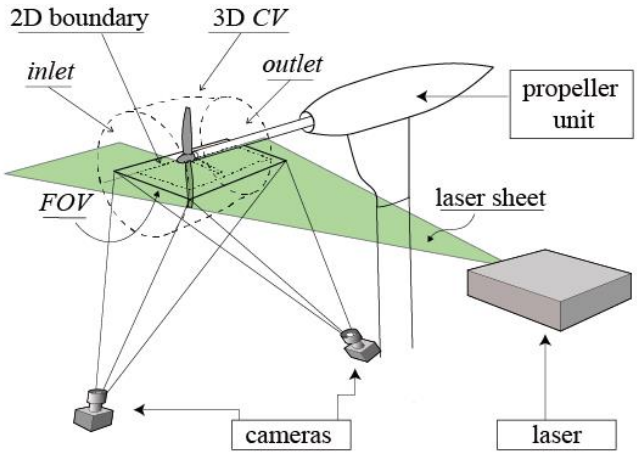

(a) Schematic of Stereoscopic ***PIV*** setup

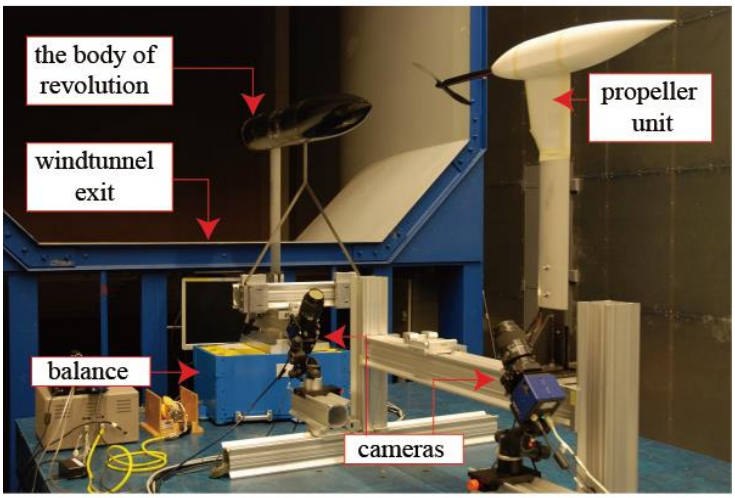

(b) Experiment setup (***WI*** configuration)

Fig. 5-3. The Stereoscopic Particle Image Velocimetry setup, showing the propeller unit and the body of revolution in the *TU* Delft *OJF* wind tunnel.

5.2.4 Pressure measurements using the Pitot-static tube

A Pitot-static tube is employed to obtain information about the pressure field in the wake of the body. Vertical profiles of static and total pressure measurements are obtained by positioning the pitot-static tube on a 2-axis traversing system and by scanning the body wake at different downstream locations. The total and static pressures are therefore measured as depicted in Fig. 5-4. The obtained profiles are used to define the relative distance between the propeller and the body unit in the *WI* configuration. The distance between the propeller and the body is adjusted to a value of 3.5 R (residual pressure coefficient C_P of 0.025). The pressure measurements are

also employed as reference values for the *PIV*-based flow field analysis described later.

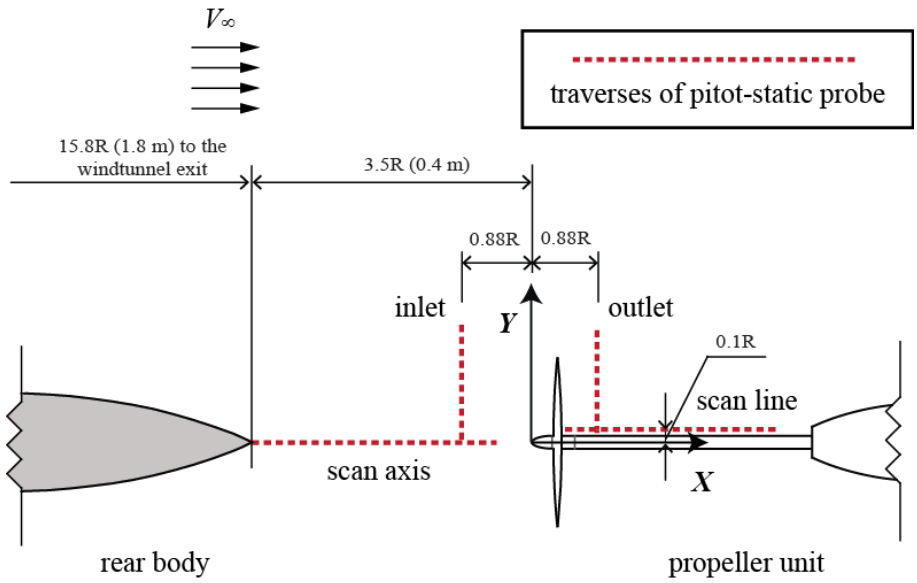

Fig. 5-4. The traverse of pressure measurements for the Wake Ingestion configuration. The spacing of the scan points is 10 *mm*.

5.2.5 Measurement Uncertainties

The uncertainties of the sensors are obtained from the specifications provided by the manufacturers and from calibration data. The instrument uncertainties for the measured quantities are listed in Table 5-2. These uncertainties are then used as input to calculate the uncertainties obtained in derived quantities using linear error propagation [107].

Table 5-2. Instrument uncertainties and the estimated uncertainties.

Measured parameter (instrument)	***Uncertainty σ***
q_∞ (wind tunnel pressure gauge)	0.314 Pascal
D (balance)	0.008 N
T (thrust sensor)	0.011 N
Q (torque sensor)	0.0009 Nm
Coefficients	***Uncertainty σ***
C_D	0.009
C_T	0.001
C_W	0.003

Most relevant uncertainties in the *PIV* measurement are due to the peak-locking and lack of spatial resolution. In the images with the seeding particles occupying approximately 2 *px*, the maximum deviation of 0.05 *px* is reported from the perfectly sampled distribution [103]. As for the stereoscopic *PIV* measurement, the system errors due to the calibration plane alignment and lens distortion are corrected by the self-calibration procedure of the Davis software, giving a residual of 0.53 *px* for calibrations [108]. According to a previous study [109], the vector resolution (0.56 *mm*) of this *PIV* setup determines the uncertainty in velocity of approximately 0.1%. The *PBM* based flow field analysis uses the velocity field as an input to compute all the forces and power contributions. Since the *PBM* is based upon conservation of kinetic energy and conservation of momentum, all forces, and power contributions should be independent of the chosen integration path. In this respect, the scatter on the values obtained from varying the boundaries of integration and the *CV* is used as an estimation of the effect of the experimental uncertainties.

5.3 Experimental Results and Analysis

5.3.1 Results of the sensor measurement

This subsection discusses the results of the tested configurations, with a focus on the comparison between the body/propeller combination and the isolated propeller. In order to quantify the effective power conversion for the *WI* configuration, the *PBM* [33] is employed in a control volume encompassing the flow field around the propeller (Fig. 5-5). The power balance equation, Eqn. (5.1) is used to quantify the various powers involved in for a propeller ingesting wake[110]. In this equation, the propeller shaft power (P_W) is a power input, while the TV_∞ is a power output. Furthermore, $\dot{E}_{w,in}$ denotes the power within the body wake (which also acts as a power input corresponding to the wake energy inflow entering the *CV)* and $\dot{E}_{w,out}$ represents the power within the downstream wake of the propeller (this is a wake energy outflow leaving the *CV)*. The last term Φ_{CV} represents viscous dissipation, due to the viscous loss within *CV*. The integral expressions of all the power terms are provided in Appendix A. The Eqn. (5.1) proposed here is quite effective because it allows treatment of more complex aircraft engine configurations (where the incoming velocity at the propeller inlet plane is not uniform) and the conventional configuration.

$$\dot{E}_{w,in} + P_W = TV_\infty + \dot{E}_{w,out} + \Phi_{CV} \tag{5.1}$$

By analyzing the power conversion described in Eqn. (5.1), two mechanisms responsible for the reduction of the shaft power P_W (for a given TV_∞ output) can be identified. For the *WI* (and also *BLI*), the first mechanism utilizes the $\dot{E}_{w,in}$ as a power input for the propeller. The second is the reduction of the power sink of $\dot{E}_{w,out}$. The ingestion of a body wake brings in a momentum deficit to the upstream flow. As a result, the given thrust force (T) can be produced with a lower momentum excess of the downstream flow, leading to a reduction in $\dot{E}_{w,out}$ of the flow behind the propeller. It is noted that reducing viscous dissipation Φ_{CV} could also lead to a

saving of P_W, but it is unclear whether *WI* (and BLI) could save vicious dissipation of the propeller, and therefore this aspect is not discussed further. The two aforementioned mechanisms theoretically support the results of experiments shown in Fig. 5-6 and 5-7. Nevertheless, due to the inability to measure $\dot{E}_{w,in}$, $\dot{E}_{w,out}$, and Φ_{CV}, there is still a lack of evidence to justify the power conversion mechanism provided in Eqn. (5.1).

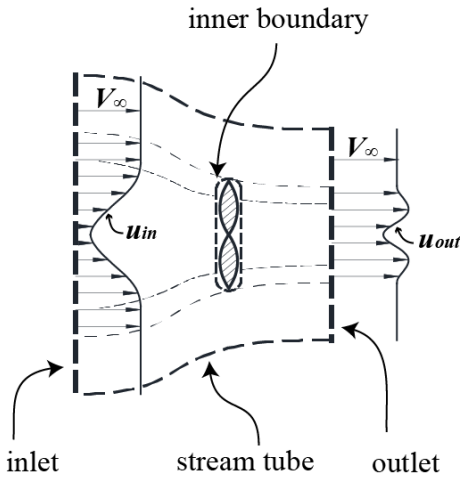

Fig. 5-5. Control volume of a propeller in the Wake Ingestion configuration.

For the body/propeller combination, C_N-C_W results are plotted in Fig. 5-6. Note that the net force (N) and the power (P_W) are unambiguously defined for aircraft models with engine simulators in many wind tunnel tests. In this research, the difference between C_T of the propeller and the C_D of the body of revolution denotes the coefficient of net force ($C_N = C_T$-C_D, the cross-sectional area of the body, A, is chosen as the reference area). For the subsystem of the propeller, the commonly used J-η_P plots are chosen. For the power coefficient η_P (= C_T/C_W), based on the free stream velocity, the same definition is used for all configurations.

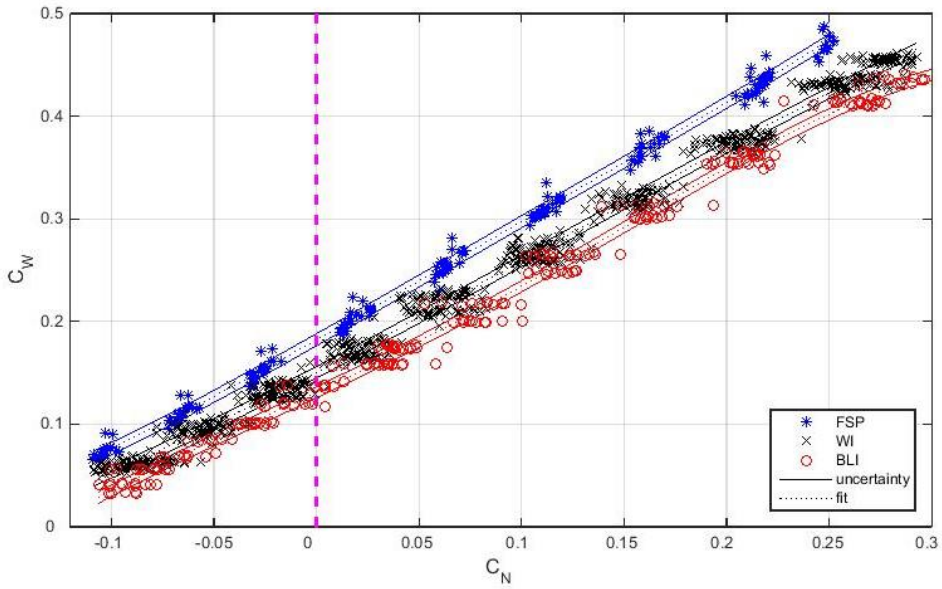

Fig. 5-6 Results for the body/propeller combination (C_N versus C_W) in the three configurations. Dotted lines represent the fitted curves of polynomial regression; the uncertainty lines denote the 2σ envelope (95% confidence interval).

Figure 5-6 presents the results of the body & propeller combination depicted by 200 measurement points for all three configurations. Each point is measured in a steady-state condition for around 30 seconds with a data sampling frequency of 50 Hz. The graph shows that the shaft power consumption in *WI* and *BLI* is lower than that for *FSP* at a given net force. The condition of $C_N = 0$ (dashed vertical line) corresponds to an equilibrium between the body and the propeller. In this condition, the power saving due to *WI* is approximately 10%±1.4% with respect to *FSP*, and the saving due to *BLI* is approximately 18%±1.4%. These results are in accordance with some of the experiments on *BLI* reported in the literature [77, 78].

Figure 5-7 shows the propeller J-η_P characteristics for the three configurations. In Fig. 5-7 (a), the propeller efficiency and J are calculated using the ambient velocity V_∞. As can be seen, the propeller in *WI* and *BLI* configuration exhibits higher efficiency for a given J, when compared to the baseline *FSP*. However, the increase in propeller performance is not only caused by the use of V_∞, which in fact is not a correct representation of the inflow condition for a propeller in *WI* and *BLI* configuration, as the incoming wake flow to the propeller is non-uniform with velocity magnitude lower than V_∞. In order to give a different picture, Fig. 5-7 (b) represents the propeller J-η_P characteristics using the average inlet velocity profile in

the wake behind the body just before the propeller[3]. Thus, it can be inferred from Fig. 5-7 that the improvement in the propeller J-η_P characteristics, when used in the *WI* and *BLI* configuration, is not just due to the reduction in inlet velocity.

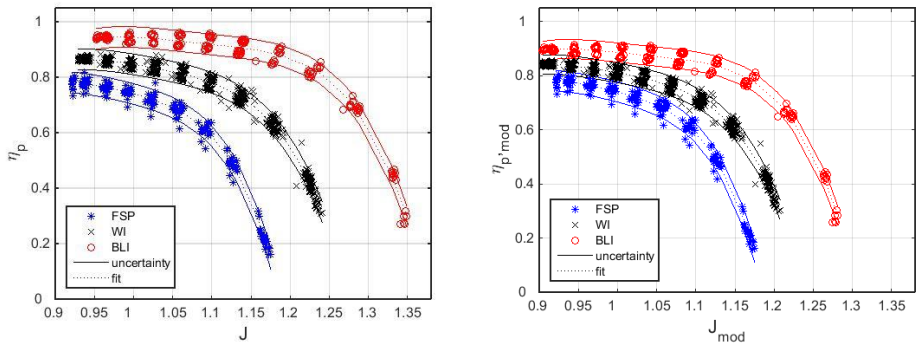

(a) (b)

Fig. 5-7. Propeller characteristics (J-η_p) in the three configurations with (a) based on V∞ and (b) based on average propeller inlet velocity.

5.3.2 *PIV*-based flow field analysis

This subsection aims at measuring the actual power conversion process within the *WI* configuration by employing the stereoscopic *PIV* technique. In order to compute all power terms in Eqn. (5.1), the results pertaining to the force balance measurements and velocity measurements obtained from *PIV* have to be combined in the integral formulation given in Appendix A.

Previous studies have shown that the *PIV* technique can be employed to determine integral forces on airfoils and propeller blades [111-114]. The *PIV* velocity measurements together with numerical simulation can be used to quantify integral powers [38, 48, 77]. In this research, the *PIV*-based pressure reconstruction and load determination are used to quantify the integral powers [111-114]. The workflow of the *PIV*-based flow field analysis is presented in Fig. 5-8. The discussion is briefly organized into three parts: the first part elaborates how to incorporate the velocity field obtained from the *PIV* measurements into the power balance method; the second part introduces computation of pressure from the velocity field, and the third part discusses the evaluation of the integral powers and forces.

[3] An mass-averaged velocity ($V_{mod} = \frac{\int_{SP} u dS}{\int_{SP} dS}$) is used to modify parameters in which $V_{\infty,}$ is replaced by V_{mod}. The modified parameters are: $J_{mod} = \frac{V_{mod}}{n\pi R}$ and $\eta_{p,mod} = \frac{T \times V_{mod}}{P_w}$;

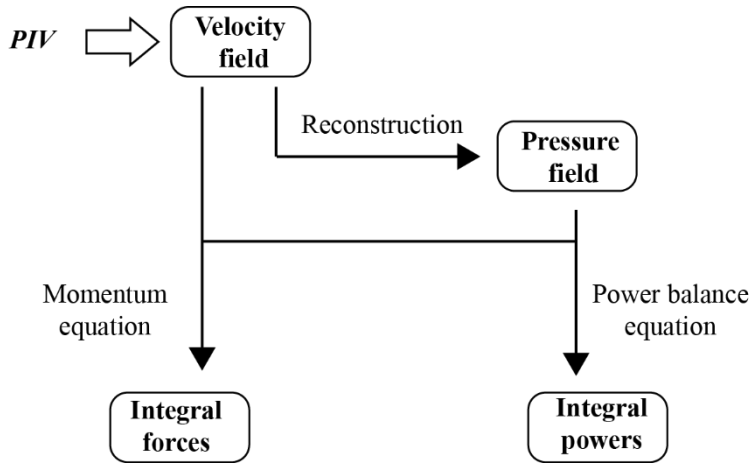

Fig. 5-8. Workflow of the *PIV*-based flow field analysis.

The *PIV*-based flow field analysis is performed for the propeller in two configurations, *FSP*, and *WI*. The comparison between them makes it possible to identify and investigate the flow mechanisms for a propeller ingesting body wake. The *PIV*-based analysis is carried out at a specific equilibrium condition of the body & propeller combination ($T \approx D$). Some of the assumptions made in carrying out the *PIV*-based flow field analysis are:

- A moving frame of reference is employed with the body and the propeller thought to be moving at V_∞.
- The flow is assumed to be axisymmetric. This is verified with the mean velocity fields to build the 3D control volume.
- The analysis is carried out on the mean fields, as obtained from averaging of a converged dataset of uncorrelated samples.
- In the *PIV* based flow field analysis, the interferences of the propeller spinner and the supporting tube are neglected in the calculation of propeller thrust and shaft power.

iii. Stereoscopic PIV measurement

For each configuration, the stereoscopic *PIV* measurement system acquires 700 pairs of images at a random azimuthal angle of the propeller. The image pairs are then correlated by a multi-pass algorithm [115] to obtain single vector fields statistically processed into their average velocities and Reynolds stresses [104]. Figure 5-9 shows the normalized convergence of (a) averaged velocity and (b) Reynolds stress. It shows that around 400 samples can ensure the statistical convergence for the field in the *WI* configuration, except for the out-of-plane component (*w* component), which has a higher relative uncertainty.

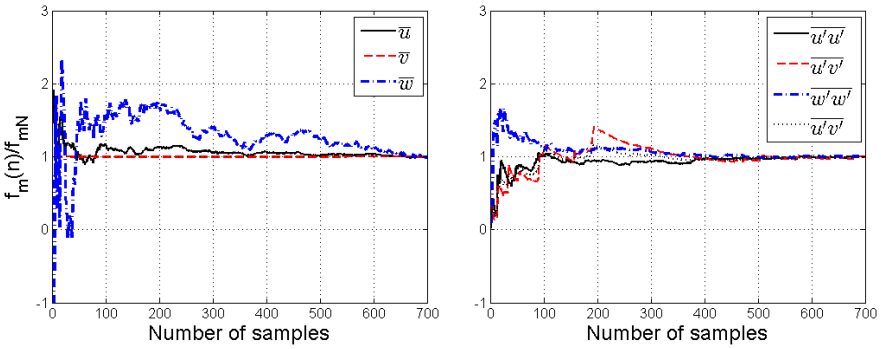

(a) (b)

Fig. 5-9. Convergence of statistically averaged (a) velocity and (b) Reynolds stress. The parameter f_m denotes the average of the quantity in a sample area within the body wake for the WI configuration (the sample area is 10 ×10mm ²in size and located at 0.5R in front of the propeller spinner).

Figure 5-10 shows the results pertaining to the flow field around the propeller in the *FSP* configuration, as denoted by the contours of normalized velocity magnitude (Fig. 5-10 (a)) and contours of turbulence intensity (Fig. 5-10 (b)). This flow field outlines the propeller shape with the origin of the coordinate set located at the spinner nose. The contours in Fig. 5-10 highlight several features in the flow field.

- Close to the spinner, the velocity contours show the boundary layer, which also corresponds to high-level Turbulence Intensity (*TI*) (above 30%).
- The velocity increases across the propeller can be observed. The moderate increase in the velocity is due to the low thrust required at the equilibrium condition ($T \approx D$).
- In the region close to the propeller blade root (0.1~0.3 y/R), a high-level of *TI* (above 30%) is measured on both sides of the propeller. The behaviour is further analyzed in the subsequent section.
- The relatively higher value of *TI* is measured close to the tip, at a radial position of 0.8~0.9 y/R,
- At the tip of the propeller blade, there is a band-shaped region characterized by low-level of *TI* (around 3%). This might be due to the lower blade loading associated with the development of the propeller tip vortex (e.g. [104, 112, 113]).

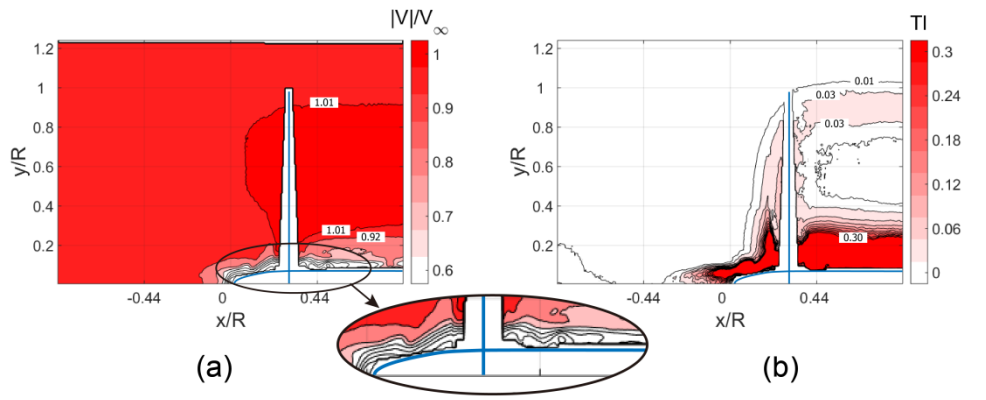

Fig. 5-10. Normalized contours (at the plane of z=0) for the propeller in the FSP configuration (a) velocity magnitude and (b) turbulent intensity.

The flow field around the propeller in the *WI* configuration is shown in Fig. 5-11. The main difference as compared to the flow field for the *FSP* is the presence of the body wake upstream of the propeller. The contours of velocity and *TI* show that the radius of the body wake is about 0.4 *R*. The flow field shows that the propeller ingests both the body wake and the free stream flow. The contours show similar features associated with the boundary layer over the spinner and the possible separation near the blade tip. The high-level of *TI* (above 30%) is also present on both sides of the blade root (0.1~0.3 *y/R*). This indicates a possible flow separation near the blade root. It should be noted that *TI* indicates the magnitude of Reynolds stress, which is used to compute viscous dissipation.

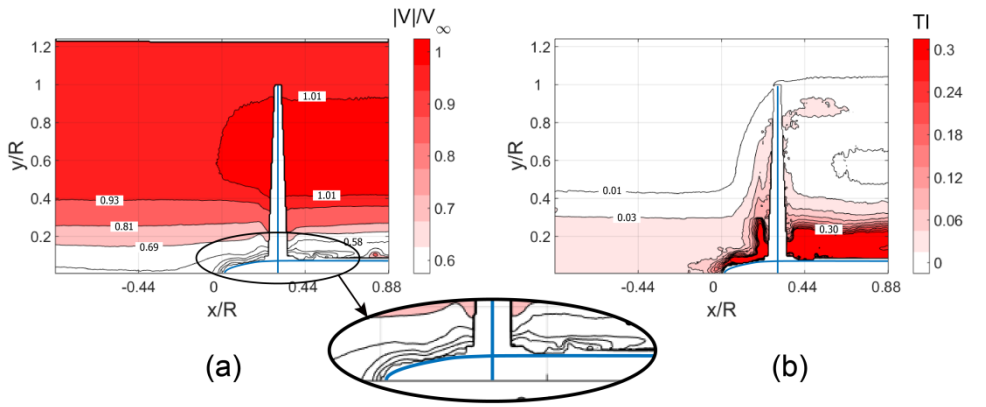

Fig. 5-11. Normalized contours (at the plane of z=0) for the propeller in the Wake Ingestion configuration (a) velocity magnitude and (b) turbulent intensity.

As introduced in the experimental section, the pressure measurements using the Pitot-static tube are acquired for the *WI* configuration. Dynamic pressure profiles from the Pitot-tube are measured upstream at the propeller inlet (-0.88 *x/R*) and downstream outlet (0.88 *x/R*) positions and transformed into velocity profiles. The results are subsequently compared with that of the *PIV* measurement. The velocity

profile from the two measurement techniques at the inlet and outlet plane is presented in Fig. 5-12. It can be seen that the two measurements are in good agreement with each other. The physical interference restricts the position of the Pitot-static tube when approaching the tube wall. The closest measurable region for *PIV* is also limited to around 0.15 *y/R* due to light reflection and finite spatial resolution near the wall and severely restrict the reliability of velocity vectors.

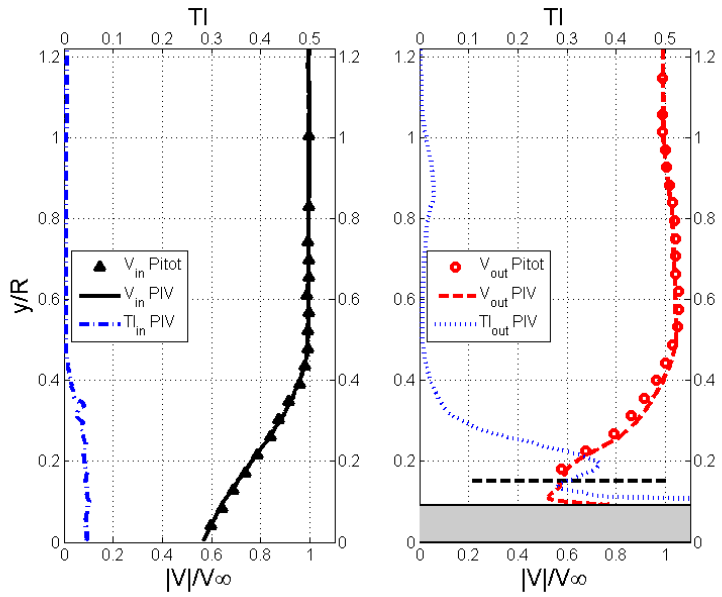

(a) (b)

Fig. 5-12. Profiles of normalized velocity magnitude and turbulent intensity in the Wake Ingestion configuration (a) at the inlet plane and (b) at the outlet plane. The region shaded in gray at the bottom of (b) represents the propeller tube, and the thick dashed line indicates the lower limit for PIV measurements.

iv. Pressure field reconstruction

The static pressure measurement using the Pitot tube indicates the impact of pressure on the forces to be measured. In the *WI* configuration, a small but finite pressure difference is measured between the inlet and outlet (Fig. 5-13). Such a value of approximately 5 *Pa* between the two planes (C_P < 0.025 at the inlet; C_P < 0.045 at the outlet) indicates the contribution of pressure force (to approximately 0.3*N*) in the control volume, constituting about 25% of the total measured thrust (1.26 *N*).

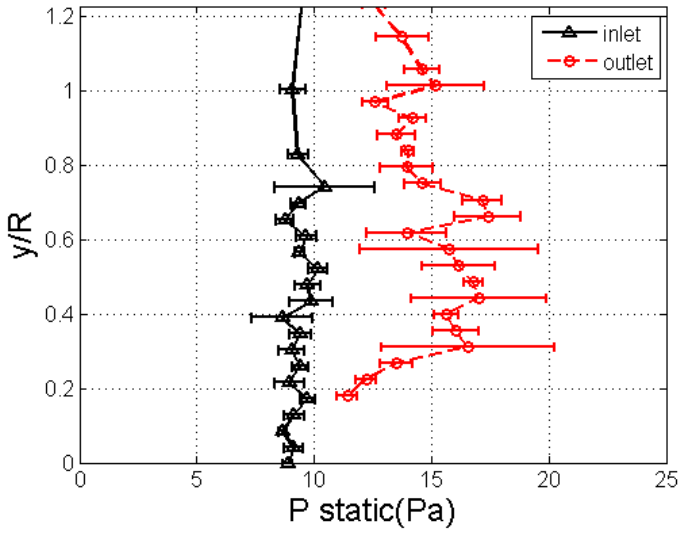

Fig. 5-13. Static pressure (measured by the Pitot-static tube) at the inlet and outlet in the Wake Ingestion configuration. Error bars denote the standard deviations of the samples.

In order to account for the contribution of pressure in the entire flow field, the *PIV*-based flow field analysis is employed to reconstruct pressure from the velocity fields [116]. The pressure gradient is derived from the Navier-Stokes momentum equation, and the pressure is subsequently integrated by solving the pressure Poisson equation as given in Eqn. (5.2). Isentropic pressure (Dirichlet) and pressure gradient (Neumann) are used as boundary conditions in the flow domain [111-113]. The former is applied for the boundary where the pressure measurement data is obtained from the isentropic process and the latter uses the data of pressure gradient for the rest of the boundary.

$$\frac{\partial^2 P}{\partial x^2}+\frac{\partial^2 P}{\partial y^2}=-\rho\left\{\left(\frac{\partial u}{\partial x}\right)^2+2\frac{\partial v}{\partial x}\frac{\partial u}{\partial y}+\left(\frac{\partial v}{\partial y}\right)^2\right\} \tag{5.2}$$

Contours of pressure coefficient are shown in **Fig. 5-14** for the two configurations. The high pressure at the propeller spinner corresponds to the stagnation flow. As can be seen, the contours identify the negative pressure upstream of the propeller blade and the positive pressure downstream the blade, thus denoting the circumferentially averaged pressure close to the suction and pressure sides of the propeller blade. The small negative pressure regions behind the blade root (0.1~0.3 *y/R*) indicates a possible flow separation as discussed previously. It can be seen that in the *FSP* configuration, the change in the pressure across the propeller is higher (0.3~0.8 *y/R*).

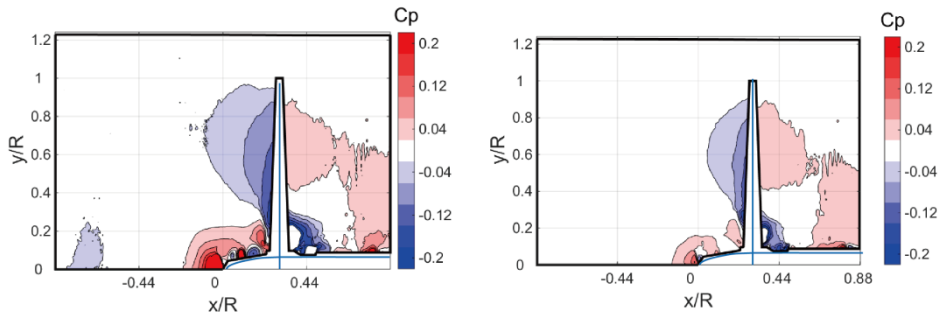

(a) (b)

Fig. 5-14 Fields (at the plane of z=0) of pressure coefficient around the propeller as obtained from the pressure reconstruction for (a) Free Stream Propulsion configuration and (b) Wake ingestion configuration.

v. Integral forces and powers in the flow field

The velocity field and reconstructed pressure are used to evaluate the integral forces and powers. The change in integral forces represents the thrust of the propeller, and the change in integral powers denotes the power conversion for the propeller. To analyze the changes in forces and powers, their values in the flow field at different axial locations have to be evaluated. The approach and the required equations are elaborated in Appendix A.

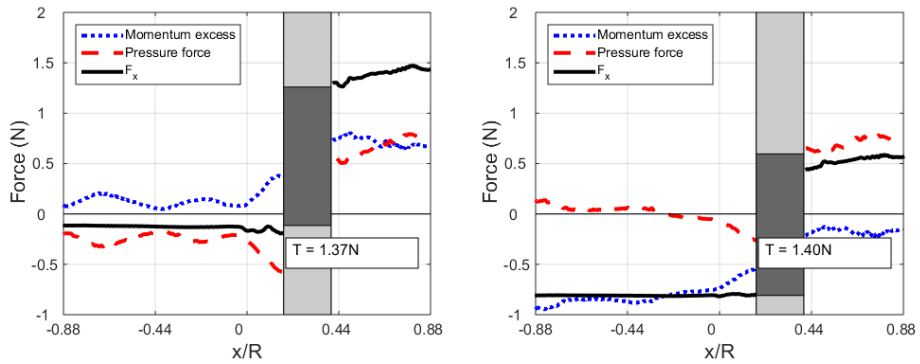

(a) (b)

Fig. 5-15. Forces in the flow field (a) Free Stream Propulsion and (b) Wake Ingestion (The light gray part of the bar indicates the location of the propeller, and the height of the dark gray part of the bar corresponds to the assessed thrust).

The integral forces pertain to the integral form of the momentum equation. This analysis classifies them as momentum excess (change), pressure force, and axial force F_x. The plot in Fig. 5-15 represents these forces for the *FSP* and the *WI*

configuration. The curves are obtained by evaluation of the integral forces at different axial locations within the flow field. The momentum change and the pressure force integrals are constant at axial locations (x) in a range of -0.88~0.2 x/R. Due to the absence of any localized source or sink, the axial force remains constant in front of the propeller. The value F_x is $0.13 \pm 0.02N$ for the *FSP* and $-0.81 \pm 0.01N$ for the *WI* configuration. It should be noted that the absolute value of the F_x does not equal the body drag measured by the balance ($1.2 \pm 0.1N$). The difference is attributed to the small cross-sectional area of the *CV* as compared to that of the body. A contour variability analysis shows that this difference increased when the size of the *CV* was reduced. The F_x is subjected to a sudden jump at the propeller location. In the axial range of 0.4~0.88 x/R (downstream the propeller), the curves still show a rather small increase in F_x, slowly converging to a specific value. This is due to the limited spatial resolution of the *PIV*.

From the two plots in Fig. 5-15, it can be seen that the curves for momentum excess vary along the field. The pressure force shows a jump at the location of the propeller (0.2~0.3 x/R). The analysis additionally evaluates the propeller thrust T (the equation is provided in Appendix A), whose value is obtained as the limit of the force balance for a relative distance shrinking to the propeller disk. In the limit, the propeller thrust T is equal to the change of F_x along the propeller disk. The mismatch between T and the change of F_x can be attributed to a tiny imbalance error in the calculation of mass flow rate within the *CV* [114], discussed in the following paragraph.

Table 5-3. Results of integral powers at the inlet and outlet planes.

		inlet	outlet
FSP	Φ	0	0.6
	$\dot{E}_w$	0	2.2
	TV_∞	0	35.7
	P_W	40.8	
WI	Φ	0	0.2
	$\dot{E}_w$	1.8	2.8
	TV_∞	0	36.5
	P_W	37.4	

In the *PIV*-based flow field analysis, the integral powers are: viscous dissipation (Φ), wake energy flow rate ($\dot{E}_w$), thrust power (TV_∞), and shaft power (P_W). Table 5-3 presents the values of these powers at the inlet and outlet planes. The power conversions are presented in Fig. 5-16. In accordance with Eqn. (5.1), the curves correspond to different summations of powers; in the figure, the blue curve for viscous dissipation (Φ) which keeps increasing along the axis. The value is rather small compared to other powers, showing the small impact of the flow features highlighted by the contours of *TI*. However, it should be noted that the dissipation of

the boundary layer over the propeller blade (blade profile loss) is not included due to the experimental limitations. The gap between the red and blue curves denotes wake energy flow rate $\dot{E}_w$. It can be seen from Fig. 16 that in the *FPS* configuration, this power is present only downstream of the propeller, whereas in the *WI* configuration, $\dot{E}_w$ is present both in the upstream and downstream of the propeller. The power of TV_∞ depends on the thrust *T*, which has been discussed as an integral force. The TV_∞ is represented by the gap between red and black curves behind the propeller. Note that the black curve denotes total power ($\Phi + \dot{E}_w + TV_\infty$). The analysis alternatively evaluates shaft power P_W as the change of mechanical power of the entire *CV*, as represented by the height of the dark grey bar shaded in Fig. 5-16. This indicates that the mechanical power is added to the flow field in the region close to the propeller plane.

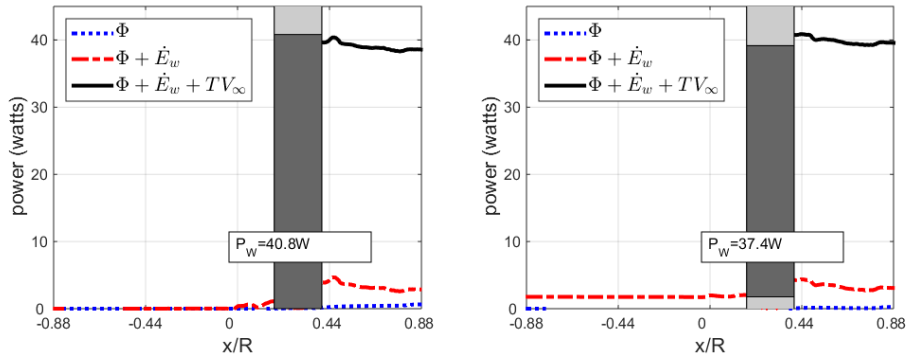

Fig. 5-16. Power conversions for the propeller (a) Free Stream Propulsion and (b) Wake Ingestion (The part of the bar shaded in light grey marks the region of the propeller blade while the height of the bar shaded in dark grey corresponds to the assessed propeller shaft power).

The two plots in Fig. 5-16 illustrate the different power conversion processes. As discussed in the power balance equation, two mechanisms reduce the shaft power consumption of the propeller when ingesting body wake. The first one is the utilization of the body wake as input power. This mechanism is clearly evidenced by the term $\dot{E}_w$ calculated upstream the propeller, denoted by the $\dot{E}_{w,in}$ in the power balance Eqn. (5.1). $\dot{E}_{w,in}$ is 1.80±0.08 *W* for the *WI* and zero for the *FSP* configuration. The second mechanism is the reduction in the power sink (output) of the downstream wake, denoted by $\dot{E}_{w,out}$ in Eqn. (5.1). However, this mechanism is not supported by experimental observations. Instead, it was observed that $\dot{E}_w$ behind the propeller is 3.2±0.5 *W* for the *WI* configuration and 2.9±0.6 *W* for the *FSP*. As a result, it is difficult to prove the second mechanism from the experimental observations. It is possible for the propeller to increase the downstream wake in this experiment because a conventional propeller is designed to work in the free stream condition, rather than to fill the downstream wake.

The contour variability analysis is carried out for the *PIV*-based flow field by varying the location of the integral computation by changing the geometry of the entire *CV* [111, 114]. The volume is modified by shifting the inlet and outlet planes towards the propeller, between -0.88~-0.44 *x/R* and -0.44~0.88 *x/R* respectively. This approach is meant to estimate the variability of the computed thrust (T) and shaft power (P_W) within the domain of integration. On the other hand, further information on the uncertainty can be obtained by analyzing the mass flow rate through the cross sections in the range -0.88~0.88 *x/R*. The relative standard deviations of 0.3% and 0.2% denote the uncertainties of the *PIV* derived mass flow in the cases of *WI* and *FSP* respectively. A previous study [114] shows that the uncertainty of mass flow plays a major role in the calculation of uncertainty in integral force. This correlation is denoted by the mismatch between thrust T and the change of F_x. The integrands of these two forces are primarily distinguished by the term of $\rho u V_\infty$, as given in Appendix A. Similarly, the uncertainty in mass explains the mismatch between the shaft power P_W and the change of the total flow power ($\Phi + \dot{E}_w + TV_\infty$). The mismatch is approximately 5.6% for *FSP* and -0.8% for the *WI* configuration.

5.3.3 Comparison and Discussion

This subsection compares the results of the two experimental techniques, *PIV* and force balance measurements. It is noted that the embedded force sensors measure about 500 sets of uncorrelated data simultaneously during the *PIV* acquisition. The settings of the wind tunnel and propeller unit were kept unchanged, maintaining a condition where the net force N of the body/propeller combination is about 0.05~0.2 N for both configurations.

Table 5-4. Results of the sensor measurement and the PIV-based flow field analysis.

	T (N)	P_W (W)
FSP sensor	1.23 ±0.01	44.9 ±0.4
WI sensor	1.26 ±0.02	40.6 ±0.5
FSP PIV	1.37 ±0.04	40.8 ±0.5
WI PIV	1.40 ±0.04	37.4 ±0.5

Table 5-4 presents a matrix showing the results of the force sensor measurement and that of the *PIV*-based flow field analysis. This table compares the quantities of thrust and P_W, showing consistent differences between the two experimental techniques. For the trust measurement, the *PIV*-based analysis shows around 10% higher values than the sensor. For the P_W measurement, the *PIV*-based analysis is approximately 8~9% lower than the results for the sensor measurement. This difference in power might be caused by the fact that *PIV*-based analysis is incapable of capturing the blade profile loss and periodical unsteady effect due to the propeller rotation.

The table compares the results of the power saving when the propeller is ingesting the body wake. For the propeller in the *WI* configuration, the results show $2.4 \pm 1.8\%$ higher T with $9.6 \pm 1.4\%$ lower P_W based on the force balance measurements, while it shows $2.2 \pm 4.1\%$ higher T with $8.3 \pm 1.7\%$ lower P_W by using the *PIV*-based flow field analysis. From this perspective, the power saving obtained from the *PIV*-based flow field analysis is about $85 \pm 22\%$ of that obtained from force balance measurement. The mechanism of power saving due to the utilization of body wake is clearly demonstrated in Fig. 5-16, while the reduction in power due to the reduction of the downstream wake is still unclear. The error related to the $\dot{E}_{w,out}$ might be responsible for the difference in power savings predicted by the two experimental measurement techniques. The blade profile loss is likely to be reduced in the *WI* configuration, however, it was not possible to be captured in the *PIV* measurement.

5.4 Conclusions

The experimental research investigates three configurations, namely *FSP*, *WI* and *BLI*. A body of revolution and propeller are employed to study the three configurations using two experimental techniques, force balance measurements and stereoscopic *PIV*. The main conclusions which can be drawn from this research are:

- The stereoscopic *PIV*-based flow field analysis has been employed for the first time to investigate the flow mechanisms involved for a propeller ingesting body wake. This analysis is capable to show the details of the flow field around the propeller.
- The Power Balance Method has been applied to the velocity fields obtained from *PIV* to evaluate the integral forces and powers for the propeller.
- Force balance measurements indicate that the propeller consumes approximately 10% and 18% less shaft power in the *WI* and *BLI* configuration while maintaining a zero net force.
- The power saving obtained by *PIV*-based analysis is in the same order of magnitude as obtained from the force balance measurements.
- The *PIV*-based flow field analysis has been used to quantify the body wake energy.
- The main reason for the increased power coefficient of the propeller in *WI* and *BLI* can be attributed to the use of body wake power as a power source.
- The power reduction in the downstream wake of the propeller due to *WI* was not observed in the current experiments. Considering that the diameter of the propeller is (two times) larger than that of the body wake, this result is likely due to the propeller that is far from an ideal wake filling actuator disc to reduce downstream wake.

Chapter 6 Conclusions and Recommendations

This chapter presents the main conclusions of the research and provides recommendations for further studies on *BLI*. The research carried out during the course of this thesis consists of three pillars, namely the theoretical analysis, numerical simulations and the experimental investigations. To be precise, simulation and experimental investigations provide the proof of the mechanisms involved in *BLI* that were discussed in the theoretical analysis. Although the three studies focus on different aspect of *BLI*, the underlying principle should be observed in all approaches. This underlying key working principle, extracted from the three approaches, would be able to improve the understanding of *BLI*, and the research questions raised in Chapter 1.

This chapter consists of three sections: Section 6.1 reviews the three approaches employed in this research and their main findings. Section 6.2 concludes the entire research work, and Section 6.3 provides some recommendations for future research on *BLI*.

6.1 Observations in theoretical, numerical and experimental research

The theoretical analysis, numerical simulation and the experimental investigation help in understanding different facets of *BLI*. The theoretical analysis highlights the key mechanisms involved in *BLI*. The numerical simulation shows detailed quantifiable flow features regarding *BLI*. The experimental investigation has a high level of physical representation, but tends to be affected by spurious effects which are not directly relevant to *BLI*. For example, the possible flow separation occurring at the propeller blade might not be necessarily related to the physics of *BLI*. These studies are briefly reviewed, and the main findings are then summarized.

The theoretical analysis in Chapter 3 establishes the physical understanding of *BLI*. This analysis focuses on the power conversion in the *WI* and the *BLI* configurations. This work helps us to investigate the power saving mechanism. Then, the body/propulsor interaction occurring in the *BLI* configuration is qualitatively analyzed to clarify its influence on the performance of the integrated vehicle. The knowledge gained from this study is listed in the following arguments:

- In the *BLI* or *WI* configuration, the propulsor utilizes the energy in the wake of the body (illustrated in Fig. 6-1), thereby reducing the power required to generate an equivalent thrust at the same flight condition as in the freestream. The propulsor reduces the wake energy of the downstream wake flow (illustrated in Fig. 6-1and Fig. 6-2), thereby reducing the power consumption in the equilibrium condition (when thrust equals to drag).
- It is proved that the power coefficient is not an efficiency of power conversion for a propulsor operating in the *BLI* or *WI* configuration. The energy flow of the body wake (or boundary layer) is mainly responsible for power coefficients being greater than one.

- For a body with a fully attached boundary layer, the body/propulsor interaction increases the body drag in the *BLI* configuration. This effect is not detrimental to the performance of the vehicle since the interaction partially shifts the pressure recovery to the pressure side of the propulsor (It was assumed *WI* configuration can avoid this effect in the theoretical analysis).

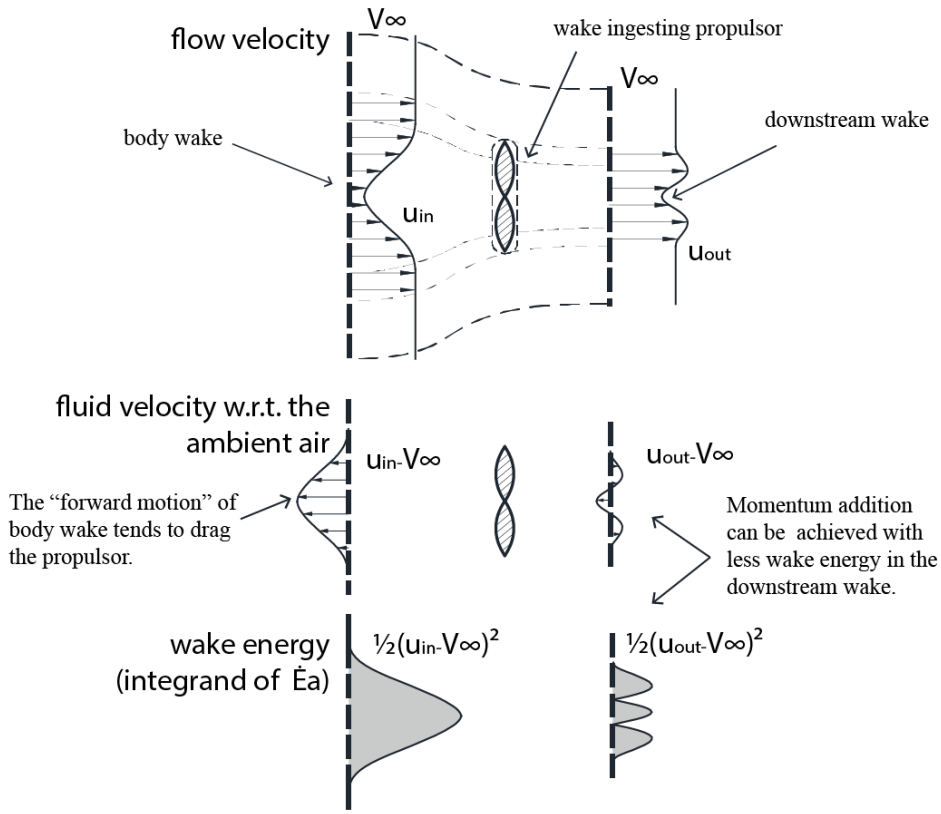

Fig. 6-1. A wake ingesting propulsor utilizes the wake energy of a body wake and reduces the wake energy of the downstream wake.

The numerical simulation in Chapter 4 is an extension of the theoretical analysis. The 2D steady laminar incompressible *CFD* simulations provide the mathematical proof of the mechanisms involved in *BLI*, described in the theoretical analysis. The *CFD* simulations are performed for a classical actuator disc, a flat plate and an integrated vehicle that combines the actuator disc and the plate in a *BLI* type configuration. The main conclusions from the simulations are as follows:

- It is possible to use the Power Balance Method for analyzing the flow field obtained from *CFD* simulations such that the power conversion within the flow field can be traced.
- The simulations demonstrate the typical power conversions, highlighting the special role of wake energy flow rate in the case of a flat plate and an integrated

vehicle. These two types of power conversion are helpful in understanding the physics of *BLI*.

- The simulations support the theoretical analysis of the mechanisms of *BLI* and evaluate the impact of *BLI* on the power terms and the drag force. In the special case of an integrated vehicle (which adopts a wake filling actuator disc model aiming to maintain the thrust/drag balance), the power saving mechanism reduces the actual power consumption by 12% as compared to an isolated flat plate. The body/propulsor interaction increases the viscous drag by 17.5% and increases the boundary layer dissipation by 8.2%.

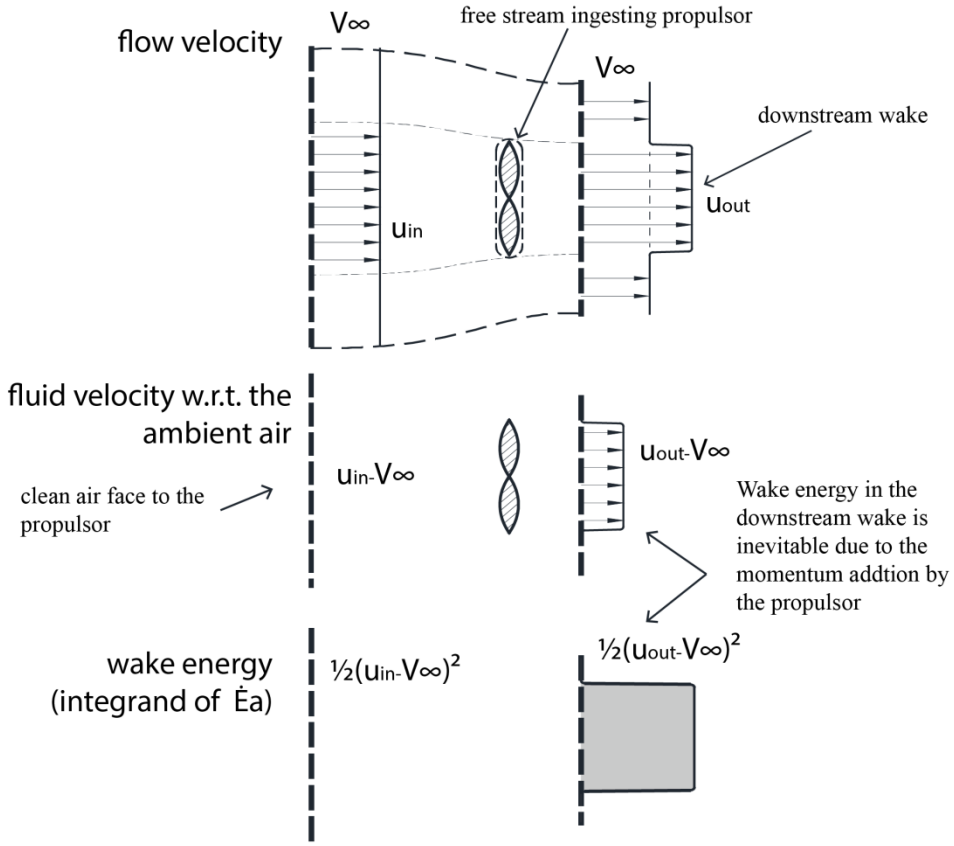

Fig. 6-2. A free stream ingesting propulsor leaves wake energy in the downstream wake.

The experimental investigation discussed in Chapter 5 aims to offer the experimental proof of mechanisms involved in *BLI*. The wind tunnel test employed a body of revolution and a propeller unit to formulate three configurations, namely *FSP*, *BLI* and *WI*. This test campaign used the conventional technique of force measurements to evaluate the impact of *BLI* (and *WI*) on various forces and powers. Moreover, a non-intrusive flow field analysis utilizing the *PIV* technique was used to

establish a direct evidence of the power conversion. The knowledge gained from the experiment is summarized as follows:

- The stereoscopic *PIV*-based flow field analysis has been used for the first time to investigate the flow mechanisms involved for a propeller ingesting body wake.
- The Power Balance Method has been applied to the velocity fields obtained from *PIV* to evaluate the integral forces and powers for the propeller.
- In the experiment, the thrust/drag equilibrium is maintained in the cases of three configurations. Force balance measurements indicate that the propeller consumes approximately 10% and 18% less shaft power in the *WI* and *BLI* configuration respectively.
- The power saving obtained by *PIV*-based analysis is in the same order of magnitude as obtained from the force balance measurements.
- The *PIV*-based flow field analysis has been used to quantify the body wake energy.
- The main reason for the increased power coefficient in *WI* and *BLI* can be attributed to the use of body wake power as a power source.
- The power reduction in the downstream wake of the propeller due to *WI* was not observed in the current experiments. As the diameter of the propeller is larger than that of the wake, this result is likely due to the propeller that is far from an ideal wake filling actuator disc to reduce downstream wake.

At this stage, a key question is "What is the generalized knowledge gained from this study". To answer this question, a key working principle is extracted from the three pillars of research to explain the benefit of *BLI*. By cancelling variations among the arguments and combining similar arguments, it allows us to generate an idea which is expressed in a concise statement:

The body (and downstream) wake energy flow rate (body or downstream wake power), participate in the power conversion process of the propeller.

6.2 Conclusions

The main conclusions of this research are presented in this section. Results from various sources suggest that *BLI* is a promising concept as it might reduce the power consumption of some new aircraft configurations. However, the discrepancy in expected power reduction indicates that there still exist some open issues concerning *BLI*. In particular, the discrepancy in various methods used to quantify the power coefficient and thrust/drag bookkeeping in preliminary studies lead to different physical interpretations of *BLI*. This shows that the aircraft design community might not understand the physics involved in *BLI* completely. Under these circumstances, this research tries to make a contribution to enhance the physical understanding of *BLI*. The two research questions addressed in this thesis are:

1. **What mechanisms are involved in *BLI* for the provided benefit?**
2. **How large is the benefit of *BLI*?**

To address these questions, this research follows a research line toward the power conversion associated with *BLI*. The research consists of theoretical analysis, numerical simulation and experimental investigations. Conclusions are drawn from this research to answer two major research questions, as given in the subsequent paragraphs.

For the first research question about the mechanisms of *BLI*, the answer shows at least three mechanisms.

- The first mechanism is the fact that the wake energy flow rate of the boundary layer (or body wake) is part of the input power to the *BLI* propulsor. This is observed from the propulsor's point of view. From a different perspective, on the level of entire aircraft, the wake energy flow rate functions as a transient power between the aircraft and the propulsor. This mechanism is evidenced in the simulation and experiment.
- The second mechanism is the possible reduction of the wake energy flow downstream of the propulsor. This research shows that this mechanism is valid under certain conditions. The numerical simulation proves that wake filling actuator disc model can reduce the downstream wake energy flow rate. Nevertheless, the experimental study did not support this conclusion. In fact, it was observed that the wake energy flow rate behind the propeller actually increased. This is due to the fact that the propeller used in the experiments is designed to work in an uniform inflow condition (free stream) and its diameter is larger than that of the wake, far from an ideal wake filling actuator disc.
- The third mechanism is the body-propulsor interaction that changes the pressure field around the body (aircraft) and the propulsor. This mechanism tends to increase the drag force of the body, however, this does not increase the total power consumption as the reduction in power consumption due to *BLI* is more than the increase in power due to increased drag. This is evidenced in the simulation of a flat plate integrated with an actuator disc model.

For the second research question about the benefit of *BLI*, conclusions can be drawn from this research.

- Theoretical, numerical and experimental approaches are adopted to quantify the benefit of *BLI*. A generalized result of the benefit has not been found, as it could depend on the flow conditions such as Reynolds number, Mach number, and etc. This research shows that the exact value of the power saving benefit depends on the specific conditions. For example, in the case of a flat plate (with laminar boundary layer) integrated with a wake filling actuator model, the theoretical analysis estimates that 21%

power consumption of the (isolated) flat plate can be reduced due to *BLI*, and the numerical simulation show a power saving of 12%. The difference can be attributed to the body-propulsor interaction that is ignored in the theoretical analysis. In the numerical simulation, the drag of the flat plate is increased by 17.9% due to the body-propulsor interaction. In the experiments, where a body of revolution is combined with a propeller, the results demonstrate that *BLI* can reduce the shaft power by around 18 % at the same flow conditions as in the numerical simulation.

6.3 Recommendations

This research shows that the benefit of power saving due to *BLI* can be substantial. However, it is still unclear how much power can be saved when *BLI* is applied to an actual aircraft. Several technical issues need to be addressed before drawing a conclusion. However, it would be fair to state that the identified benefit is high enough to motivate further investigation.

As for an actual aircraft concerned, more inputs are required from research institutes and industry. In terms of future research, the following aspects can be improved:

- A complete aircraft design includes wings, empennage, nacelle, etc. The effect of these components on the benefit of *BLI* should to be evaluated.
- Further investigations are required on the issues of noise emission, controllability and stability. These issues can be challenging for aircraft configurations utilizing *BLI* that place the propulsor in the rear fuselage.
- In the future experimental research, the size of the aircraft model should be scaled appropriately to study the *BLI* benefit that can be achieved by an actual aircraft.
- The analysis of aircraft performance should include flight conditions such as take-off, climb, descend, angle of attack, etc.
- Further research is required on the design and test of propulsors that aim to utilise *BLI*. Such propulsors should be designed to face non-uniform inflow and should reduce their downstream wake, as discussed in the numerical simulation of the ideal wake filling actuator disc model.

The current research is in agreement with several of the previous investigations on *BLI*, showing that *BLI* is a promising technology and might be suitable for future aircraft configurations. However, there are several open issues which need to be addressed, particularly the possible discrepencies about the physics involved. In that respect, this research contributes to the knowledge of aircraft design community by clarifying the actual power conversion concerning *BLI*. Efforts are made to elaborate that the wake energy flow rate is the key to understand the power conversion. At the

current stage, this work might provide some guidance for the future of research on *BLI*.

Appendix A. Integral force and power terms of the flow field

A 3D *CV* is obtained from an axisymmetric 2D boundary around the axis measured during the *PIV* measurements. Due to the axisymmetric nature of the flow, the surface integral over a cross section of the *CV* is given by Eqn. A1, and the volume integral can be expressed by Eqn. A2. The scan plane defines a scan stream surface and segregates a scan volume from the *CV*, as shown at the top of Fig. A. As a result, the surface integrals can be assessed at different axial positions and the volume integrals of the cumulative quantities can be evaluated.

$$\iint \; dS = \int_0^{radius} 2\pi y \cdot dy \tag{A1}$$

$$\iiint \; dV = \int_{xin}^{xout} \left(\int_0^{radius} 2\pi y \cdot dy \right) dx \tag{A2}$$

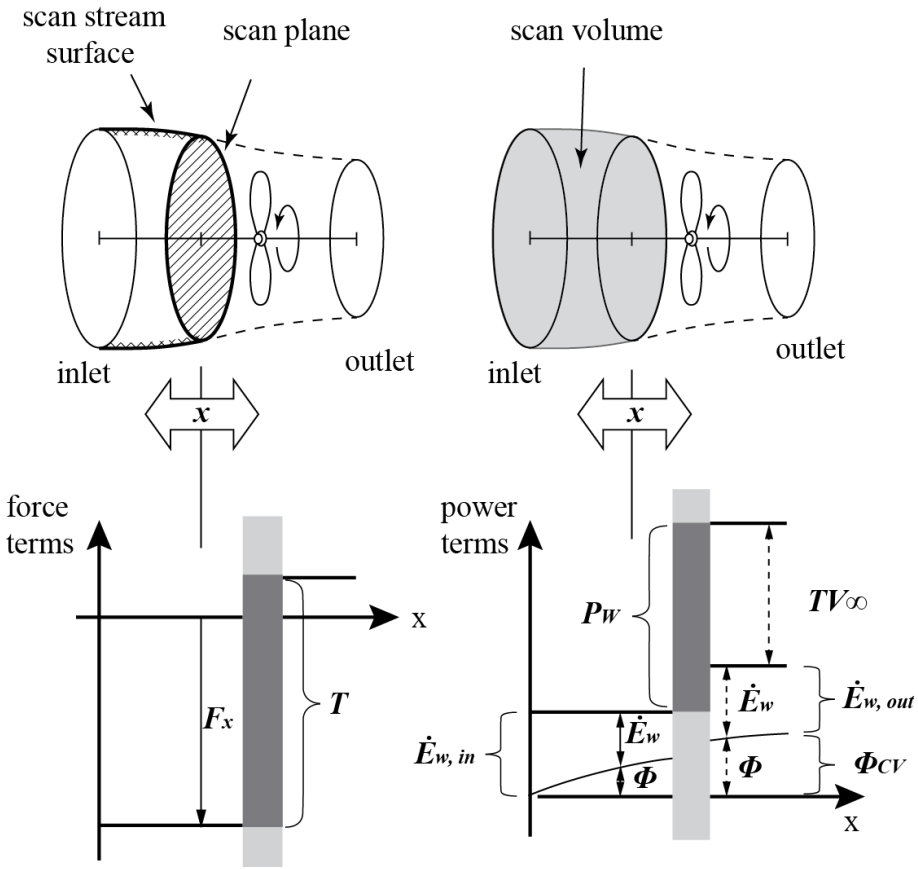

Fig. A. Variation of integral forces and powers with the axial position.

The integral forces and powers along the axis of the *CV* can be assessed by varying the axial position of the scan plane. The momentum equation can be used to

quantify the propeller thrust *T*, as shown in Eqn. (A3), including the pressure force exerted on the stream tube of the *CV*. Furthermore, the axial force F_x is defined as shown in Eqn. A4, which consists of momentum excess and pressure force. By changing the *x* location of the scan plane, F_x imparted to the flow field can be examined. A typical plot for the propeller in a *WI* configuration is shown at the bottom left of Fig. A.

$$T = \iint_{out}(P + \rho u^2)dS + \iint_{str\_tube}(Pn_x)dS - \iint_{in}(P + \rho u^2)dS \quad \text{(A3)}$$

$$F_x = \left[\iint_{scan}\rho u \cdot (u - V_\infty)\cdot dS\right] + \left[\iint_{scan}(P - P_a)dS + \iint_{str\_sur}(P - P_a)\cdot n_x dS\right] \quad \text{(A4)}$$

As for the integral power terms in the flow field, the propeller shaft power (P_W) imparted on the fluid corresponds to the change in mechanical energy of the flow and the viscous loss inside the *CV*, as given in Eqn. (A5).

$$P_W \cong \iint_{out}\left(\rho u\frac{1}{2}(u^2 + v^2 + w^2) + Pu\right)dS - \iint_{in}\left(\rho u\frac{1}{2}(u^2 + v^2 + w^2) + Pu\right)dS + \Phi_{CV} \quad \text{(A5)}$$

The energy deposition rates [33] at the scan plane denote wake energy of the flow $\dot{E}_w$, as the flow power relative to undisturbed free stream air. It contains the wake kinetic energy $K\dot{E}_w$ and pressure work rate $\dot{E}_p$ as expressed in Eqn. (A6).

$$\dot{E}_w = K\dot{E}_w + \dot{E}_P = \oint_{scan}\rho u\cdot\frac{1}{2}\left((u - V_\infty)^2 + (v^2 + w^2)\right)\cdot dS + \oint_{scan}(P - P_a)\cdot(u - V_\infty)dS \quad \text{(A6)}$$

The rate of viscous dissipation Φ is a volume integral whose integrand can be simplified to two dominant terms as given in Eqn. (A7). In the *PIV*-based assessment, contributions of both laminar and Reynolds stress are included.

$$\Phi \cong \iiint_{CV}\left(\left[\mu\left(\frac{\partial u}{\partial y}\right)^2 - \rho u'v'\frac{\partial u}{\partial y}\right] + \left[\mu\left(\frac{\partial w}{\partial y}\right)^2 - \rho v'w'\frac{\partial w}{\partial y}\right]\right)dV \quad \text{(A7)}$$

The integral power terms in the power balance equation (5.1) are evaluated for the axial position of the scan plane. It is noted that the dissipation Φ as a cumulative quantity of the scan volume, and it increases when the scan plane is moved downstream. The power conversion for a propeller in *WI* configuration is shown in the bottom right of Fig. A.

Bibliography

1. IATA. "Economic Performance Of the Airline Industry," *Report of Industry Economic Performance*. 2014.

2. Lee, J. J., Lukachko, S. P., Waitz, I. A., and Schafer, A. "Historical and Future Trends in Aircraft Performance, Cost, and Emissions," *Annual Review of Energy and the Environment* Vol. 26, No. 1, 2001, pp. 167-200.

doi: 10.1146/annurev.energy.26.1.167

3. Djibo, B. "ICAO Seminar on International Transport Policy and Liberalization-Outcome of ATConf/6 and ICAO follow-up work." Durban, South Africa, 2013.

4. Chapman, L. "Transport and climate change: a review," *Journal of Transport Geography*. Vol. 15, 2007, pp. 354-367.

5. Macintosh, A., and Wallace, L. "International aviation emissions to 2025: Can emissions be stabilised without restricting demand?," *Energy Policy*. Vol. 37, 2009, pp. 264-273.

6. Bruner, S., Baber, S., Harris, C., Caldwell, N., Keding, P., Rahrig, K., Pho, L., and Wlezian, R. "NASA N+ 3 Subsonic Fixed Wing Silent Efficient Low-Emissions Commercial Transport (SELECT) Vehicle Study. Revision A." 2010.

7. Krein, A., and Williams, G. "Flightpath 2050: Europe's Vision for Aeronautics," *Innovation for Sustainable Aviation in a Global Environment: Proceedings of the Sixth European Aeronautics Days, Madrid, 30 March-1 April, 2011*.

8. Greitzer, E., Bonnefoy, P., De la Rosa Blanco, E., Dorbian, C., Drela, M., Hall, D., Hansman, R., Hileman, J., Liebeck, R., and Lovergren, J. "N+ 3 Aircraft Concept Designs and Trade Studies Final Report," *NASA CR-2010-216794/vol2, NASA Glenn Research Center, Cleveland, Ohio* Vol. 44135, 2010.

9. Graham, W., Hall, C., and Morales, M. V. "The potential of future aircraft technology for noise and pollutant emissions reduction," *Transport Policy* Vol. 34, 2014, pp. 36-51.

10. Ashcraft, S. W., Padron, A. S., Pascioni, K. A., Stout Jr, G. W., and Huff, D. L. *Review of propulsion technologies for N+ 3 subsonic vehicle concepts*: NASA Glenn Research Center, 2011.

11. Schmidt, M. "The Sankey Diagram in Energy and Material Flow Management," *Journal of Industrial Ecology* Vol. 12, No. 1, 2008, pp. 82-94.

doi: 10.1111/j.1530-9290.2008.00004.x

12. Rao, A. G. "Aero Engine Technology-Introduction," *Lecture notes*. TU Delft, 2011, p. 10~15.

13. Jobe, C. E. "Prediction of Aerodynamic Drag." DTIC Document, 1984.

14. Hegen, G. H., Puffert-Meisner, W., Dieterle, L., and Vollmers, H. "Flow field investigation on a wing installed Counter Rotating Ultra-high-bypass Fan engine simulator in the low speed wind tunnel DNW-LST." 1999.

15. Sclafani, A. J., Vassberg, J. C., N. A. Harrison, Rumsey, C. L., Rivers, S. M., and Morrison, J. H. "CFL3D/OVERFLOW results for DLR-F6 wing/body and drag prediction workshop wing," *Journal of Aircraft* Vol. 45, 2008, pp. 762-780.

doi: 10.2514/1.30571

16. Saravanamuttoo, H. I. H., Rogers, G. F. C., and Cohen, H. "Gas turbine theory." Pearson Education, 2001, pp. 123-138.

17. Ballal, D. R., and Zelina, J. "Progress in Aeroengine Technology (1939--2003)," *Journal of aircraft* Vol. 41, No. 1, 2004, pp. 43-50.

18. Mattingly, J. D. "Aircraft engine design." AIAA, 2002, pp. 19-39.

19. Dewanji, D. "Flow characteristics in lean direct injection combustors." PhD thesis, TU Delft, 2012.

20. Laban, M. "Aircraft Drag and Thrust Analysis (AIRDATA)." National Aerospace Laboratory NRL, 2000.

21. Group, M. S. "Guide to in-flight thrust measurement of turbojets and fan engines," *AGARDograph AG-237, Jan*. 1979.

22. Whitcomb, R. T. "Review of NASA supercritical airfoils," *ICAS paper*, No. 74-10, 1974, pp. 25-30.

23. Harris, C. D. "NASA Supercritical airfoils: a matrix of family-related airfoils." NASA Langley Research Center, 1990.

24. Fujino, M., and Kawamura, Y. "Wave-drag characteristics of an over-the-wing nacelle business-jet configuration," *Journal of Aircraft* Vol. 40, No. 6, 2003, pp. 1177-1184.

25. Patterson, J. C., and Flechner, S. G. "Jet-wake effect of a high-bypass engine on wing-nacelle interference drag of a subsonic transport airplane." NASA TN D-6067, NASA, 1970.

26. Kroo, I. "Drag Due To Lift: Concepts for Prediction and Reduction," *Annual Review of Fluid Mechanics* Vol. 33, No. 1, 2001, pp. 587-617.

doi: 10.1146/annurev.fluid.33.1.587

27. Eppler, R. "Induced drag and winglets," *Aerospace Science and Technology* Vol. 1, No. 1, 1997, pp. 3-15.

28. Hegen, G., Puffert-Meissner, W., Dieterle, L., and Vollmers, H. *Flow field investigations on a wing installed Counter Rotating Ultra-high-bypass Fan engine simulator in the low speed wind tunnel DNW-LST*: Nationaal Lucht-en Ruimtevaartlaboratorium, 1999.

29. Banks, D. W., Van Dam, C., Shiu, H., and Miller, G. *Visualization of in-flight flow phenomena using infrared thermography*: NASA Dryden Flight Research Center, 2000.

30. Braslow, A. L. *A history of suction-type laminar-flow control with emphasis on flight research*: Books Express Publishing, 1999.

31. Fransson, J. H., Talamelli, A., Brandt, L., and Cossu, C. "Delaying transition to turbulence by a passive mechanism," *Physical review letters* Vol. 96, No. 6, 2006, p. 064501.

32. Eitelberg, G. "Introduction to Engine Integration testing," *Lecture notes of Aero Engine Technology*. TU Delft, 2011.

33. Drela, M. "Power Balance in Aerodynamic Flows," *AIAA Journal* Vol. 47, No. 7, 2009, pp. 1761-1771.

doi: 10.2514/1.42409

34. Plas, A., Sargeant, M., Madani, V., Crichton, D., Greitzer, E., Hynes, T., and Hall, C. "Performance of a boundary layer ingesting (BLI) propulsion system,"

45th American Institute of Aeronautics and Astronautics Aerospace Sciences Meeting and Exhibit, Reno, NV. AIAA 2007-450, AIAA, 2007.

35. Daggett, D. L., Kawai, R., and Geiselhart, K. A. "Blended wing body systems studies: boundary layer ingestion inlets with active flow control," *NASA CR-2003-212670*. 2003, p. 2003.

36. Felder, J., Hyun, K., and Brown, G. "Turboelectric distributed propulsion engine cycle analysis for hybrid-wing-body aircraft," *47th AIAA Aerospace Sciences Meeting*. AIAA 2009-1132, AIAA, Orlando, 2009.

37. Uranga, A., Drela, M., Greitzer, E., Titchener, N., Lieu, M., Siu, N., Huang, A., Gatlin, G. M., and Hannon, J. "Preliminary Experimental Assessment of the Boundary Layer Ingestion Benefit for the D8 Aircraft," *52nd Aerospace Sciences Meeting*. AIAA 2014-0906, AIAA, Maryland, 2014.

38. Pandya, S. A., Uranga, A., Espitia, A., and Huang, A. "Computational Assessment of the Boundary Layer Ingesting Nacelle Design of the D8 Aircraft," *52nd Aerospace Sciences Meeting*. AIAA 2014-0907, AIAA, Maryland, 2014.

39. Froude, W. "Note by Froude to his remarks on Professor Rankine's paper "On the mechanical principles of the action of propellers"," *Trans Inst Naval Architects*. Vol. 6, 1865, pp. 31-39.

40. Ghose, J., and Gokarn, R. "Basic ship propulsion." Allied Publishers, 2004, pp. 94-100.

41. Woud, H. K., and Stapersma, D. "Design of Propulsion and Electric Power Generation Systems." IMAREST, Institute of Marine Engineering, Science and Technology, 2002, pp. 55-59.

42. Durand, W. F. "Aerodynamic Theory: A General Review of Progress. ." Vol. Volume IV, Julius Springer, Berlin, 1935, pp. 286-289.

43. McLemore, H. C. "Wind-tunnel tests of a 1/20-scale airship model with stern propellers," *NASA TN D-1026*. DTIC Document, 1962.

44. Alexander, H., Dorn, F., Lutz, T., and Kramer, E. "Improvement of Propulsive Efficiency by Dedicated Stern Thruster Design," *7th AIAA ATIO Conf, 2nd CEIAT Int'l Conf on Innov and Integr in Aero Sciences,17th LTA Systems Tech Conf; followed by 2nd TEOS Forum*. AIAA 2007-7702, AIAA, 2007.

45. Kawai, R. T., Friedman, D. M., and Serrano, L. "Blended wing body (BWB) boundary layer ingestion (BLI) inlet configuration and system studies," *NASA CR-214534*. 2006.

46. Sato, S. "The power balance method For aerodynamic performance assessment." PhD thesis, Massachusetts Institute of Technology, 2012.

47. Arntz, A., Atinault, O., and Merlen, A. "Exergy-Based Formulation for Aircraft Aeropropulsive Performance Assessment: Theoretical Development," *AIAA Journal* Vol. 53, No. 6, 2014, pp. 1627-1639.

doi: 10.2514/1.J053467

48. Arntz, A., and Atinault, O. "Exergy-Based Performance Assessment of a Blended Wing–Body with Boundary-Layer Ingestion," *AIAA Journal* Vol. 53, No. 12, 2015, pp. 3766-3776.

doi: 10.2514/1.J054072

49. Duncan, W. J., Thom, A. S., and Young, A. D. "Mechanics of Fluids (S.I. Units)." Edward Arnold, London, 1970, pp. 692-693.

50. Roskam, J., and Lan, C.-T. E. "Airplane aerodynamics and performance." DARcorporation, 1997, pp. 298-299.

51. Froude, R. "On the part played in propulsion by differences of fluid pressure," *Transactions of the Institute of Naval Architects*. Vol. 30, 1889, pp. 390-405.

52. *The Jet Engine*: Rolls Royce plc, 1986.

53. "Correlation, Operation, Design, and Modification of Turbofan, Jet Engine Test Cells," *No. AC43-207*. CIRCULAR ADVISORY, 2002.

54. *Propeller/propfan In-flight Thrust Determination*: Society of Automotive Engineers, 1993.

55. Sibilli, T., Savill, M., Sethi, V., MacManus, D., and Rolt, A. M. "Numerical Simulation of Propulsion System Integration for Very High Bypass Ratio Engines," *ASME Turbo Expo 2012: Turbine Technical Conference and Exposition*. GT 2012-68908, ASME, 2012, pp. 185-193.

56. Brodersen, O. "Drag prediction of engine-airframe interference effects using unstructured Navier-Stokes calculations," *Journal of Aircraft*. Vol. 39, 2002, pp. 927-935.

57. Hegen, G., and Kiock, R. "Experiences with ultra-high-bypass simulators from calibration and isolated engine testing," *Aspects of engine airframe integration for transport aircraft*. National Aerospace Laboratory NLR, 1996.

58. Hoheisel, H. "Aerodynamic aspects of engine-aircraft integration of transport aircraft," *Aerospace science and technology*. Vol. 1, 1997, pp. 475-487.

59. Tognaccini, R. "Drag computation and breakdown in power-on conditions," *Journal of Aircraft* Vol. 42, No. 1, 2005, pp. 245-252.

60. Rossow, C. C., Godard, J. L., Hoheisel, H., and Schmitt, V. "Investigations of propulsion integration interference effects on a transport aircraft configuration," *Journal of Aircraft* Vol. 31, No. 5, 1994, pp. 1022-1030.

doi: 10.2514/3.46605

61. Godston, J., and Reynolds, C. H. "Propulsion system integration configurations for future prop-fan powered aircraft," *Journal of Aircraft* Vol. 22, No. 12, 1985, pp. 1027-1033.

doi: 10.2514/3.45245

62. Lange, R. H. "A review of advanced turboprop transport aircraft," *Progress in Aerospace Sciences*. Vol. 23, 1986, pp. 151-166.

63. Veldhuis, L. L. M. "Propeller wing aerodynamic interference." PhD Thesis, TU Delft, 2005.

64. Kroo, I. "Propeller-wing integration for minimum induced loss," *Journal of Aircraft* Vol. 23, No. 7, 1986, pp. 561-565.

doi: 10.2514/3.45344

65. Veldhuis, L. L. M. "Review of propeller-wing aerodynamic interference," *24th International Congress of the Aeronautical Sciences, ICAS Paper*. Vol. 6, 2004.

66. Sinnige, T., Kuijk, J. v., Lynch, K. P., Ragni, D., Eitelberg, G., and Veldhuis, L. L. M. "The Effects of Swirl Recovery Vanes on Single-Rotation Propeller Aerodynamics and Aeroacoustics," *21st AIAA/CEAS Aeroacoustics Conference*. AIAA 2015-2358, AIAA, Dallas, 2015.

67. Wang, Y., Li, Q., Eitelberg, G., Veldhuis, L., and Kotsonis, M. "Design and numerical investigation of swirl recovery vanes for the Fokker 29 propeller," *Chinese Journal of Aeronautics*. Vol. 27, 2014, pp. 1128-1136.

68. Yaros, S., Sexstone, M. G., Huebner, L. D., Lamar, J. E., McKinley, R., Torres, A. O., Burley, C. L., Scott, R. C., and Small, W. J. "Synergistic airframe-propulsion interactions and integrations." NASA Langley Research Center, 1998.

69. Smith, L. H. "Wake Ingestion Propulsion Benefit," *Journal of Propulsion and Power* Vol. 9, No. 1, 1993, pp. 74-82.

doi: 10.2514/3.11487

70. Froude, R. "A description of a method of investigation of screw-propeller efficiency," *Trans Inst Naval Architects*. Vol. 24, 1883, pp. 231-55.

71. Brown, D. K. *The way of a ship in the midst of the sea: the life and work of William Froude*: Periscope Publishing Ltd., 2006.

72. Carlton, J. S. "Ship Resistance and Propulsion," *Marine Propellers and Propulsion (Third Edition)*. Butterworth-Heinemann, Oxford, 2012, pp. 323-324.

73. Betz, A. "Introduction to the theory of flow machines." Pergamon press, Oxford, 1966, pp. 215-217.

74. Miley, S., and von Lavante, E. "Propeller Propulsion Integration—State of Technology Survey," *NASA CR-3882*. 1985.

75. Boxer, E. "Wind-Tunnel Investigation of Alternative Propellers Operating Behind Deflected Wing Flaps for the XB-36 Airplane." 1945.

76. Skaarup, H. *Maryland, Virginia, and Washington DC Warbird Survivors 2003: A Handbook on where to find them*: iUniverse, 2003.

77. Carrier, G., Atinault, O., Grenon, R., and Verbecke, C. "Numerical and Experimental Aerodynamic Investigations of Boundary Layer Ingestion for Improving Propulsion Efficiency of Future Air Transport," *31st AIAA Applied Aerodynamics Conference*. AIAA 2013-2406, AIAA, San Diego, California, 2013.

78. Sabo, K. M., and Drela, M. "Benefits of Boundary Layer Ingestion Propulsion," *53rd AIAA Aerospace Sciences Meeting*. AIAA 2015-1667, AIAA, Kissimmee, Florida, 2015.

79. "Gas Turbine Engine Inlet Flow Distortion Guidelines," *ARP 1420B*. SAE, 2002.

80. Seddon, J., and Goldsmith, E. L. *Intake aerodynamics*: AIAA, 1999.

81. Owens, L. R., Allan, B. G., and Gorton, S. A. "Boundary-Layer-Ingesting Inlet Flow Control," *Journal of Aircraft* Vol. 45, No. 4, 2008, pp. 1431-1440.

doi: 10.2514/1.36989

82. Anabtawi, A., Blackwelder, R., Lissaman, P., and Liebeck, R. "An experimental investigation of boundary layer ingestion in a diffusing S-duct with and without passive flow control," *37th Aerospace Sciences Meeting and Exhibit*. AIAA 99-0739, AIAA, 1999.

83. Lee, B. J., and Liou, M. S. "Re-Design of Boundary Layer Ingesting Offset Inlet via Passive Flow Control Manner," *48th AIAA Aerospace Sciences Meeting*

Including the New Horizons Forum and Aerospace Exposition. AIAA 2010-842, AIAA, 2010.

84. Gorton, S., Owens, L., Jenkins, L., Allan, B., and Schuster, E. "Active Flow Control on a Boundary-Layer-Ingesting Inlet," *42nd AIAA Aerospace Sciences Meeting and Exhibit*. AIAA 2004-1203, AIAA, 2004.

85. Gissen, A., Vukasinovic, B., McMillan, M., and Glezer, A. "Distortion Management in a BLI Inlet Diffuser using Synthetic-Jet Hybrid Flow Control," *49th AIAA Aerospace Sciences Meeting including the New Horizons Forum and Aerospace Exposition*. AIAA 2011-35, AIAA, 2011.

86. Blanco, E. d. l. R., Hall, C., and Crichton, D. "Challenges in the Silent Aircraft Engine Design," *45th AIAA Aerospace Sciences Meeting and Exhibit*. AIAA 2007-454, AIAA, 2007.

87. Defoe, J. "Inlet swirl distortion effects on the generation and propagation of fan rotor shock noise." PhD thesis, Massachusetts Institute of Technology, 2011.

88. Agarwal, A., and Dowling, A. P. "Low-Frequency Acoustic Shielding by the Silent Aircraft Airframe," *Aiaa Journal* Vol. 45, No. 2, 2007, pp. 358-365.

89. Block, P. J. W. "Noise radiation patterns of counter-rotation and unsteadily loaded single-rotation propellers," *Journal of Aircraft* Vol. 22, No. 9, 1985, pp. 776-783.

doi: 10.2514/3.45201

90. Kim, H., and Felder, J. "Control Volume Analysis of Boundary Layer Ingesting Propulsion Systems With or Without Shock Wave Ahead of the Inlet," *49th AIAA Aerospace Sciences Meeting including the New Horizons Forum and Aerospace Exposition*. AIAA 2011-222, AIAA, 2011.

91. Ferri, A. "Airframe/Engine Integration," *AGARD-LS-53*. DTIC Document, 1972.

92. Hardin, L., Tillman, G., Sharma, O. P., Berton, J., and Arend, D. J. "Aircraft System Study of Boundary Layer Ingesting Propulsion," *48th AIAA/ASME/SAE/ASEE Joint Propulsion Conference & Exhibit*. AIAA 2012-3993, AIAA, Georgia, 2012.

93. Drela, M. "Development of the D8 Transport Configuration," *29th AIAA Applied Aerodynamics Conference*. AIAA 2011-3970, AIAA, 2011.

94. Schlichting, H., Gersten, K., and Gersten, K. *Boundary-layer theory*: Springer Science & Business Media, 2000.

95. Horsten, B. J. C. "Low-Speed Model Support Interference - Elements of an Expert System," *Aerodynamics Dept.*, PhD Thesis, TU Delft, 2011, pp. 43-44.

96. Anderson, J. D., and Wendt, J. *Computational fluid dynamics*: Springer, 1995.

97. Oberkampf, W. L., Trucano, T. G., and Hirsch, C. "Verification, validation, and predictive capability in computational engineering and physics," *Applied Mechanics Reviews* Vol. 57, No. 5, 2004, pp. 345-384.

doi: 10.1115/1.1767847

98. Aeschliman, D. P., and Oberkampf, W. L. "Experimental Methodology for Computational Fluid Dynamics Code Validation," *AIAA Journal* Vol. 36, No. 5, 1998, pp. 733-741.

doi: 10.2514/2.461

99. Versteeg, H. K., and Malalasekera, W. *An introduction to computational fluid dynamics: the finite volume method*: Pearson Education, 2007.

100. *ANSYS FLUENT Theory Guide*, 2011.

101. Veldman, A. *Computational fluid dynamics*. Institute for Mathematics and Computer Science, University of Groningen, 2012.

102. Jasak, H. "Error analysis and estimation for the finite volume method with applications to fluid flows." PhD thesis, Imperial College London, 1996.

103. Westerweel, J. "Fundamentals of digital particle image velocimetry," *Measurement science and technology* Vol. 8, No. 12, 1997, p. 1379.

104. Lignarolo, L., Ragni, D., Krishnaswami, C., Chen, Q., Ferreira, C. S., and Van Bussel, G. "Experimental analysis of the wake of a horizontal-axis wind-turbine model," *Renewable Energy* Vol. 70, 2014, pp. 31-46.

105. Ewald, B. "Wind Tunnel Wall Corrections (la Correction des effets de paroi en soufflerie)," *AGARD-AG-336*. DTIC Document, 1998.

106. Meinhart, C. D., and Wereley, S. T. "The theory of diffraction-limited resolution in microparticle image velocimetry," *Measurement science and technology* Vol. 14, No. 7, 2003, p. 1047.

107. Willink, R. "Measurement Uncertainty and Probability." Cambridge University Press, West Nyack, 2013.

108. Raffel, M., Willert, C. E., and Kompenhans, J. *Particle image velocimetry: a practical guide*: Springer, 2013.

109. Schrijer, F., and Scarano, F. "Effect of predictor–corrector filtering on the stability and spatial resolution of iterative PIV interrogation," *Experiments in Fluids* Vol. 45, No. 5, 2008, pp. 927-941.

110. Lv, P., Rao, A. G., Ragni, D., and Veldhuis, L. "Performance Analysis of Wake and Boundary-Layer Ingestion for Aircraft Design," *Journal of Aircraft* Vol. 53, No. 5, 2016, pp. 1517-1526.

111. van Oudheusden, B. W., Scarano, F., Roosenboom, E. W., Casimiri, E. W., and Souverein, L. J. "Evaluation of integral forces and pressure fields from planar velocimetry data for incompressible and compressible flows," *Experiments in Fluids* Vol. 43, No. 2-3, 2007, pp. 153-162.

112. Ragni, D., van Oudheusden, B. W., and Scarano, F. "Non-intrusive aerodynamic loads analysis of an aircraft propeller blade," *Experiments in Fluids* Vol. 51, No. 2, 2011, pp. 361-371.

113. Ragni, D. "PIV-based load determination in aircraft propellers." PhD Thesis, TU Delft, 2012.

114. Van Oudheusden, B., Scarano, F., and Casimiri, E. "Non-intrusive load characterization of an airfoil using PIV," *Experiments in Fluids* Vol. 40, No. 6, 2006, pp. 988-992.

115. Scarano, F., and Riethmuller, M. L. "Advances in iterative multigrid PIV image processing," *Experiments in Fluids*. Vol. 29, 2000, pp. 51-60.

116. van Oudheusden, B. W. "PIV-based pressure measurement," *Measurement Science and Technology* Vol. 24, No. 3, 2013, p. 032001.

Acknowledgements

I would like to thank China Scholarship Council (CSC) for the financial support which allows me to do PhD research in TU Delft. The CSC scholarship makes my dream become true: to do the most exciting research in a top university.

I would like to express my gratitude to my promotor Prof. Leo Veldhuis. You are always kind and it is a pleasure to work with you. I have been inspired by your enthusiasm in aviation since our first meet. In the wind tunnel test, you provided many wise suggestions which are valuable and helpful. Moreover, you encouraged me when I feel frustrated in writing this thesis and your encouragements support me going through difficult times.

Dr. Arvind G. Rao, please accept my deepest appreciation! As my co-promotor, you graciously accept me as a PhD candidate and you have made enormous amount of efforts to guide me in research. I feel proud that your efforts are paying-back. I would like to thank you for the assistance in finalizing this thesis. Your high standard is impressive and it was a great experience to work with you!

I would like to thank Prof. Georg Eitelberg. It is an honor to work with you. You played a special role in inspiring me with research work. Especially, you challenged me with truly tough questions. This gives me a chance to rethink my work profoundly. I consider those challenges as touch stones which sharp my mind and these will benefit me in the rest part of my career. Thank you!

This research work won't be completed without the support of Dr. Dani Ragni. Our collaboration in windtunnel test and journal papers is productive. I would like to thank graduate students Tarik Hartuç and Nando van Arnhem, and it was of great joy to work with you! I couldn't forget the day Tarik and I shout out loudly in the wind tunnel when we got the exciting results. Nando presented very impressive work to help me understanding my research better, and you are very kind to translate the summary of this thesis into Dutch.

I would like to give thanks to my office mate and friend Mo Li. We had so many great times in discussing aircraft and we enjoyed our first glider flight together. It is of great joy to work with my colleges and friends in the FPP group, Yannian Yang, Dipanjay Dewanji, Feijia Yin, Qingxi Li, Haiqiang Wang, Mark Voskuijl, Tomas Sinnige, Andr é Perpignan. We have great time in the coffee corner and it is your companionship makes my life in the Netherlands rich and colorful.

Last but not least, my parents Giexiang Lv and Xunfeng Feng, your love supports me through the good and bad times. I can always get inspirations from you and I feel lucky to be your son. My beloved fianc ée Jingjing Yang, it is your love and encouragement supported me in finalizing this thesis and starting up my career. Thank you!